Murdoch
UNIVERSITY

Discipline of Engineering and Energy

Stability of Microgrids and Weak Grids with High Penetration of Variable Renewable Energy

Julius Susanto

32921063

This thesis is presented for the Degree of

Doctor of Philosophy

of

Murdoch University

January 2020

Declaration

I declare that this thesis is my own account of my research and contains as its main content work which has not previously been submitted for a degree at any tertiary education institution.

Julius Susanto

20/01/2020

Abstract

Autonomous microgrids and weak grids with high penetrations of variable renewable energy (VRE) generation tend to share several common characteristics: i) low synchronous inertia, ii) sensitivity to active power imbalances, and iii) low system strength (as defined by the nodal short circuit ratio). As a result of these characteristics, there is a greater risk of system instability relative to larger grids, especially as the share of VRE is increased.

This thesis focuses on the development of techniques and strategies to assess and improve the stability of microgrids and weak grids. In the first part of this thesis, the small-signal stability of inertia-less converter dominated microgrids is analysed, wherein a load flow based method for small-signal model initialisation is proposed and used to examine the effects of topology and network parameters on the stability of the microgrid. The use of a back-to-back dc link to interconnect neighbouring microgrids and provide dynamic frequency support is then proposed to improve frequency stability by helping to alleviate active power imbalances. In the third part of this thesis, a new technique to determine the optimal sizing of smoothing batteries in microgrids is proposed. The technique is based on the temporal variability of the solar irradiance at the specific site location in order to maximise PV penetration without causing grid instability.

A technical framework for integrating solar PV plants into weak grids is then proposed, addressing the weaknesses in conventional Grid Codes that fail to consider the unique characteristics of weak grids. Finally, a new technique is proposed for estimating system load relief factors that are used in aggregate single frequency stability models.

Acknowledgments

First and foremost, I would like to express my gratitude to my principal supervisor Dr. Farhad Shahnia for his patient and invaluable guidance throughout my candidacy. In future, I hope to continue the wide-ranging multi-hour discussions that we used to have in his office. I would also like to thank my advisory committee Dr. GM Shafiullah and Dr. Manickam Minakshi for their advice and support throughout my studies.

Last but not least, I would like to thank my family for their unconditional support and love. They provided the encouragement to continue when I felt like giving up and I wouldn't have finished without them.

Table of Contents

List of Figures

List of Tables

List of Abbreviations

BESS	Battery energy storage systems
BOM	Bureau of Meteorology
CFCT	Critical fault clearing time
CDF	Cumulative distribution function
DAE	Differential-algebraic equations
DER	Distributed energy resources
EMS	Energy Management System
EMT	Electromagnetic transients
DoD	Depth of discharge
dq	Direct-quadrature
GHI	Global horizontal irradiance
IEC	International Electrotechnical Commission
LRF	Load relief factor
LPF	Low pass filter
ODE	Ordinary differential equation
PDF	Probability density function
PFR	Primary frequency response

PI	Proportional-integral
PLL	Phase-locked loop
PONE	Probability of non-exceedance
PV	Photovoltaic
PWM	Pulse width modulation
RoCoF	Rate of change of frequency
SBOC	Smoothing battery’s optimal capacity
SCADA	Supervisory control and data acquisition
SCR	Short circuit ratio (system strength)
SIVI	Solar irradiance variability index
SoC	State of charge
SR	Stiffness ratio
SWIS	Southwest Interconnected System
UFLS	Under frequency load shedding
UPS	Uninterruptible power supply
VRE	Variable renewable energy
VSC	Voltage source converter

Chapter 1 **Introduction**

1.1 **Problem Statement**

Variable renewable energy (VRE) generation (such as wind and solar) has in recent years become cost-competitive with traditional thermal generation (such as coal and gas) and is on a trajectory to become the least cost generation option [1-2]. As a result, we are in the midst of a worldwide development boom in wind and solar, leading to a 7-fold and 45-fold increase in the global installed wind and solar power capacity between 2005 and 2015 respectively. As renewable energy incentive programs in Europe and North America are wound down, developers are increasingly looking outside these mature markets and beginning to make forays into developing countries [3]. While this includes large markets such as China [4] and India [5], smaller developing markets in Asia, Africa and South America are also being targeted. However, the weak grids present in many of these developing countries are less robust and are less capable of accommodating large shares of VRE when compared to the large interconnected grids of Europe and North America [7].

For remote and isolated areas that typically rely on diesel generation, VRE also delivers significant economic benefits by lowering average energy generation costs [6]. The concept of a standalone (autonomous) microgrid has been proposed as a possible power supply option for remote areas where an external electricity grid is unavailable or inaccessible [8-10]. In this context, an autonomous microgrid is a

cluster of loads and generators that can act as a single controllable unit in order to maintain bus voltages and frequency within acceptable ranges. The generators are considered as distributed energy resources (DERs) which are typically in the form of power electronic interfaced DERs, such as solar photovoltaic (PV) systems, wind turbines, micro-hydro turbines, battery storage and fuel cells systems or inertial DERs, such as induction / synchronous generators [11].

As the penetration of VRE increases in microgrids and weak grids, so does the risk of system instability due to factors associated with high VRE penetration in such power systems, e.g., low synchronous inertia, sensitivity to active power imbalances and low system strength [12].

1.2 Aims and objectives of the thesis

The overall objective of this thesis is to develop techniques for analysing and improving the stability of microgrids and weak grids with high penetrations of VRE. Several different facets of this problem are investigated in this thesis, with the following specific objectives:

- Analyse the effects that network parameters and topological features in a converter dominated microgrid affect system small-signal stability
- Explore the interconnection of two neighbouring microgrids in order to improve frequency stability
- Study the optimal of sizing smoothing battery energy storage systems (BESS) to mitigate frequency instability risks and increase PV penetration in a microgrid
- Investigate the specific technical considerations required to integrate solar PV into weak grids to maintain system security and stability

- Analyse high-speed fault recorder data of generator contingency events to estimate the system load relief factor, which is an important input to frequency stability studies in weak grids

1.3 Significance of research

The confluence of economic drivers and increasing concerns over climate change has seen an acceleration in VRE deployments all around the world, firstly in large interconnected grids, but now shifting to weak grids and small-scale autonomous microgrids. Maintaining grid stability with flexible resources will be the key challenge to integrate ever larger shares of VRE into microgrids and weak grids.

The research presented in this thesis has attempted to address some of these stability challenges. The main contributions of this thesis to the research field are as follows:

a) **Small-signal stability of converter dominated microgrids:** developing a new load flow based method for initialising the small-signal model of a microgrid and using this method to derive insights on the effects of topology and network parameters on the stability of the microgrid.

b) **Interconnected microgrids for frequency stability support:** proposing a back-to-back dc link to interconnect neighbouring microgrids that can provide dynamic frequency support due to active power imbalances.

c) **Optimal smoothing battery sizing for microgrids:** proposing a new technique for the optimal sizing of smoothing batteries in microgrids based on the temporal variability of the solar irradiance at the specific

site location in order to maximise PV penetration without causing grid instability.

d) **PV integration into weak grids:** developing a technical framework intended to be used by network operators during the decision-making process for approving PV plant connections into weak grids and outlining the possible mitigation techniques when technical criteria are not met.

e) **Frequency stability analysis in weak grids:** proposing a new technique for estimating the system load relief factor using high-speed fault recorder data.

1.4 Structure of the thesis

The remainder of this thesis is organised as follows: **Chapter 2** describes the needs and justifications of the research work through a literature review**. Chapter 3** describes the methods and analysis techniques proposed in this thesis, the implementation of which are discussed in later chapters.

Chapter 4 examines the small-signal stability of converter dominated microgrids and how network parameters and topological features impact microgrid stability. In **Chapter 5**, the concept of interconnecting neighbouring microgrids via back-to-back dc links is investigated, the simulation results showing that such an interconnection can be applied to provide dynamic frequency support. The optimal sizing method for a smoothing battery proposed in Chapter 3 is evaluated in **Chapter 6**, where it is shown that the temporal irradiance characteristics of the site location has a significant influence on the minimum sizing of the battery to smooth out PV fluctuations and assist frequency stability. **Chapter 7** presents sample case studies to

illustrate the assessment framework proposed in Chapter 3 for integrating PV plants into weak grids. In **Chapter 8**, the proposed system load relief factor estimation procedure is applied on real high-speed measurement data from a medium-sized weak grid.

Finally, the conclusions drawn from this research and the recommendations for future work are highlighted in **Chapter 9**.

Chapter 2 Literature Review

In this chapter, a literature review is carried out to evaluate the state of the art as it pertains to 1) the stability of converter dominated microgrids, 2) frequency stability in weak grids, 3) interconnecting microgrids to improve stability, 4) the use of battery energy storage systems (BESSs) in microgrids to smooth out active power fluctuations due to PV intermittency, and 5) the integration of PV into weak grids.

2.1 Stability of Converter Dominated Microgrids

Converter-dominated power systems have pre-dated the concept of microgrids and were first studied for use in standalone Uninterruptible Power Supply (UPS) systems [13-14]. However, since the popularisation of the term "microgrid" in 2002 [15], converter- or inverter-dominated microgrids have been the subject of numerous studies, both in the context of power system control and stability [16-17]. Ref [18] suggests a taxonomy of stability issues applicable for microgrids focusing on three main areas: small-signal stability, transient stability and voltage stability.

2.1.1 Small-Signal Stability

Since converter-dominated microgrids in standalone mode are largely inertia-less, stability analyses of such microgrids normally revolve around small-signal

stability [19]. The small-signal stability of a multi-synchronous machine-based power system is extended to microgrids, and different techniques such as eigenanalysis and frequency-response (impedance-based) are used [14, 20]. Ref. [21] reviews various methods such as transformation into a rotating direct-quadrature reference frame, dynamic phasors, reduced-order modelling, and harmonic linearisation.

In eigenanalysis, the studied system is expressed by its state-space equations. The corresponding eigenvalues are then calculated from the state matrix [14]. An eigenanalysis-based small-signal model of a microgrid composed of converter-interfaced DERs is presented in [21-28]. Ref. [29-30] even consider the dynamics of the DERs in the small-signal analysis of the microgrid while [31] presents a reduced order model by simplifying the dynamics of converters of the DERs. Similarly, [32] presents another reduced order model using the singular perturbation method and simplifying the utilised filters. Ref. [33-36] study the impact of communication delays, presence of constant-power loads, induction motor loads, and the ramp rates of the DERs on the stability of the microgrid. These studies indicate that the most dominant parameter in the small-signal stability of droop-controlled microgrids is the power-frequency droop coefficient [37].

Proposed improvements to small-signal stability in microgrids include supplementary control loops [38], active damping [39] and coordinated control of the DERs [18]. In the context of interconnected microgrids, small signal stability was examined in [47] for ac switch type connections.

The above studies have focused on a microgrid with a known structure while [27] and [40] have only analysed the impact of the microgrid topology on its stability. This is a research gap that is addressed in this thesis, exploring how the microgrid topology and parameters (e.g., line impedances, lengths, etc.) influence its stability.

Another gap addressed in this thesis are the practical issues with the initialisation of the small-signal model. Previous works tend to use time-domain simulations (e.g., PSCAD) to arrive at the steady-state operating point for the small-signal model [22, 26]. However, this approach is time consuming, especially when attempting to test many different and arbitrary network and/or model configurations. A load flow initialisation would obviate the need to run a time-domain simulation externally to the small-signal model initialisation routine. As a result, bulk simulation runs can be automated and executed with scripts.

2.1.2 **Transient Stability**

Due to their inertia-less nature, conventional transient (or large-signal) stability analyses based on the swing equation is not valid for converter dominated microgrids since the concept of rotor angle is not intrinsic to converter-based sources, i.e., there is no natural physical relationship between system frequency and the active power output of converters [44].

However, standard transient stability analyses may need to be considered for microgrids that are operating in grid-connected mode or for microgrids with a mix of synchronous machines and converters [41]. In such system, standard rotor angle stability techniques are typically applied such as RMS simulation and equal area criterion analysis, for example in [42-43]. Alternatively, pure simulation approaches using detailed EMT models can be performed. In such approaches, the microgrid models are perturbed with large disturbances and multiple simulation runs are studied to find the stable and unstable operating points [142].

The transient stability of completely inertia-less systems has not been the subject of many works, with one approach using Lyapunov functions being a rare exception

[44]. Instead, for inertia-less converter dominated systems, researchers have proposed adopting converter control systems that mimic the behaviour of synchronous machines, called synchronverters or virtual synchronous generators [143-144]. This has the effect of introducing "virtual" inertia into the system, thus facilitating the use of standard rotor angle stability techniques to analyse transient stability [145-146].

2.1.3 **Voltage Stability**

Voltage stability issues for inertia-less systems are more or less the same as for conventional power systems, with reactive power limits, overloading, long high impedance lines, load dynamics and tap changers causing the majority of issues [18].

Power flow analyses using P-V and Q-V curves can generally be used to assess voltage stability. The P-V curve indicates the limits to system loading before voltage collapse, while the Q-V curve indicates the quantity of reactive reserve at a bus for any given voltage operating point. Ref. [45] derives sufficient conditions for ensuring voltage stability in weak grids with converter interfaced sources.

The reactive power range of the converters themselves can be used to maintain and improve voltage stability in an inertia-less microgrid. One of the central questions investigated in the literature has been how reactive power should be shared between converters in the microgrid [147]. Centralised approaches have been proposed where a master microgrid controller determines the proportional balancing of reactive power between converters [148-149]. Alternatively, fully decentralised approaches without the use of master controllers have been explored, for example with consensus-based distributed control [150], distributed finite-time control [151] and cooperative control via nearest-neighbour communications [152].

2.2 Frequency Stability in Weak Grids

With the increasing penetration of variable renewable energy in power systems, there is a greater need for robust operational tools to maintain system frequency stability after large generator and load contingency events. This issue is particularly important for weak islanded grids that are more sensitive to large active power perturbations [93]. Where synchronous generators are largely coherent across an entire system, then a low-order aggregate single-frequency model of the system can be appropriately used for frequency stability studies [94]. However, one of the key parameters to such models is the load relief factor (LRF), alternatively referred to as the load damping coefficient or load-frequency characteristic, which represents the natural sensitivity of loads in a network to system frequency.

The reliable estimation of the load-frequency characteristic at a system level is necessary for the accuracy of low-order aggregate single-frequency models. There have been a number of previous works such as [95-96] that have quoted system-level LRF, but have not provided any details on its derivation. Another set of studies have investigated load-frequency characteristics by conducting live tests such as the intentional tripping of generators and transmission lines. Ref. [97] performed tests for the Great Britain's grid but did not decouple the load response from the total system's response. Similarly, [98] performed tests for the Norwegian grid but the study did not investigate system wide quantities, rather focusing on load response measurements at specific locations. Likewise, [99] conducted tests for the Irish grid in which only one generator's governor was enabled while the others were locked (disabled) to isolate the load response.

Ref. [100] has estimated system LRFs for the UK grid using measurements from the Energy Management System (EMS) of total generation post-contingency (at 2-

second resolution). For smaller, weaker and less spatially dense systems like the Southwest Interconnected System (SWIS) in Western Australia, the EMS sampling resolution may not be high enough to accurately assess system load changes post-contingency, which is further exacerbated by the effects of time-averaging of generator output measurements spread out across a large geographic area, i.e., that are not time-synchronised via the global positioning system.

A new method for estimating system-level LRFs is offered in this thesis by using high-resolution fault recorder data, triggered during contingency events. The key advantages of the proposed approach are that (a) it uses available high-resolution data that is time-synchronised, and (b) no subjective inferences are required to determine the aggregate load response after a contingency.

2.3 **Interconnected Microgrids for Stability Support**

Two or more autonomous microgrid clusters can be interconnected in order to improve system stability and security by alleviating overloading, prevent load shedding and provide voltage support [46-48]. This is particularly useful for microgrid clusters based on intermittent renewable energy sources (e.g., solar PV) with limited energy storage [49-50]. For example, in the case when one autonomous microgrid has sufficient generation/storage capacity while a neighbouring microgrid has a deficiency in power.

Different interconnection types are possible, e.g., a simple ac connection [47], medium voltage backbone [51] or a common dc bus [52]. This research examines the interconnection via a back-to-back converter-based system. The main advantage of this interconnection type is that each microgrid can operate at any voltage and

frequency while they exchange active/reactive power through the back-to-back converters. Depending on the distance that the two neighbouring microgrids are situated, the dc link can have a length of zero to a few kilometres.

2.4 **PV Smoothing in Microgrids**

The use of battery energy storage systems to smooth out the fluctuations in the output power of PV is an attractive option for increasing the penetration of PV into a microgrid without causing system instability [53-54]. A smoothing battery can limit frequency deviations and reducing the wear and tear on conventional generators from excessive ramping [56]. The use of energy storage systems is commonly used for integrating renewable energy resources into microgrids [57-58].

Traditionally, the sizing of battery energy storage systems for smoothing the power fluctuations of PVs has been achieved by chronological/time-sequential simulation studies, where a smoothing algorithm is applied to the PV's output and the energy exchange between the battery and the power system is calculated at each time step [59-67]. Similar methods are also used in the smoothing of wind power fluctuations [68-74].

For the smoothing of PV fluctuations, the application of high-resolution solar irradiance data (i.e., less than 1-min) is necessary to adequately reflect the extents of short-term variability in solar irradiance [75]. However, several previous studies have used coarse 1-hour resolution data, which would introduce significant temporal smoothing from the solar irradiance data alone [62, 65].

Moreover, data for at least a year should be used for sizing a smoothing battery to capture seasonal variations in solar irradiance variability [60-64]. Some studies such

as [59, 66] have only considered data for one day, while [67] has examined only 1-hour of data.

Finally, while some studies such as [62-63, 67] make use of fully specified battery capacity models, many works have not considered the battery charge/discharge characteristics and have sized the battery capacity based on either the peak energy exchange [64-65] or the net energy exchange [66]. A battery capacity model is important as it is known that a battery's capacity tends to decrease with an increasing rate of charge or discharge [112]. In smoothing applications, the charge / discharge rate can be high depending on the level of smoothing required, thus there is a risk that a smoothing battery may be undersized if the battery charge/discharge characteristics are neglected. Furthermore, in some studies, there is no consideration for key parameters such as the battery's depth of discharge (DoD) and the initial state of charge (SoC) [64, 66].

It should be noted, however, that many of the previous works cited above are predominantly concerned with the control and performance aspects of different smoothing algorithms, and battery sizing is not their main emphasis. Moreover, while battery sizing for microgrid applications has been widely studied, few works specifically address the sizing of batteries purely for smoothing purposes (as opposed to time shifting energy) [62].

2.5 **Integrating PV into Weak Grids**

Grid code and network operator requirements for connecting PV plants are typically generic and written for large interconnected grids. As a result, they may not be suitable for analysing connections to weak grids, which are more sensitive to

frequency and/or voltage fluctuations [77]. Therefore, special attention needs to be given to address the key issues specific to weak grids. Power system modelling accuracy is also more crucial in weak grids as the margin for error is lower, and a single bad actor can lead to system-wide issues.

Although [78-79] have reviewed and presented network management techniques for weak grids, the majority of the literature on integrating renewable sources into weak grids such as [80-81] focus on the grid's sensitivity to either frequency and/or voltage, but do not provide any systematic methods or criteria for assessing grid impacts. A comprehensive review of generator connections to weak grids is provided in [77]; however, its discussions are applicable to all types of generators and is primarily a comparison of how different international grid codes relate to weak grids. Ref. [82-83] examine the issues related to grid integration of PV plants from the frequency and voltage stability perspective, but both works are more general in scope and do not explicitly consider weak grids. Ref. [76] and [84] consider the integration of PV plants from the utility operations perspective and identify the key challenges in frequency and voltage control while highlighting the need for better power system flexibility, but do not give any specific guidance for weak grids.

Ref. [85] provides a comprehensive review of connecting inverter-based resources into voltage-weak grids while [86-87] explore the integration of PV plants into weak radial distribution networks and emphasises on voltage control and quality issues only. Ref. [88] proposes a method for calculating the maximum penetration limit of PV plants in weak grids, taking into account grid weaknesses in frequency and voltage, but the applied method only considers transient frequency and voltage limits and is more applicable for project screening.

Ref. [89] discusses the importance of inertia in a power system and the operation of future power systems with high penetrations of inertia-less generation. While the paper is not confined to weak grids, it briefly discusses the operational issues encountered in low-inertia systems. Ref. [90-91] present case studies for integrating high penetration of PV plants into two small isolated systems and include analysis of frequency stability and generator dispatch patterns considering minimum machine loading.

Considering the abovementioned points, there is currently no coherent policy or framework for classifying, analysing and assessing the connection of PV plants to weak grids. Therefore, developing a coherent framework to analyse and evaluate the connection of utility-scale PV plants to weak grids is the research gap that part of this thesis will attempt to address. This is very important as grid code and network operator requirements for connecting PV plants are typically generic and developed for large interconnected grids. As a result, they may not be suitable for connections to weak grids, which are more sensitive to frequency and/or voltage fluctuations. As an example, a 5 MWp PV plant that was constructed and connected to a weak island grid in Nusa Tenggara Timur, Indonesia, had to be curtailed to 2 MWp at the operation stage as a result of observed grid instability issues that were not identified at the planning phase (because the material differences between the weak grids and large interconnected systems were largely ignored) [92].

Chapter 3 **Methodology**

This chapter presents the methodologies developed for the analysis and improvement of stability in microgrids and weak grids. The small-signal stability of converter dominated microgrids is first examined, where a load flow based technique to initialise the small-signal model is proposed. The structure for a back-to-back dc link to interconnect two microgrids is then discussed to improve frequency stability between geographically adjacent systems. Another frequency stability improvement method for microgrids, this time using smoothing batteries, is then proposed. The final two sections deal with the analysis of stability in weak grids: a framework for studying grid integration of PV into weak grids, and lastly, a new method for estimating the system load relief factor, a crucial input parameter used in frequency stability studies.

3.1 **Small-Signal Stability in Converter Dominated Microgrids**

The small-signal stability of inertia-less, pure converter based autonomous microgrids with decentralised control are considered in this section. A key feature of the considered system is the use of power-frequency droop control for load sharing between converters, a familiar technique that is used in synchronous power systems, but one that operates in a different manner in inertia-less systems.

3.1.1 **Power-Frequency Droop Control**

Power-frequency droop control is the standard approach for decentralised load sharing in conventional (synchronous) power systems. This has been adopted for pure converter-based power systems as well [13, 101]. However, the mechanisms for how power-frequency droop works in a converter-based system is very different to that of a synchronous system. In a synchronous power system, all directly-coupled synchronous machines rotate in unison at the same electrical frequency. Energy is stored in the inertia of rotating masses (shafts, fly-wheels, turbines, etc.) and this inertia responds instantaneously to supply mismatches in active power generation and load during load fluctuations. Oversupply or deficits of power are naturally transmitted throughout the system via a changing frequency.

Therefore, frequency has natural significance in a synchronous power system and indicates the mismatches between generation and load. But in a droop controlled converter-based microgrid, each voltage source converter (VSC) can generate voltages at any frequency desired, and the frequency of each VSC depends on its output active power. Therefore, there is no guarantee of a single frequency in the system, nor does frequency provide a naturally useful signal for active power mismatches. In fact, multiple frequencies are required in the system to facilitate active power exchange between VSCs as differences in frequency between two or more VSCs lead to the change of voltage phase angles and consequently, active power fluctuations. In other words, the VSC's active power output determines the frequency and differences in frequency between VSCs cause active power exchange, which leads to further adjustments in frequency and power exchange. The cycle repeats until all frequencies converge to an equilibrium point.

It is interesting to note that this is actually the opposite to how conventional droop works, where frequency determines output active power. The interactions between VSCs droops settings is one of the causes of small-signal instability in a microgrid, where instead of converging to a stable frequency as in Figure 3.1, VSCs' frequencies exhibit undamped oscillations and diverge.

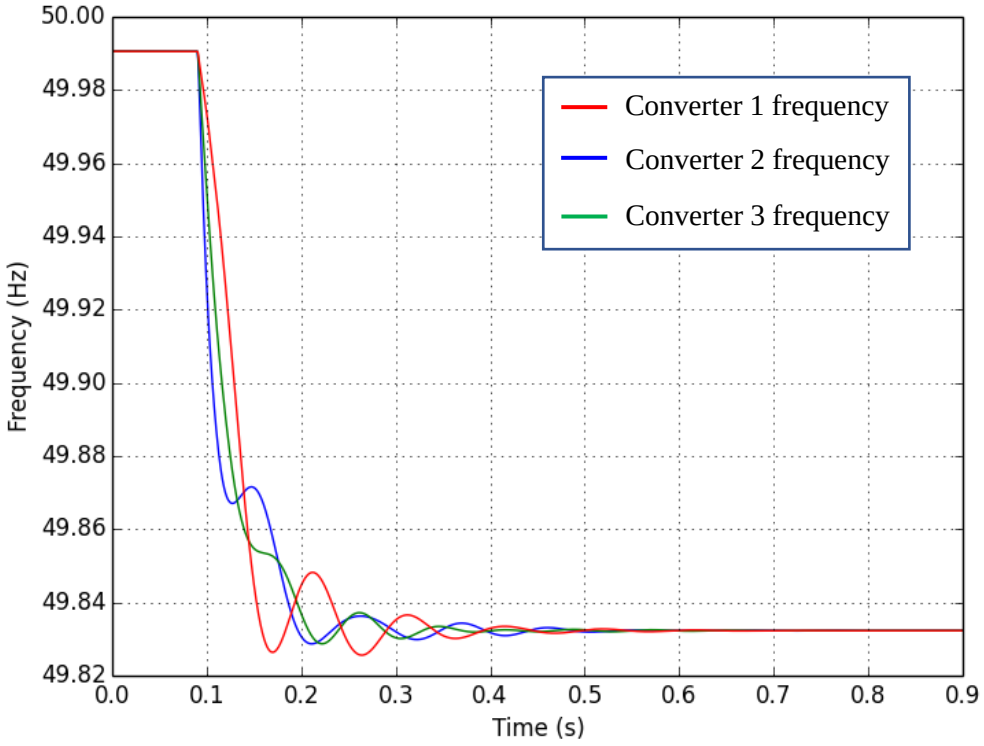

Figure 3.1. Power-frequency droop in converter-based systems

3.1.2 **Small-Signal Stability Model of a Microgrid**

The mathematical small-signal model for a microgrid comprising VSCs, RL lines and loads is now developed in the direct-quadrature (dq) reference frame. In order to form a complete system model from the individual component models, one VSC is designated as the common reference machine and the complete system is modelled in terms of its dq reference frame (called the common reference frame). As it is standard practice to model VSCs in terms of their own local

reference frame, VSC network interfaces (e.g., output voltage and current) are transformed to the common reference frame. In this study, capital letters D and Q denote quantities in the common reference frame whereas lowercase letters d and q denote quantities in the local frame. Also, lowercase letters denote state variables (e.g., i_o, v_o, i_l, etc.) while uppercase letters denote initial conditions or steady-state operating points (e.g., I_o, V_o, I_l, etc.), with the exception of Greek letters such as ω, where a 0-suffix is used to denote initial conditions, e.g., ω_0.

3.1.2.1 **Converter Model**

Converters are assumed to be three-leg, three phase VSCs interfaced to the microgrid via LCL filters. Each VSC is modelled as an ideal ac voltage source and dynamics on the dc side of the converter are not considered. The VSC control structure is shown below in Figure 3.2.

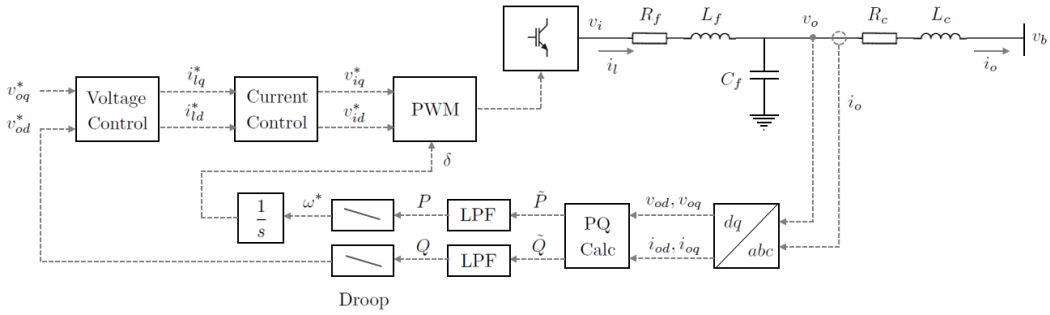

Figure 3.2. Generic voltage source converter with LCL filter frontend.

Details for each block of the VSC control structure are described in the following subsections:

i) dq Transformation: a dq transformation is required to convert time-domain network quantities $V_o(t)$ and $I_o(t)$ into dq coordinates for use in the converter control system. In this study, it is assumed that the synchronous

reference frame is perfectly known and additional control elements such as a phase-locked loop (PLL) are not considered.

ii) Power Measurement and Filtering: a power measurement block calculates the instantaneous active and reactive power measured at the output of the converter. The instantaneous power is then filtered via a low-pass filter (LPF) to suppress high frequency components. The combined power measurement and filtering blocks can be expressed as

$$\begin{aligned} \dot{P} &= \omega_c\left(v_{od}i_{od} + v_{oq}i_{oq} - P\right) \\ \dot{Q} &= \omega_c\left(v_{od}i_{oq} - v_{od}i_{oq} - Q\right) \end{aligned} \tag{3.1}$$

where ω_c is the cut-off frequency. The equations above can be linearised as

$$\begin{aligned} \Delta\dot{P} &= \omega_c\left(I_{od}\Delta v_{od} + I_{oq}\Delta v_{oq} + V_{od}\Delta i_{od} + V_{oq}\Delta i_{oq} - \Delta P\right) \\ \Delta\dot{Q} &= \omega_c\left(I_{oq}\Delta v_{od} - I_{od}\Delta v_{oq} - V_{oq}\Delta i_{od} + V_{od}\Delta i_{oq} - \Delta Q\right) \end{aligned} \tag{3.2}$$

iii) Droop Control: active power/frequency droop control is employed in order to facilitate active power sharing between converters

$$\begin{aligned} \omega &= \omega_n - mP \\ \dot{\delta} &= \omega - \omega_{com} \end{aligned} \tag{3.3}$$

where ω_n is the nominal frequency and m is the active power droop gain. ω_{com} is the common reference frequency and is the means by which individual converters modelled in their own local reference frame are connected together. One converter is designated as the reference converter and the angle δ represents the angle required to transform from a converter's local reference frame to the common reference frame. Eq. (3.3) can be linearised as

$$\begin{aligned} \Delta\omega &= -m\Delta P \\ \Delta\dot{\delta} &= -m\Delta P - \Delta\omega_{com} \end{aligned} \tag{3.4}$$

iv) Voltage and Current Controllers: as this work focuses on the stability margin based on the active power droop gain (i.e., the dominant parameter in small-signal stability of droop-controlled microgrids), the dynamics of the voltage and current controllers are not explicitly modelled and V_i is assumed to have a constant value (initialised from the steady-state load flow solution).

v) LCL Filter: each converter is interfaced to the microgrid via an LCL filter. The state space equations for the LCL filter are derived from Kirchhoff's laws and linearised as

$$\begin{aligned}
\Delta\dot{i}_{ld} &= -\frac{R_f}{L_f}\Delta i_{ld} + \omega_0 \Delta i_{lq} - \frac{1}{L_f}\Delta v_{od} + I_{lq}\Delta\omega \\
\Delta\dot{i}_{lq} &= -\omega_0 \Delta i_{ld} - \frac{R_f}{L_f}\Delta i_{lq} - \frac{1}{L_f}\Delta v_{oq} - I_{ld}\Delta\omega \\
\Delta\dot{v}_{od} &= \frac{1}{C_f}\Delta i_{ld} + \omega_0 \Delta v_{oq} - \frac{1}{C_f}\Delta i_{od} + V_{oq}\Delta\omega \\
\Delta\dot{v}_{oq} &= \frac{1}{C_f}\Delta i_{lq} - \omega_0 \Delta v_{od} - \frac{1}{C_f}\Delta i_{oq} - V_{od}\Delta\omega \\
\Delta\dot{i}_{od} &= \frac{1}{L_c}\Delta v_{od} - \frac{R_c}{L_c}\Delta i_{od} + \omega_0 \Delta i_{oq} - \frac{1}{L_c}\Delta v_{bd} + I_{oq}\Delta\omega \\
\Delta\dot{i}_{oq} &= \frac{1}{L_c}\Delta v_{oq} - \omega_0 \Delta i_{od} - \frac{R_c}{L_c}\Delta i_{oq} - \frac{1}{L_c}\Delta v_{bq} - I_{od}\Delta\omega
\end{aligned} \tag{3.5}$$

vi) Reference Frame Transformations: as the internal control elements for each converter are expressed in a local reference frame, any converter variable connected directly to the microgrid network (e.g., v_b and i_o) must be transformed to/from the common reference frame. The linearised equations for the transformed variables are

$$\begin{bmatrix}\Delta i_{oD} \\ \Delta i_{oQ}\end{bmatrix} = \begin{bmatrix}\cos\delta_0 & -\sin\delta_0 \\ \sin\delta_0 & \cos\delta_0\end{bmatrix}\begin{bmatrix}\Delta i_{od} \\ \Delta i_{oq}\end{bmatrix} + \begin{bmatrix}-\Delta i_{od}\sin\delta_0 - \Delta i_{oq}\cos\delta_0 \\ \Delta i_{od}\cos\delta_0 - \Delta i_{oq}\sin\delta_0\end{bmatrix}[\Delta\delta] \tag{3.6}$$

$$\begin{bmatrix}\Delta v_{bd}\\ \Delta v_{bq}\end{bmatrix} = \begin{bmatrix}\cos\delta_0 & \sin\delta_0\\ -\sin\delta_0 & \cos\delta_0\end{bmatrix}\begin{bmatrix}\Delta v_{bD}\\ \Delta v_{bQ}\end{bmatrix} + \begin{bmatrix}-\Delta v_{bD}\sin\delta_0 + \Delta v_{bQ}\cos\delta_0\\ -\Delta v_{bD}\cos\delta_0 - \Delta v_{bQ}\sin\delta_0\end{bmatrix}[\Delta\delta]$$

vii) Complete Converter Model: the complete converter state space model has nine state variables

$$\Delta\boldsymbol{x_{conv}} = \left[\Delta\delta\ \Delta P\ \Delta Q\ \Delta i_{ld}\ \Delta i_{lq}\ \Delta v_{od}\ \Delta v_{oq}\ \Delta i_{od}\ \Delta i_{oq}\ \right]' \tag{3.7}$$

The state equations for the converter can be expressed as

$$\Delta\dot{\boldsymbol{x}}_{\boldsymbol{conv}} = \boldsymbol{A_{conv}}\Delta\boldsymbol{x_{conv}} + \boldsymbol{B_{conv}}\begin{bmatrix}\Delta V_{bD}\\ \Delta V_{bQ}\end{bmatrix} + \boldsymbol{B_{\omega}}\Delta\omega_{com} \tag{3.8}$$

where

$$\mathbf{A}_{\boldsymbol{conv}} = \begin{bmatrix}
0 & -m & 0 & 0 & 0 & 0 & 0 & 0 & 0\\
0 & -\omega_c & 0 & 0 & 0 & \omega_c I_{od} & \omega_c I_{oq} & \omega_c V_{od} & \omega_c V_{oq}\\
0 & 0 & -\omega_c & 0 & 0 & \omega_c I_{od} & -\omega_c I_{od} & -\omega_c V_{oq} & \omega_c V_{od}\\
0 & mI_{lq} & 0 & -\frac{R_f}{L_f} & \omega_0 & -\frac{1}{L_f} & 0 & 0 & 0\\
0 & -mI_{ld} & 0 & -\omega_0 & -\frac{R_f}{L_f} & 0 & -\frac{1}{L_f} & 0 & 0\\
0 & mV_{oq} & 0 & \frac{1}{C_f} & 0 & 0 & \omega_0 & -\frac{1}{C_f} & 0\\
0 & -mV_{od} & 0 & 0 & \frac{1}{C_f} & -\omega_0 & 0 & 0 & -\frac{1}{C_f}\\
\frac{1}{L_c}\left(V_{bD}\sin\delta_0 - V_{bQ}\cos\delta_0\right) & mI_{oq} & 0 & 0 & 0 & \frac{1}{L_c} & 0 & -\frac{R_c}{L_c} & \omega_0\\
\frac{1}{L_c}\left(V_{bD}\cos\delta_0 + V_{bQ}\sin\delta_0\right) & -mI_{od} & 0 & 0 & 0 & 0 & \frac{1}{L_c} & -\omega_0 & -\frac{R_c}{L_c}
\end{bmatrix}$$

$$\mathbf{B}_{\boldsymbol{conv}} = \begin{bmatrix}
0 & 0 & 0 & 0 & 0 & 0 & 0 & -\frac{1}{L_c}\cos\delta_0 & -\frac{1}{L_c}\sin\delta_0\\
0 & 0 & 0 & 0 & 0 & 0 & 0 & \frac{1}{L_c}\sin\delta_0 & -\frac{1}{L_c}\cos\delta_0
\end{bmatrix}'$$

$$\boldsymbol{B_{\omega}} = [-1\ 0\ 0\ 0\ 0\ 0\ 0\ 0\ 0\ ]'$$

Linearised network quantities $\Delta\omega$, Δi_{oD} and Δi_{oQ} can be written as

$$\left[\Delta\omega\ \Delta i_{oD}\ \Delta i_{oQ}\ \right]' = [\boldsymbol{C_{\omega}}\ \boldsymbol{C_{io}}\ ]'\Delta\boldsymbol{x_{conv}} \tag{3.9}$$

where

$$\boldsymbol{C_{\omega}} = [0\ -m\ 0\ 0\ 0\ 0\ 0\ 0\ 0\ ]$$

$$\mathbf{C}_{\boldsymbol{io}} = \begin{bmatrix}
-I_{od}\sin\delta_0 - I_{oq}\cos\delta_0 & 0 & 0 & 0 & 0 & 0 & 0 & \cos\delta_0 & -\sin\delta_0\\
I_{od}\cos\delta_0 - I_{oq}\sin\delta_0 & 0 & 0 & 0 & 0 & 0 & 0 & \sin\delta_0 & \cos\delta_0
\end{bmatrix}$$

3.1.2.2 **Branch / Line Model**

Microgrid branches / lines are represented by series RL elements. The dynamic equations for a line connecting nodes i and j can be expressed as

$$\begin{aligned} \dot{i}_{line,D} &= \frac{1}{L_{line}}\left(v_{bD,i} - v_{bD,j} - R_{line} i_{line,D}\right) + \omega i_{line,Q} \\ \dot{i}_{line,Q} &= \frac{1}{L_{line}}\left(v_{bQ,i} - v_{bQ,j} - R_{line} i_{line,Q}\right) - \omega i_{line,D} \end{aligned} \tag{3.10}$$

where R_{line} and L_{line} are the resistance and inductance of the branch/line respectively. Eq. (3.10) can be linearised as

$$\begin{aligned} \Delta\dot{i}_{line,D} &= -\frac{R_{line}}{L_{line}}\Delta i_{line,D} + \omega_0 \Delta i_{line,Q} + \frac{1}{L_{line}}\left(\Delta v_{bD,i} - \Delta v_{bD,j}\right) + I_{line,Q}\Delta\omega \\ \Delta\dot{i}_{line,Q} &= -\omega_0 \Delta i_{line,D} - \frac{R_{line}}{L_{line}}\Delta i_{line,Q} + \frac{1}{L_{line}}\left(\Delta v_{bQ,i} - \Delta v_{bQ,j}\right) - I_{line,D}\Delta\omega \end{aligned} \tag{3.11}$$

3.1.2.3 **Load Model**

Microgrid loads are modelled as shunt RL (constant impedance) elements. The dynamic equations for a load connected to node i can be expressed as

$$\begin{aligned} \dot{i}_{load,D} &= \frac{1}{L_{load}}\left(v_{bD,i} - R_{load} i_{load,D}\right) + \omega i_{load,Q} \\ \dot{i}_{load,Q} &= \frac{1}{L_{load}}\left(v_{bQ,i} - R_{load} i_{load,Q}\right) - \omega i_{load,D} \end{aligned} \tag{3.12}$$

where R_{load} and L_{load} are the resistance and inductance of the load respectively. Eq. (3.12) can be linearised as

$$\begin{aligned} \Delta\dot{i}_{load,D} &= -\frac{R_{load}}{L_{load}}\Delta i_{load,D} + \omega_0 \Delta i_{load,Q} + \frac{1}{L_{load}}\Delta v_{bD,i} + I_{load,Q}\Delta\omega \\ \Delta\dot{i}_{load,Q} &= -\omega_0 \Delta i_{load,D} - \frac{R_{load}}{L_{load}}\Delta i_{load,Q} + \frac{1}{L_{load}}\Delta v_{bQ,i} - I_{load,D}\Delta\omega \end{aligned} \tag{3.13}$$

3.1.2.4 **Network Topology Model**

The dynamic equations for the microgrid converters, branches/lines and loads are expressed as ordinary differential equations (ODEs) of current injections with node voltages V_{bd} and V_{bq} as inputs. Thus, well-defined node voltages are required to interface the individual component models to the network. This is achieved by the virtual resistor method, which is simple and has been found to have minimal influence on small-signal stability [22]. With this method, the voltage at node i is calculated as

$$\begin{aligned} v_{bD,i} &= R_v\left(i_{oD,i} - i_{load,D,i} + \sum i_{line,D,i}\right) \\ v_{bQ,i} &= R_v\left(i_{oQ,i} - i_{load,Q,i} + \sum i_{line,Q,i}\right) \end{aligned} \tag{3.14}$$

where R_v is the virtual resistor, $i_{o,i}$ is the current injection from a converter at node i, $i_{load,i}$ is the current delivered to a load at node i, and $\sum i_{line,i}$ is the sum of current injections from lines connected to node i.

For a microgrid with N nodes, U converters, W loads and Z lines, the linearised bus voltages can be represented in matrix form as

$$\begin{aligned} &\left[\Delta v_{bD,1}\ \Delta v_{bQ,1}\ \cdots\ \Delta v_{bD,N}\ \Delta v_{bQ,N}\ \right]' \\ &= R_v \boldsymbol{M_{conv}}\left[\Delta i_{oD,1}\ \Delta i_{oQ,1}\ \cdots\ \Delta i_{oD,U}\ \Delta i_{oQ,U}\ \right]' \\ &+ R_v \boldsymbol{M_{load}}\left[\Delta i_{load,D,1}\ \Delta i_{load,Q,1}\ \cdots\ \Delta i_{load,D,W}\ \Delta i_{load,Q,W}\ \right]' \\ &+ R_v \boldsymbol{M_{line}}\left[\Delta i_{line,D,1}\ \Delta i_{line,Q,1}\ \cdots\ \Delta i_{line,D,Z}\ \Delta i_{line,Q,Z}\ \right]' \end{aligned} \tag{3.15}$$

where $\boldsymbol{M_{conv}}$, $\boldsymbol{M_{load}}$ and $\boldsymbol{M_{line}}$ are mapping matrices for the converters, loads and lines respectively. The mapping matrices reflect the network topology and show how individual component models are connected together. The convention used in this study is to have a +1 entry in the mapping matrix for a current entering a node (e.g., sources), and -1 entry for a current exiting a node (e.g., loads).

For U converters, the mapping matrix $\boldsymbol{M_{conv}}$ has dimensions $2N \times 2U$, and is composed such that the ith converter connected to the jth node has entries in the form of

$$\boldsymbol{M_{conv}}(2j-1,2i-1) = 1, \boldsymbol{M_{conv}}(2j,2i) = 1 \tag{3.16}$$

For W loads, the mapping matrix $\boldsymbol{M_{load}}$ has dimensions $2N \times 2W$ and the ith load connected to the jth node has entries in the form of

$$\boldsymbol{M_{load}}(2j-1,2i-1) = -1, \boldsymbol{M_{load}}(2j,2i) = -1 \tag{3.17}$$

For Z lines, the mapping matrix $\boldsymbol{M_{line}}$ has dimensions $2N \times 2Z$ and for the ith line connected to nodes j and k, the entries in M_{line} are in the form of

$$\begin{aligned} &\boldsymbol{M_{line}}(2j-1,2i-1) = -1, \boldsymbol{M_{line}}(2j,2i) = -1 \\ &\boldsymbol{M_{line}}(2k-1,2i-1) = 1, \boldsymbol{M_{line}}(2k,2i) = 1 \end{aligned} \tag{3.18}$$

3.1.2.5 **Complete Microgrid Model**

The combined model for the converters can be given as

$$\Delta \dot{\boldsymbol{x}}_{\boldsymbol{convs}} = \boldsymbol{A_{convs}} \Delta \boldsymbol{x_{convs}} + \boldsymbol{B_{convs}} \boldsymbol{M'_{conv}} \Delta \boldsymbol{v_{bDQ}} \tag{3.19}$$

where

$$\Delta \boldsymbol{x_{convs}} = \left[\Delta x_{conv,1}\ \Delta x_{conv,2}\ \cdots\ \Delta x_{conv,U}\ \right]'$$

$$\Delta \boldsymbol{v_{bDQ}} = \left[\Delta v_{bD,1}\ \Delta v_{bQ,1}\ \cdots\ \Delta v_{bD,N}\ \Delta v_{bQ,N}\ \right]'$$

$$\boldsymbol{A_{convs}} = diag\left(A_{conv,1}\ \cdots\ A_{conv,U}\ \right) + \left[B_{\omega,1}\ B_{\omega,2}\ \cdots\ B_{\omega,U}\ \right]'[0\ m\ 0\ \cdots\ 0\ ]$$

$$\boldsymbol{B_{convs}} = diag\left(B_{conv,1}\ \cdots\ B_{conv,U}\ \right)$$

The combined model for the lines can be given as

$$\Delta \dot{\boldsymbol{x}}_{\boldsymbol{lines}} = \boldsymbol{A_{lines}} \Delta \boldsymbol{x_{lines}} + \boldsymbol{B_{1lines}} \boldsymbol{M'_{line}} \Delta \boldsymbol{v_{bDQ}} + \boldsymbol{B_{2lines}} \Delta \omega_{com} \tag{3.20}$$

where

$$\Delta \boldsymbol{x_{lines}} = \left[\Delta x_{line,1}\ \Delta x_{line,2}\ \cdots\ \Delta x_{line,U}\ \right]'$$

$$\boldsymbol{A_{lines}} = diag\left(A_{line,1}\ \cdots\ A_{line,U}\ \right)$$

$$\boldsymbol{B_{1lines}} = diag\left(\frac{1}{L_{line,1}}, \frac{1}{L_{line,1}}, \cdots, \frac{1}{L_{line,Z}}, \frac{1}{L_{line,Z}}\right)$$

$$\boldsymbol{B_{2lines}} = \left[I_{line,Q,1} - I_{line,D,1} \ \cdots \ I_{line,Q,Z} - I_{line,D,Z}\right]'$$

Similarly, the combined model for loads can be described as

$$\Delta \dot{\boldsymbol{x}}_{\boldsymbol{loads}} = \boldsymbol{A_{loads}} \Delta \boldsymbol{x_{loads}} + \boldsymbol{B_{1loads}} \boldsymbol{M'_{load}} \Delta \boldsymbol{v_{bDQ}} + \boldsymbol{B_{2loads}} \Delta \omega_{com} \tag{3.21}$$

where

$$\Delta \boldsymbol{x_{loads}} = \left[\Delta x_{load,1} \ \Delta x_{load,2} \ \cdots \ \Delta x_{load,V}\right]'$$

$$\boldsymbol{A_{loads}} = diag\left(A_{load,1} \ \cdots \ A_{load,V}\right)$$

$$\boldsymbol{B_{1loads}} = diag\left(\frac{1}{L_{load,1}}, \frac{1}{L_{load,1}}, \cdots, \frac{1}{L_{load,V}}, \frac{1}{V}\right)$$

$$\boldsymbol{B_{2loads}} = \left[I_{load,Q,1} - I_{load,D,1} \ \cdots \ I_{load,Q,V} - I_{load,D,V}\right]'$$

The complete model for a microgrid can be formed by combining all of the components together into a single state-space matrix as

$$\Delta \dot{\boldsymbol{x}}_{\boldsymbol{MG}} = \boldsymbol{A_{MG}} \Delta \boldsymbol{x_{MG}} \tag{3.22}$$

where

$$\Delta \boldsymbol{x_{MG}} = \left[\Delta \boldsymbol{x_{convs}} \ \Delta \boldsymbol{x_{lines}} \ \Delta \boldsymbol{x_{loads}}\right]'$$

$$\mathbf{A_{MG}} = \begin{bmatrix} \mathbf{A}_{convs} + \mathbf{B}_{convs}\mathbf{M}'_{conv}R_v\mathbf{M}_{conv}\mathbf{C}_{io} & \mathbf{B}_{convs}R_v\mathbf{M}_{line} & \mathbf{B}_{convs}R_v\mathbf{M}_{load} \\ \mathbf{B}_{1lines}\mathbf{M}'_{line}R_v\mathbf{M}_{conv}\mathbf{C}_{io} + \mathbf{B}_{2lines}\mathbf{C}_{\omega} & \mathbf{A}_{lines} + \mathbf{B}_{1lines}\mathbf{M}'_{line}R_v\mathbf{M}_{line} & \mathbf{B}_{1lines}\mathbf{M}'_{line}R_v\mathbf{M}_{load} \\ \mathbf{B}_{1loads}\mathbf{M}'_{load}R_v\mathbf{M}_{conv}\mathbf{C}_{io} + \mathbf{B}_{2loads}\mathbf{C}_{\omega} & \mathbf{B}_{1loads}\mathbf{M}'_{load}R_v\mathbf{M}_{line} & \mathbf{A}_{loads} + \mathbf{B}_{1loads}\mathbf{M}'_{load}R_v\mathbf{M}_{load} \end{bmatrix}$$

3.1.3 **Load Flow Initialisation of Microgrid Model**

Initial conditions for the small-signal model are determined first by calculating the steady-state operating point using a standard load flow simulation, and then using these results to calculate initial conditions for each component model (e.g., converter, line and load models). Initial values for the component

models are determined by solving the dynamic equations with all derivatives set to zero.

The first step is to obtain steady-state network quantities (voltages, power flows, etc) from a load flow simulation. Nodal current injections can then be computed for each converter based on the load flow results. It is assumed that the system is operating at nominal frequency, i.e., $\omega_0 = \omega_n$, although an arbitrary initial operating frequency can be used if desired (note that line reactances would need to be adjusted accordingly in the load flow model).

3.1.3.1 **Initial Conditions for Converters**

For each converter, the bus voltage V_b and bus current injection Io is known from the load flow solution. The other quantities that need to be initialised in the converter model (V_i, V_o and I_l) can be calculated by solving the system of linear equations:

$$\begin{bmatrix} \frac{1}{L_f} & 0 & -\frac{R_f}{L_f} & \omega_0 & -\frac{1}{L_f} & 0 \\ 0 & \frac{1}{L_f} & -\omega_0 & -\frac{R_f}{L_f} & 0 & -\frac{1}{L_f} \\ 0 & 0 & \frac{1}{C_f} & 0 & 0 & \omega_0 \\ 0 & 0 & 0 & \frac{1}{C_f} & -\omega_0 & 0 \\ 0 & 0 & 0 & 0 & \frac{1}{L_c} & 0 \\ 0 & 0 & 0 & 0 & 0 & \frac{1}{L_c} \end{bmatrix} \begin{bmatrix} V_{id} \\ V_{iq} \\ I_{ld} \\ I_{lq} \\ V_{od} \\ V_{oq} \end{bmatrix} = \begin{bmatrix} 0 & 0 & 0 & 0 \\ 0 & 0 & 0 & 0 \\ 0 & 0 & \frac{1}{C_f} & 0 \\ 0 & 0 & 0 & \frac{1}{C_f} \\ \frac{1}{L_c} & 0 & \frac{R_c}{L_c} & -\omega_0 \\ 0 & \frac{1}{L_c} & \omega_0 & \frac{R_c}{L_c} \end{bmatrix} \begin{bmatrix} V_{bd} \\ V_{bq} \\ I_{od} \\ I_{oq} \end{bmatrix} \quad (3.23)$$

The initial converter angle relative to the network reference frame can be calculated based on the converter control strategy. For example, if the control

strategy is to align the output voltage V_o to the d-axis (i.e., $V_{oq} = 0$), then the initial converter angle δ_0 is calculated from:

$$\delta_0 = \left(\frac{V_{oq}}{V_{od}}\right) \tag{3.24}$$

3.1.3.2 **Initial Conditions for Branches / Lines**

For each line, the bus voltages at each end of the line ($V_{b,i}$ and $V_{b,j}$) are known from the load flow solution. The load current I_{line} can be calculated by solving:

$$\begin{bmatrix} \frac{R_{line}}{L_{line}} & -\omega_0 \\ \omega_0 & \frac{R_{line}}{L_{line}} \end{bmatrix} \begin{bmatrix} I_{line,d} \\ I_{line,q} \end{bmatrix} = \begin{bmatrix} \frac{1}{L_{line}} & -\frac{1}{L_{line}} & 0 & 0 \\ 0 & 0 & \frac{1}{L_{line}} & -\frac{1}{L_{line}} \end{bmatrix} \begin{bmatrix} V_{bd,i} \\ V_{bq,i} \\ V_{bd,j} \\ V_{bq,j} \end{bmatrix} \tag{3.25}$$

3.1.3.3 **Initial Conditions for Loads**

For each load, the bus voltage V_b is known from the load flow solution. In a standard load flow model, loads are typically described as constant PQ loads, which need to be converted to RL loads. This can be done by calculating the complex impedance from the bus voltage and load power consumption from:

$$Z_{load} = \frac{V_b^2}{S_{load}} = R_{load} + j\omega_0 L_{load} \tag{3.26}$$

Finally, the load current I_{load} can be calculated by solving the following linear system:

$$\begin{bmatrix} \frac{R_{load}}{L_{load}} & -\omega_0 \\ \omega_0 & \frac{R_{load}}{L_{load}} \end{bmatrix} \begin{bmatrix} I_{load,d} \\ I_{load,q} \end{bmatrix} = \begin{bmatrix} \frac{1}{L_{load}} & 0 \\ 0 & \frac{1}{L_{load}} \end{bmatrix} \begin{bmatrix} V_{bd} \\ V_{bq} \end{bmatrix} \tag{3.27}$$

3.2 **Interconnecting Microgrids for Dynamic Frequency Support**

The proposed system structure in this section considers two neighbouring microgrid clusters, situated at a close distance within a geographical area and interconnected via a back-to-back dc link as shown in Figure 3.3a.

(a)

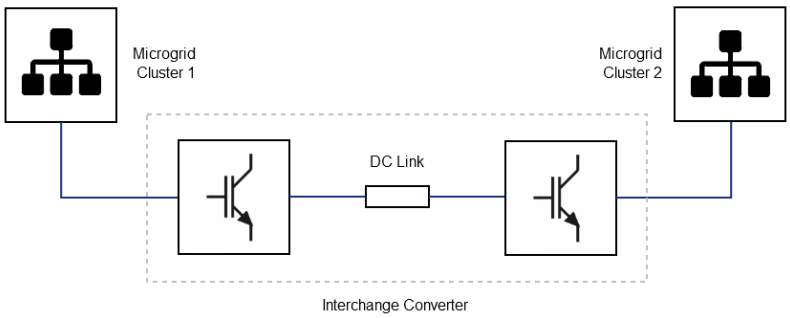

(b)

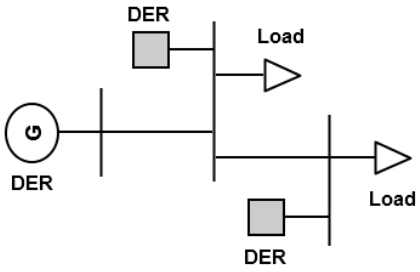

(c)

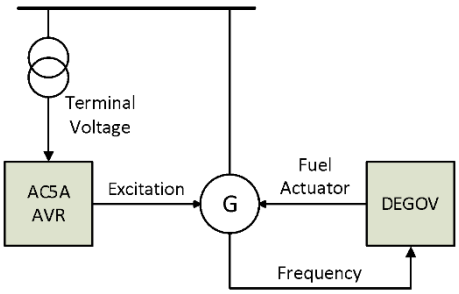

(d)

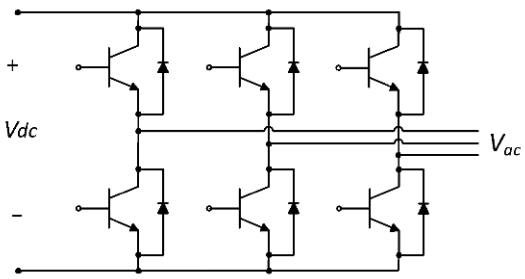

Figure 3.3. Schematic diagram of power supply system for remote areas: (a) Two neighbouring autonomous microgrids interconnected via interchange (back-to-back) converter, (b) Microgrid system consisting of two converter-interfaced DERs, one diesel generator and one local load, (c) Diesel generator set, (d) VSC system of the converter-interfaced DERs

3.2.1 **Microgrid Cluster Structure and Control**

Two similar hybrid microgrid clusters are assumed. Each microgrid cluster consists of two converter-interfaced DERs and one inertial DER. The DERs are assumed to have voltage Source Converters (VSCs) while the inertial DER is assumed to be a diesel generator. Figure 3.3b shows the topological structure considered for each microgrid cluster.

The diesel generator set is modelled dynamically with the simple Siemens DEGOV diesel governor model [102] and the IEEE AC5A exciter model [103]. The diesel generator set is as shown in Figure 3.3c. Each converter is composed of a three-phase, three-leg VSC structure as shown in Figure 3.3d.

Each microgrid has a hierarchical control system to maintain the frequency and voltage deviations within an acceptable range while the DERs supply the required active/reactive power demand of the local loads. The hierarchical control system for each microgrid is based on a three-level control system, similar to that used in large power systems, but is adapted for the microgrid [17, 101]. These three levels are:

a) **Primary control:** This controller consists of two loops: i) an inner loop and ii) an outer loop. The inner loop is responsible for regulating the output current and voltage of each converter-based DER. The outer-loop is responsible for defining the set-points for the inner-loop using the droop control and based on the set-points defined from the secondary controller.

   For inertial DERs (i.e., diesel generator), the primary controller consists of a mechanically-actuated diesel engine governor with droop control.

b) **Secondary control:** This controller is responsible to define the proper set-points for the primary controllers of each DER such that the frequency and voltage within the microgrid is kept within the acceptable ranges.

c) **Tertiary control:** This controller facilitates the power exchange through the interchange converter between the two microgrids. This control system is discussed in more detail in Section 0.

In the proposed control scheme, a synchronous based diesel generator provides the reference voltage and frequency (though in principle, a grid-forming converter could also be used for this purpose). A more detailed description of the primary and secondary control scheme follows.

3.2.1.1 **Primary Control Scheme**

For converter-based DERs, a vector current control approach in the Direct-Quadrature (dq) reference frame is used for the inner control loop of each converter. The three-phase currents at the output of the converter (I_{abc}) are transferred to their equivalent direct-axis current (I_d) and quadrature-axis current (I_q). These two currents are regulated to their reference values (i.e., $I_{d,ref}$ and $I_{q,ref}$) by the help of Proportional-Integral (PI) controllers.

The outputs of the inner current controller are the modulation indices in the *dq* reference frame, which are then converted to the stationary *abc* frame and fed into the converter PWM modulator block [104]. This control block diagram is shown in Figure 3.4.

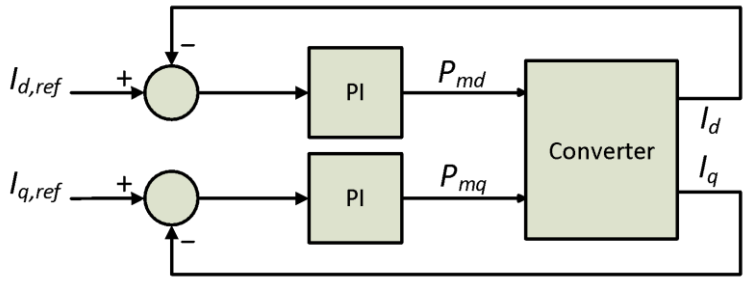

Figure 3.4. Control block diagram of the microgrid Primary Control level

Voltage and frequency droop control serves as the primary control strategy for each DER (synchronous and converter-based alike). The primary control structure is based on the standard droop equations as

$$f = f_{ref} - m(P - P_{ref}) \tag{3.28}$$

$$V = V_{ref} - n(Q - Q_{ref}) \tag{3.29}$$

where f and V are respectively the frequency and voltage of the microgrid and f_{ref} and V_{ref} are the references for these parameters, P and Q are the average three-phase active and reactive power output of the DER and P_{ref} and Q_{ref} are the references for these parameters, and m and n are the frequency and voltage droop coefficients. It is to be noted that the reference values and the droop coefficients are defined by the secondary controller to provide a desired power ratio among the DERs as well as to hold the voltage and frequency within the acceptable ranges.

The droop coefficients are defined by the secondary controller

$$m = \Delta f / P_{max} \tag{3.30}$$

$$n = \Delta V / 2Q_{max} \tag{3.31}$$

where Δf and ΔV are the maximum frequency and voltage deviations allowed and P_{max} and Q_{max} are the maximum active and reactive power output of the DER.

For converter-based DERs, the control of P and Q are achieved through the adjustment of inner control loop reference set-points (i.e., $I_{d,ref}$ and $I_{q,ref}$) from

$$I_{d,ref} = P_{ref} + (f_{ref} - f)/m \tag{3.32}$$

$$I_{q,ref} = Q_{ref} + (V_{ref} - V)/n \tag{3.33}$$

3.2.1.2 **Secondary Control Scheme**

The secondary controller adjusts the active and reactive power reference signals P_{ref} and Q_{ref} in order to regulate frequency and voltage to nominal values. Secondary control is intended to operate after primary control action has taken place, and so the time steps for the secondary controller are relatively larger compared to that of the primary controller (e.g., 3s vs 10ms).

In the secondary controller, new active and reactive power set-points are calculated at discrete time intervals (e.g., every 3s) from

$$P_{ref} = P + m(f - f_{ref}) \tag{3.34}$$

$$Q_{ref} = Q + n(V - V_{ref}) \tag{3.35}$$

3.2.2 **Interchange Converter**

A back-to-back converter arrangement is proposed as a means to interconnect the two neighbouring microgrids. This converter will provide frequency support for the two microgrids in the case of power deficiency in one of the microgrids while the other microgrid has enough generation/storage capability. The tertiary control scheme is applied to control the dynamic performance of the interchange converter to support two interconnected microgrids. Each converter is composed of a three-phase, three-leg VSC structure

as shown in Figure 3.3d.

Each converter in the proposed back-to-back converter arrangement has an individual controller that is configured to regulate the voltage of the dc link and provide frequency support to both microgrids. The control block diagram for each of these converters is shown in Figure 3.5a.

Each controller participates in controlling both the dc link voltage and the frequency of the microgrid. For this, an error signal (ζ) is calculated as

$$\zeta = k_{dc}\left(V_{dc,ref} - V_{dc}\right) + k_f\left(f_{ref} - f\right) \tag{3.36}$$

where V_{dc} is the dc voltage at the terminals of the converter and $V_{dc,ref}$ is its reference value and k_f and k_{dc} are the controller coefficients. This error signal is then passed through a PI controller to generate $I_{d,ref}$ for the converter. This is referred to as the active power controller module and is shown schematically in Figure 3.5b. The current controller for the interchange converter is a based on a PI controller, similar to the inner-loop control of the DER converters.

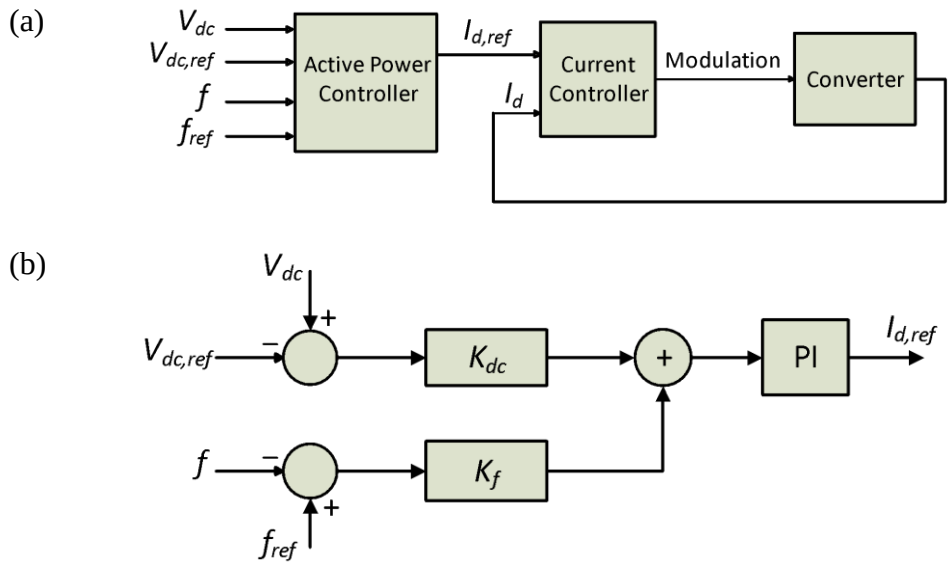

Figure 3.5. (a) Control block diagram of the interchange converter, (b) Active power controller module of the interchange converter..

3.3 Optimal Smoothing Battery Sizing for PV-Diesel Microgrids

This section describes the proposed method for optimally sizing a BESS to smooth out active power fluctuations in a PV-diesel microgrid so as to improve frequency stability and maximise the penetration of PV into the system.

3.3.1 Solar Irradiance Variability

One of the key features of the proposed method is the explicit consideration of the solar irradiance variability index (SIVI) for sizing a smoothing battery. This is because different geographical locations are subject to different levels of SIVI over a calendar year, and consequently, the sites with low SIVI do not require as much smoothing as the sites with higher SIVI.

The solar irradiance dataset, used in this study, is based on the 2017 measurement data of the global horizontal irradiance (GHI), with a 1-minute resolution, captured from the Australian Government's Bureau of Meteorology [105]. This data was retrieved for 11 weather station locations around Australia, as listed in Table 3.1. The selected areas vary from urban (site-1, 6) to rural (site-4, 8) locations, coastal (site-7, 8, 9) to inland areas (site-2, 5), and hot (site-3, 11) to cold (site-4, 10) regions.

Table 3.1 Considered study sites in this thesis

Site No	Name	State	Latitude (°)	Longitude (°)
1	Adelaide	South Australia	-34.9285	138.6007
2	Alice Springs	Northern Territory	-23.6980	133.8807
3	Rockhampton	Queensland	-23.3791	150.5100
4	Cape Grim	Tasmania	-40.6833	144.6833
5	Kalgoorlie	Western Australia	-30.7490	121.4660

Site No	Name	State	Latitude (°)	Longitude (°)
6	Darwin	Northern Territory	-12.4634	130.8456
7	Broome	Western Australia	-17.9614	122.2359
8	Learmonth	Western Australia	-22.2312	114.0888
9	Geraldton	Western Australia	-28.7774	114.6150
10	Wagga	New South Wales	-35.1082	147.3598
11	Townsville	Queensland	-19.2590	146.8169

Fluctuations in the solar irradiance throughout a full day, at a specific location, can be quantified as a single number using the SIVI in the form of [106]

$$SIVI = \frac{\sum_{t=1}^{T-1}\sqrt{[GHI(t+1) - GHI(t)]^2 + \Delta T^2}}{\sum_{t=1}^{T-1}\sqrt{\left[GHI_{clear-sky}(t+1) - GHI_{clear-sky}(t)\right]^2 + \Delta T^2}} \tag{3.37}$$

where GHI is the measured global horizontal irradiance (W/m^2), $GHI_{clear-sky}$ is the clear-sky irradiance and ΔT is the averaging interval while T is the number of consecutive measurements (e.g., given a minute-averaged time series, $\Delta T = 1$ and $T = 1440$ for a 24-hour period).

The SIVI provides a useful measure for classifying different days based on their solar intermittency relative to the expected clear-sky irradiance profile. An SIVI of close to unity represents the ideal clear-sky day (refer to Figure 3.6a, as an example, captured from site-1 on 25/01/2017), while a high SIVI is more representative of a mixed-sky day (refer to Figure 3.6b, captured from the same site on 06/11/2017). Note that an overcast day may have a low SIVI despite having uniformly low irradiance throughout the day (as an example, see Figure 3.6d, captured from the same site on 16/07/2017).

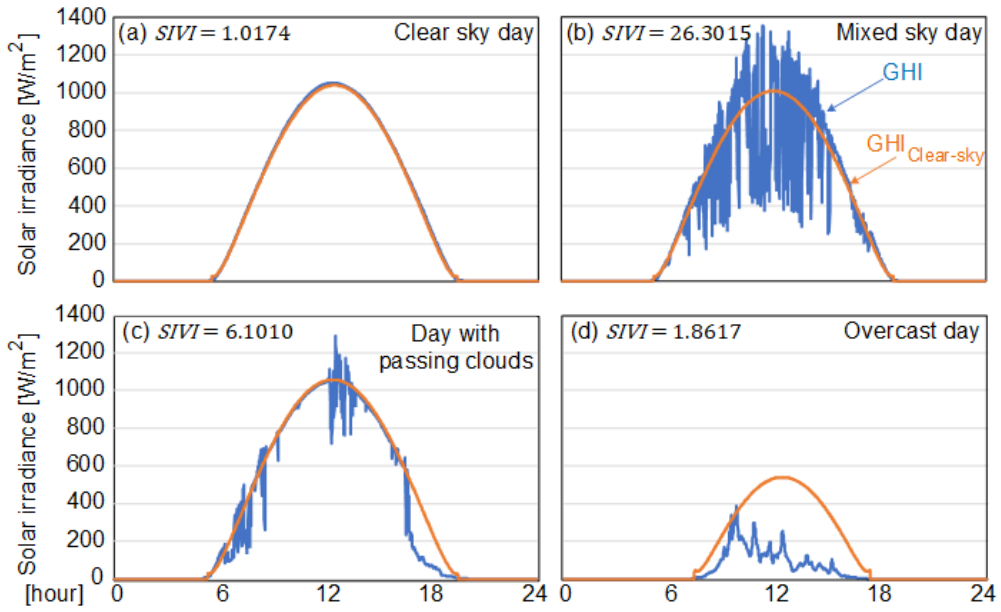

Figure 3.6. Solar irradiance and the corresponding SIVI for 4 sample days at site-1: (a) a clear sky day, (b) a day with frequent cloud movements, (c) a clear day with a few passing clouds throughout the day and an overcast period in the afternoon, (d) an overcast day

The SIVI for a single location can be calculated for each day in the available dataset with a minimum of one year to cover seasonal variations and combined to form empirical cumulative distribution functions (CDFs). The CDFs provide insights into a site's SIVI over time.

Figure 3.7 illustrates the empirical CDFs for site-1 to 4 of Table 3.1 in 2017. As seen in Figure 3.7b, Site-2 shows SIVIs that are close to unity for over 40% of the year, indicating a site that has consistent clear sky days. On the other hand, as seen in Figure 3.7c, Site-3 exhibits a much higher spread in the SIVI, suggesting a site with a higher prevalence of mixed-sky days.

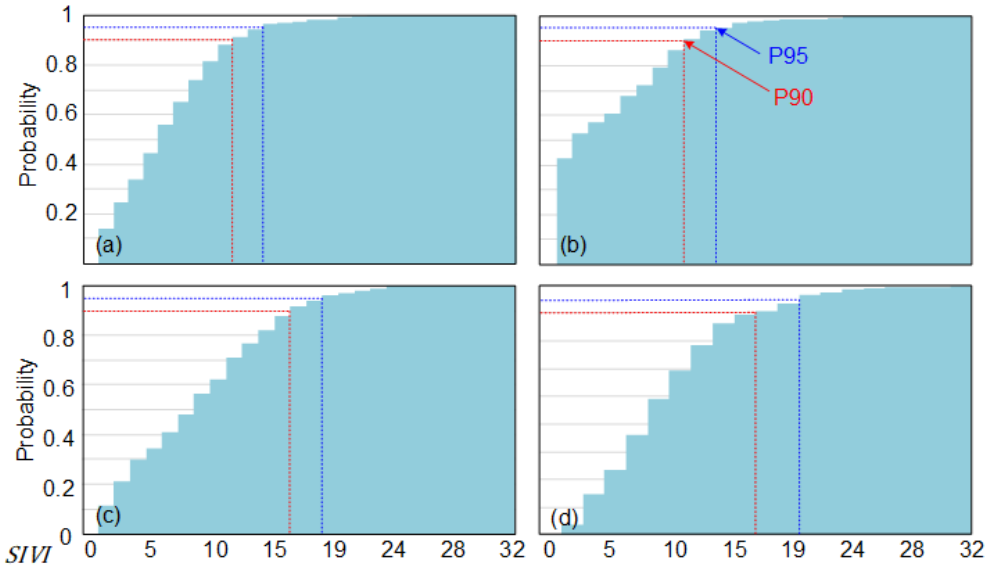

Figure 3.7. Empirical CDF for SIVI in 2017 at (a) site-1, (b) site-2, (c) site-3, (d) site-4

The SIVI data in the CDFs can also be represented as a probability of non-exceedance (PONE) values, indicating the probability that an SIVI is not exceeded. For example, Table 3.2 provides the SIVI values under various PONE limits for the 4 sites of Figure 3.7. As seen from this table, at site-1, a P90 value of 10.2 denotes that the SIVI does not exceed 10.2 for 90% of the year. The PONE limits will be used in the remainder of the study to select an appropriate smoothing level for the smoothing batteries at various locations.

Table 3.2 SIVI values for various PONE levels for sites-1 to 4 of Table 3.1 in 2017

PONE	site-1	site-2	site-3	site-4
P50	4.8	2.0	8.4	8.2
P75	7.2	8.4	12.5	12.1
P90	11.1	10.2	15.3	15.4
P95	12.4	12.7	17.8	18.5
P99	22.1	21.3	22.5	23.4
P100	26.3	25.0	25.0	32.9

3.3.2 **Simulation Model and Optimisation**

The system topology considered in this study is an ac-coupled PV-diesel microgrid supplying ac loads, as shown in Figure 3.8. The smoothing battery's functionality in such systems is to smooth out the fluctuations in the output power of the PVs in order to limit the ramping requirements and stresses on the diesel generator(s). This is crucial for increasing the PV penetration in the microgrid without causing frequency instability and poor frequency regulation.

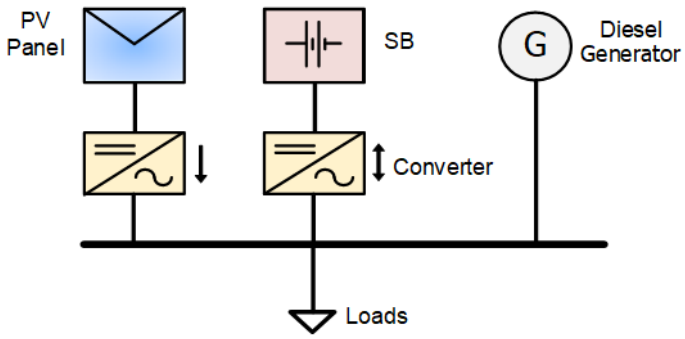

Figure 3.8. A typical PV-diesel microgrid with a power smoothing battery

For the purposes of this study, neither the diesel generator nor the loads are explicitly modelled as the study specifically looks at the smoothing battery's performance in producing a less volatile output from the solar PV system. It is assumed from the design of the microgrid that the diesel generator and PV system have been adequately sized to supply the load at all times without under- or over-loading the diesel generator. Based on the diesel generator specifications, the maximum ramp-rate capability of the generator defines the amount of smoothing required by the smoothing battery [107].

3.3.2.1 **Modelling of PV and Smoothing Battery Systems**

The output power of the PV system at the coupling point of the inverter at each time step of t ($P_{pv}(t)$) can be calculated by the simplified model of [111]

$$P_{pv}(t) = GHI(t) \times P_{nom} \times k_e \times k_m \times \left(1 - k_{pt} \times T_{amb}(t)\right) \times \eta_{inv} \qquad (3.38)$$

where k_e is the environmental derating factor to account for soiling, dust, etc. [%], k_m is the manufacturer tolerance derating factor [%], k_{pt} is the power-temperature coefficient [%/°C], $T_{amb}(t)$ is the ambient temperature at time step t [°C] and η_{inv} is the inverter's efficiency [%]. It is to be noted that this simplified model does not consider the effects of the PV array's tilt angle and azimuth nor the albedo (ground reflectance). The inverter is also assumed to be fully rated to the peak output power of the PV array and no oversupply coefficient is considered (i.e., dc:ac ratio is 1).

The Kinetic battery model developed in [112-114] is used in the simulation model to calculate the amount of energy that can be transferred to and from the smoothing battery at each time step. The model reflects the observation that a battery's capacity tends to decrease with an increasing rate of charge or discharge. The total charge in a battery is divided into an "available" charge (q_1 [Ah]), which is energy that is accessible for immediate use, and a "bound" charge (q_2 [Ah]), which is energy that is chemically bound, but can be released at a certain rate. The flows of available and bound charges can be described as

$$\begin{aligned} \frac{dq_1}{dt} &= -(I + k_1(1 - k_2)q_1 - k_1 k_2 q_2) \\ \frac{dq_2}{dt} &= k_1(1 - k_2)q_1 - k_1 k_2 q_2 \end{aligned} \qquad (3.39)$$

where I is the charge or discharge current [A], k_1 is a rate constant at which chemically bound charge becomes available and k_2 is the ratio of available charge

to total capacity. The differential equations can be solved for each time step t using Laplace transforms as

$$q_1 = q_{1,0}e^{-k_1\Delta t} + \frac{(q_0k_1k_2 - I)(1 - e^{-k_1\Delta t})}{k_1} - \frac{Ik_2(k_1\Delta t - 1 + e^{-k_1\Delta t})}{k_1}$$
$$q_2 = q_{2,0}e^{-k_1\Delta t} + q_0(1 - k_2)(1 - e^{-k_1\Delta t}) - \frac{I(1 - k_2)(k_1\Delta t - 1 + e^{-k_1\Delta t})}{k_1} \quad (3.40)$$

where $q_{1,0}$, $q_{2,0}$ and q_0 are the available, bound, and total charges at the beginning of the time step and Δt is the length of the time step (1 minute = 1/60 hour).

It is to be noted that k_1 and k_2 are specific to a battery's charging and/or discharging performance, which in turn varies with battery chemistry, capacity and construction. The constants can be estimated using a non-linear least squares algorithm that fits the battery constants with actual charge/discharge performance characteristics, e.g., from a battery manufacturer's datasheet. Also, the flow of charge into and out of the battery is also reduced by the conversion losses from the battery's bi-directional converter. Note that, the kinetic battery model does not consider the effects of temperature, self-discharge and cycle degradation/ageing on the capacity and SoC.

3.3.2.2 **Power Smoothing Algorithms**

Several methods are existing in the literature about power smoothing algorithms via batteries [60-61, 108-109], among which two commonly used techniques are considered here, as discussed below:

1. Moving average technique

The lagging moving average-based smoothing technique takes the arithmetic mean of the PV's output power for the previous N_w time steps from the current time step of t as [108-109]

$$P_{\mathrm{MA}}(t) = \frac{\sum_{i=0}^{N_{\mathrm{w}}-1} P_{\mathrm{PV}}(t-i)}{N_{\mathrm{w}}} \tag{3.41}$$

where $P_{MA}(t)$ is the smoothed PV power output at time step t [W], $P_{PV}(t)$ is the raw PV power output at that time step [W] and N_w is the window of the moving average, measured as the integer number of time steps.

2. Ramp rate control technique

The ramp rate-based smoothing technique limits the change in the output power between 1-minute time steps to a maximum value. In this study, the maximum allowable change in the output power is expressed as a proportion relative to the nominal output power of the PVs, in the form of

$$\Delta P_{max} = k_{RRL} \times P_{nom} \tag{3.42}$$

where ΔP_{max} is the maximum allowed change in the PV power output [W], k_{RRL} is the ramp rate limit [%] and P_{nom} is the nominal output of the PV module at standard test conditions [Wp]. The target output power by this technique ($P_{RR}(t)$) is then

$$P_{\mathrm{RR}}(t) = \begin{cases} P_{\mathrm{PV}}(t-1) - \Delta P_{\max} & \text{if} \quad |\Delta P_{\mathrm{PV}}| > \Delta P_{\max} \,\&\, \Delta P_{\mathrm{PV}} < 0 \\ P_{\mathrm{PV}}(t) & \text{if} \quad |\Delta P_{\mathrm{PV}}| \le \Delta P_{\max} \\ P_{\mathrm{PV}}(t-1) + \Delta P_{\max} & \text{if} \quad |\Delta P_{\mathrm{PV}}| > \Delta P_{\max} \,\&\, \Delta P_{\mathrm{PV}} > 0 \end{cases} \tag{3.43}$$

where $\Delta P_{PV} = P_{PV}(t) - P_{PV}(t-1)$ is the change in the output power of the PVs between time steps t and $t-1$.

At each time step, the smoothing battery's net output power ($P_{SB}^{MA}(t)$) is the difference between the smoothing battery's target output power and the PV's output power at that time step, i.e.,

$$P_{SB}^{MA}(t) = P_{MA}(t) - P_{PV}(t) \quad (3.44)$$

$$P_{SB}^{RR}(t) = P_{RR}(t) - P_{PV}(t) \quad (3.45)$$

for the moving average and ramp rate-based techniques, respectively. By convention, a positive power (i.e., $P_{SB}(t) > 0$) denotes that the smoothing battery is discharging, while a negative power denotes the smoothing battery's charging.

3.3.2.3 **Optimisation Problem and Solution**

The smoothing battery optimal capacity (SBOC) can be determined within an optimisation problem which determines the smoothing battery's best (least) maximum energy storage capacity (E_{SB}^{max}) as

$$SBOC = (E_{SB}^{max}) \quad (3.46)$$

which is subject to $SoC_{min} < SoC(t) \leq SoC_{max}$ while SoC_{min} and SoC_{max} respectively denote the smoothing battery's minimum and maximum allowed SoC.

It will be demonstrated in Chapter 6 that the results of the optimisation studies for both of the moving average and ramp rate-based smoothing techniques typically show several days in the year that can be marked as outliers in terms of the SBOC and/or the SIVI. Therefore, from an economic standpoint, there are diminishing investment returns from a smoothing battery that covers 100% of all cases (denoted by P100). As such, it is more prudent to select a smoothing level that covers the majority (e.g., 90 or 95%) of the cases (denoted respectively by P90 and P95) and allow curtailment of the PVs for the rest of the time. As such, the SBOC selection is based on the distribution of the optimisation results using a pre-selected (desired) smoothing level (e.g., P90 or P95).

To solve (3.46), two smoothing battery sizing methods can be considered. The first one is highly accurate but requires full chronological simulation and optimisation, while the second one provides an order-of-magnitude estimate that only requires the SIVI's calculation. They are discussed below:

3.3.2.4 **Detailed solution method**

The detailed method employs full chronological/time-sequential simulations and optimisation routines. The steps for this method are as follows:

a) Collecting 1-minute (or higher) resolution solar irradiance data for the site over at least one year,
b) Running the chronological simulation studies and optimisation for each day (discussed in more detail below)
c) Calculating the empirical CDFs and PONE levels for the dataset, and
d) Selecting a smoothing level based on the PONE of the optimisation results, and calculating the SBOC according to selected smoothing level.

The chronological simulation is executed for every simulation day at 1-minute time steps (i.e., 1,440 time steps per 24-hour of the simulation) to capture the variations in the demand and power output of the PV system. At each time step, the computation steps are as below:

a) Retrieving the solar irradiance for the time step from the available dataset,
b) Calculating the expected output power of the PVs from (3.38)
c) Employing the moving average or ramp rate-based battery smoothing technique and calculating the smoothing battery's charging/discharging status and level, from (3.44) or (3.45),

d) Calculating the smoothed output power of the PV, considering the smoothing battery's influence,
e) Updating the smoothing battery's SoC from the Kinetic battery model described in (3.39) and (3.40), and
f) Applying the smoothing battery's empty or full status (based on $\mathrm{SoC_{SB}(t)}$) to update its charging/discharging level, if required.

For each simulation day, the optimisation problem in (3.46) is solved using a binary search algorithm [110] where the smoothing battery's capacity is adjusted up and down at each iteration depending on whether the SoC constraints are met. The binary search algorithm ends when the difference between two successive iterations is below a nominated tolerance level or if the maximum number of iterations is reached.

3.3.2.5 **Proposed approximate solution method based on SIVI**

Although the detailed method is more accurate, it is computationally intensive and not necessarily amenable to practical scenarios, especially when conducting preliminary level project feasibility and screening studies. As such, an approximate method can be proposed that has an order-of-magnitude estimate but leads to very fast results. This technique is based on linear regression and using the combined optimisation results across all sites and the SIVI as the dependent variable. A statistical error term (i.e., the standard error) is also added to the regression to capture the upper envelope of the results. The steps for this method are can be summarised as:

a) Collecting 1-minute (or higher) resolution solar irradiance data for the site over at least one year,

b) Calculating SIVI for each day from the solar irradiance dataset,

c) Calculating the empirical CDFs and PONE levels for the SIVI dataset,

d) Selecting a smoothing level based on the PONE of SIVI, and

e) Calculating the approximate SBOC (denoted by $SBOC^{ap}$) based on the linear regression as

$$SBOC^{ap} = \alpha \times VI_{PONE} + \beta + \sigma \tag{3.47}$$

where VI_{PONE} is the $SIVI$ at the selected smoothing level (e.g., P90 or P95) while α and β are the linear regression coefficients and σ is the standard error of the estimate.

The coefficients of α and β are calculated by running a linear regression of the SBOC results for each day and across all sites while the standard error σ is calculated from

$$\sigma = \sqrt{\frac{\sum(E_{\mathrm{SB}}^{\max} - (E_{\mathrm{SB}}^{\max})^{\mathrm{pred}})^2}{N_{\mathrm{s}}}} \tag{3.48}$$

where E_{SB}^{max} is the SBOC for a single day while $(E_{SB}^{max})^{pred} = \alpha \times VI + \beta$ is the smoothing battery's capacity, predicted by the linear regression, and N_s is the total number of samples.

3.4 Framework for Integrating Solar PV into Weak Grids

3.4.1 Grid Connection Studies for PV Plants

The grid connection process is often initiated during the feasibility study stage of a PV plant development, where a grid connection application is lodged with the electricity network operator. As part of the application, the network operator requires a grid connection study to be performed. Depending on the

jurisdiction, the study is either performed by the network operator or it is deemed as contestable work that can be undertaken by third parties.

The overall grid connection study commonly consists of two subsidiary studies: 1) Grid impact study, which assesses the grid's capability to integrate the PV plant without adversely affecting the overall system, and 2) Grid code compliance study, which evaluates whether the PV plant and its equipment are technically compliant to the local rules and requirements (e.g., compatibility with tolerances of voltage and frequency variation, harmonics, flicker, etc.). Therefore, the grid impact study has a wider external focus towards the rest of the network whereas the grid code compliance study is more focused on the capabilities of the PV plant itself.

The grid connection study needs to be reviewed and approved by the network operator before the connection application can be accepted and a connection agreement is signed. An outcome of such a study is the identification of any network augmentations or non-network solutions (such as demand response) that are necessary to connect the PV plant, the costs of which may need to be borne by the network operator, the developer or are shared [115]. Alternatively, the conclusions of this type of study may set an upper limit on the maximum capacity of the PV plant that can be connected without additional network upgrades.

Grid codes and network operator study requirements are typically generic in nature and do not have special provisions for weak grids. It is usually left to the network operator's discretion to decide which studies are appropriate on a case by case basis. It is argued that a more systematic approach is needed when connecting

PV plants to weak grids, with specific issues investigated depending on the strength of the grid connection point.

3.4.2 **Weak and Strong Connection Points**

According to the IEEE Guide for planning dc links terminating at ac locations having low short-circuit capacities (IEEE Std-1204) [116], the strength of a distribution system can be characterised by the system's inertia and network's impedance (i.e., short-circuit capacity). These two factors dictate the sensitivity of the distribution system to fluctuations in frequency and voltage magnitude, respectively. Note that while inertia is a system-wide measure, the network impedance varies throughout the distribution system and is location-specific [117]. Thus, in the context of connecting a PV plant to a network, the concept of a weak connection point is one in which the network impedance at the connection point is high and/or the system inertia is low, both relative to the capacity of the PV plant to be connected. Weak connection points are most commonly found in sparsely populated rural or remote areas, islands with a fragile network, or countries with under-developed electricity infrastructure [77]. It should be noted that the strength of a connection point is a relative quantity, and so a single power distribution system may have both weak and strong connection points depending on the capacity and location of the proposed PV plant. In the proposed framework, PV plant connection points are classified into three categories: 1) weak high-impedance, 2) weak low-inertia, and 3) strong connection points.

3.4.2.1 **Weak High-Impedance Connection Points**

The impedance of a connection point is commonly measured by the short-circuit ratio (SCR) and is defined by the IEEE Standard Std-1204 [116] as

$$SCR = \frac{S_{SC}}{P_n} \tag{3.49}$$

where S_{SC} is the fault level at the connection bus (in MVA) and P_n is the nominal power of the PV plant connected to the same bus (in MWp). The fault level at the connection bus is usually determined by the help of power system software-based short-circuit simulations according to IEC or ANSI standards, and is normally provided by the network operator. As per the IEEE Std-1204, a weak connection point has an SCR ≤ 3.

3.4.2.2 **Weak Low-inertia Connection Points**

Similar to the SCR, a stiffness ratio (SR) is proposed to measure the inertia of a connection point relative to the PV plant and is defined as

$$SR = \frac{\beta}{P_n} \tag{3.50}$$

where P_n is the nominal power of the PV plant connected to the system (in MWp) while β is the power system stiffness or composite frequency response characteristic (in MW/Hz) and includes the influence of the combined inertia of all directly-coupled rotating machines in the system, as well as the automatic control actions of primary frequency controllers in response to frequency deviations (e.g., speed-droop governors).

The stiffness of a network can be estimated through practical observations and/or recordings from past events or via power system software-based dynamic simulations in which the network's frequency deviation is measured following a loss of generation event of fixed capacity. A connection point can be considered weak when SR ≤ 5, based on an implied frequency deviation of 0.2 Hz after a sudden trip of the PV plant. This maximum frequency deviation is selected

because it represents the lower limit of the normal operating frequency range for many power systems around the world (i.e., 49.8 – 50.2 or 59.8 – 60.2 Hz for systems with a nominal frequency of 50 and 60 Hz respectively). Outside of these bands, the power system is said to be in a frequency excursion state, and primary frequency control action is expected to take place. Hence, the threshold of SR ≤ 5 can prevent the network's frequency to fall outside the normal operating range following the trip of the PV plant [118].

3.4.2.3 **Strong Connection Points**

At strong connection points, the PV plant does not exert significant influence on the voltage and frequency of the system and is expected only to have minimal impacts on the grid. A connection point can be considered strong when SCR > 3 and SR > 5, and very strong if SCR > 25 and SR > 30. In practical terms, a very strong connection point is equivalent to connecting a small PV plant (e.g., 1 MWp) to a key substation in a very large system (e.g., one with a peak demand of 20,000 MW), where the impact of the PV plant on the grid is negligible. However, it should be noted that the grid may already be constrained in other ways, such as high fault levels and/or highly loaded lines, and the addition of a PV plant may exacerbate these pre-existing issues.

3.4.3 **Proposed Assessment Framework**

As weak grids are highly sensitive to voltage and/or frequency fluctuations, the grid connection studies of PV plants to such networks should be tailored specifically to investigate the critical issues applicable to the connection point. To address this, a framework is proposed that classifies grid connection points and suggests the appropriate analyses to be performed depending on whether the

connection points are weak high-impedance, weak low-inertia or strong. The proposed process flowchart is shown in Figure 3.9.

As seen from this flowchart, various types of analyses are required depending on the type of the weak connection point while some analyses are common between the weak and strong points. The flowchart also shows the actions that need to be taken by the network operator in the event that the initial proposal fails to fulfil the requirements and criteria. The suggested studies and acceptance criteria are summarised in Table 3.3 while the following subsections provide detailed descriptions of the issues and special considerations that are associated with each part of the proposed assessment framework.

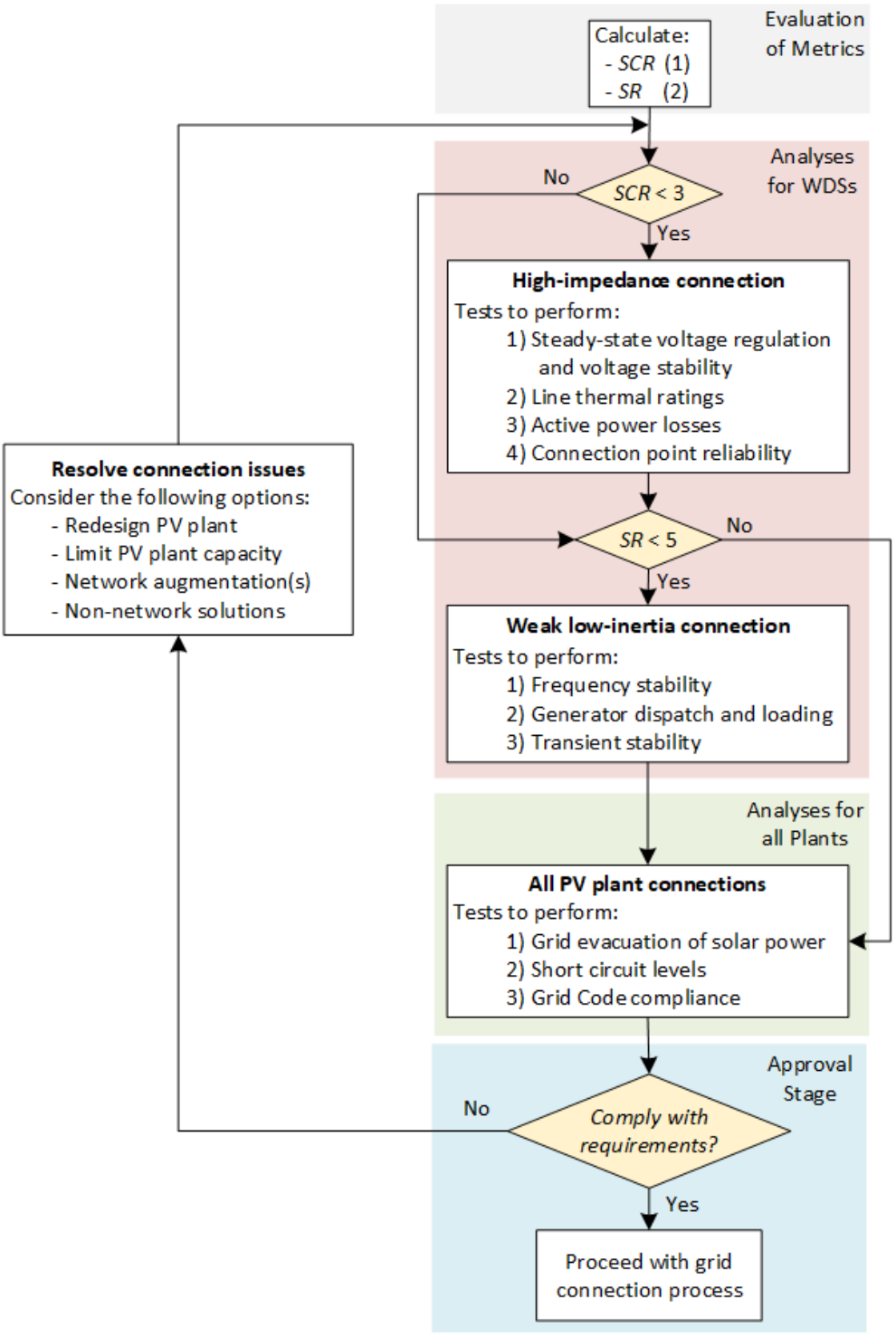

Figure 3.9. Proposed framework for assessing grid connections to weak grids

Table 3.3 Summary of the essential considerations for integrating PV plants into weak grids

Connection	Factor	Consideration/Criteria	Case Studies
Weak high impedance	Voltage regulation and stability	• Steady-state voltage regulation maintained at connection point and nearby buses • Dynamic voltage stability is maintained after a contingency	• Daytime operation with varying PV plant output • Night time voltage regulation • Dynamic voltage response after loss of PV plant/load
	Line thermal ratings	• Thermal ratings of upstream overhead lines/cables are not overloaded with the PV plant connected	• N-1 contingency analyses at peak daytime loading and maximum PV output
	Active power losses	• Active power losses with the PV plant connected are below grid code requirements	• Losses in system at minimum or low daytime load and high PV plant output
Weak low inertia	Frequency stability	• Normal day-to-day fluctuations in PV plant output do not trigger the UFLS system • Abnormal contingencies such as loss of generating plant events do not cause grid instability/collapse	• Extreme ramp event • Loss of PV plant • Loss of largest generator
	Generator dispatch and loading	• Changes to existing generator dispatch arrangements due to the PV plant must not violate contractual obligations, minimum loading and spinning reserve requirements.	• Daytime minimum load • PV plant maximum output • Optimal generator dispatch

Connection	Factor	Consideration/Criteria	Case Studies
All	Transient stability	• Protection relay tripping times are below CFCTs	• Recalculate CFCTs for faults on all major lines
	Grid evacuation	• Power generated from PV plant can be evacuated to the grid • Line thermal ratings and transformer ratings are not exceeded during system normal and N-1 contingency cases	• System normal at peak daytime loading and maximum PV output • N-1 contingency analyses at peak daytime loading and maximum PV output
	Short-circuit levels	• Short-circuit levels do not exceed equipment fault ratings	• System normal at peak daytime loading
	Grid code compliance	• Performance of the PV plant at the connection point complies with the applicable Grid Code	• Studies as per Grid Code requirements, e.g., PQ capability, fault ride-through, power quality, etc.

3.4.4 **Assessment of Weak High-impedance Connection Points**

At weak high-impedance connection points, the PV plant can exert a large influence on the network voltages in the vicinity of the plant. Such connection points are typically characterised by interconnections at (or near) the end of long radial feeders with no embedded generation and limited reactive power support [85]. There are four key issues that need to be assessed at weak high-impedance connection points. They are voltage regulation and stability, line thermal ratings, excessive losses, and connection point reliability, as discussed in the following subsections.

3.4.4.1 **Steady-State Voltage Regulation and Voltage Stability**

Weak high-impedance connection points exhibit higher sensitivity to voltage fluctuations and are more prone to issues with voltage stability and control. Voltage sensitivity is measured by the gradient of the reactive power-voltage magnitude (Q-V) curve (denoted by $\partial V/\partial Q$) at the connection point, and represents the sensitivity of the voltage to changes in reactive power injection/absorption. Weak connection points typically have a high $\partial V/\partial Q$ which implies that a small change in reactive power will lead to large changes in the voltage magnitude. In distribution networks with low X/R ratios, there is also a higher level of coupling between active power and voltage magnitude. Thus, active power swings can also affect voltage magnitudes at weak connection points. This is of high importance to PV plants with their intrinsic variability in output power due to the continuously changing ambient conditions (e.g., see case study-3 in Section-5).

The simplest and most efficient way to mitigate voltage regulation issues at weak connection points is to operate the inverters of the PV plant in voltage control mode, rather than at fixed power factor mode. Most commercially available inverters can operate within a reactive power range of up to 0.95 leading/lagging, which is suitable in most cases to regulate voltages within a tight band. Figure 3.10 illustrates the desired operation principle for such inverters, and as it is seen from this figure, their output reactive power varies with respect to the variations of the voltage magnitude.

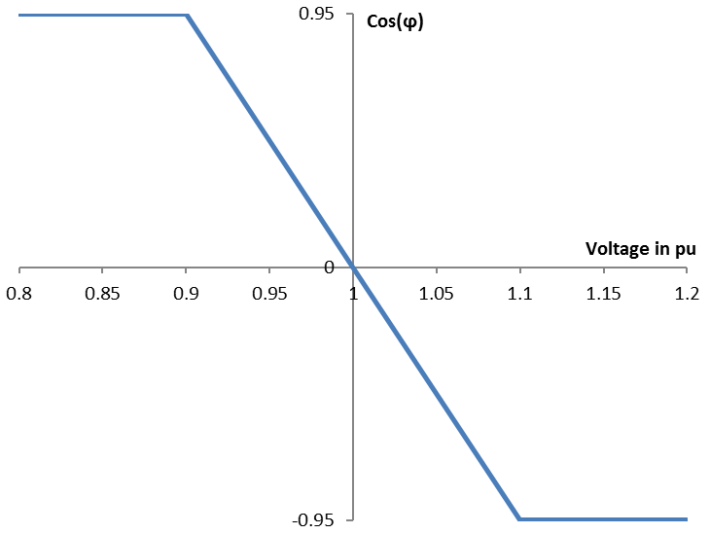

Figure 3.10. Typical Q injection/absorption curve to realise voltage support by voltage control of PV plant inverters.

Operating the PV inverters in voltage control or reactive power support mode can be particularly useful for supporting distribution systems that are already stressed and have poorly regulated voltage profiles, especially during evening peak periods or to aid voltage recovery during sag or post-fault conditions [119]. Since many PV inverters can generate reactive power at zero active power output, a PV plant can also improve the voltage profile of the nearby buses throughout the entire day and night (e.g., refer to case study-2 in Chapter 7) [120].

It should be noted that the ratings of the transformers and cables within the PV plant, as well as the interconnection lines, should always be taken into consideration when formulating reactive power requirements for PV plants, especially for large plants and/or those with long interconnection lines where the power factor will be influenced by the electrical infrastructure. Additional reactive power support by fixed/switched capacitor banks, dynamic voltage regulators, etc. may also be required if the reactive power capability of the PV plant is inadequate or if the plant is deliberately optimised for delivering the maximum output active

power. Alternatively, a back-to-back dc link between the PV plant and the connection point can be considered, as suggested in [121]; although detailed techno-economic analyses need to be conducted to validate the economic merits of such a solution.

When connecting a PV plant to the end of a radial feeder, there is a tendency for the voltage at the midpoint of the feeder to sag. A voltage-distance plot can be used to visualise the voltage profile along the feeder in order to verify that the voltage magnitude stays within the acceptable limits set by the network operator throughout the feeder and not only the connection point of the PV plant (e.g., see case study-1 in Chapter 7).

At weak connection points, the network operator may also be concerned with the dynamic voltage response of the system after a fast ramp or complete trip of the PV plant, or after the loss of load events. As the plant may be supporting the voltage during normal operation with both active and reactive power injections, rapid changes in the output power of the PV plant or its nearby loads may lead to excessive voltage sags/swells at the connection point and surrounding buses. Mitigating such a contingency may require fast-acting reactive power support such as static VAR compensators, as was recommended for the Nyngan PV plant in Australia [122].

Standard steady-state voltage stability analyses (e.g., the active power-voltage magnitude and reactive power-voltage magnitude curves) can determine the current system operating point and network loadability limits. PV plants with reactive power/voltage control can generally be expected to improve voltage stability limits at weak high-impedance connection points (e.g., refer to case study-1 in Chapter 7). In addition, it is also reported in [85] and [123] that small signal

stability may be an issue at very low SCR values (i.e., SCR ≤ 1.5), thereby indicating that such an analysis is also crucial.

3.4.4.2 **Line Thermal Ratings**

A weak connection point indicates high upstream source impedance relative to the PV plant. This can be the result of a radial feeder from the main grid to the connection point (e.g., a long line drawn to a remote area). Therefore, the penetration level of the PV plant at such connection points may be limited by the thermal/current rating of the weakest upstream distribution feeder. Load flow and N-1 contingency analyses (if applicable) should be performed at the worst line thermal ratings (e.g., summer day ratings) to ensure that the power flowing from the PV plant back to the grid does not overload the weakest upstream line. When calculating buried cable current ratings, the cyclic nature of PV generation should also be taken into account.

3.4.4.3 **Active Power Losses**

Considerations need to be made regarding system losses for the PV plants connected to radial distribution feeders or downstream substations. Power losses due to the PV plant can be significant for long, lightly-loaded radial feeders. From the utility standpoint, a substantial increase in power losses due to a PV plant connection may not be acceptable since technical losses are often monitored and tracked as a key performance indicator for the distribution utility. Thus any increase in losses is always discouraged. There are also implications for the PV plant developer, as depending on the custody metering location, the cost of energy losses may need to be borne by the PV plant.

Mitigating the power loss problem may require building a dedicated line with a higher nominal voltage (e.g., a transmission line) and a reduced current as losses are inversely proportional to the square of the current. In addition, a direct connection to substations with higher daytime loading will also mitigate losses as the power generated by the PV plant will have a more direct path to the loads as opposed to flowing upstream through the distribution network first before being reticulated to loaded feeders.

3.4.4.4 **Connection Point Reliability**

Reliability may be a concern for tee connections into a radial distribution feeder. This is particularly a problem for radial feeders without redundancy as the feeder can be prone to faults or be part of an under-frequency load shedding (UFLS) scheme and can trip during under-frequency events. In both cases, a feeder trip will cause an unplanned outage of the PV plant. A UFLS trip would actually exacerbate an under-frequency problem since the output active power of the PV plant is suddenly removed from the system. The reliability of a radial feeder needs to be assessed by investigating the history of faults/trips on the feeder and checking the UFLS scheme and its set-points.

The risk of spurious or frequent faults on the feeder can be mitigated by installing autoreclosers at the tee connection, although the system must still be able to withstand a PV plant trip while maintaining stability. An autorecloser does not prevent a feeder trip but facilitates rapid reconnection of the grid following a trip in order to minimise the PV plant's downtime. Alternatively, a dedicated transmission line can be built to the nearest substation which is typically more reliable because it is a direct connection without spurs or customers, and its

maintenance is easier versus shared distribution feeders; however, it can increase the project's overall costs significantly.

3.4.5 Assessment of Weak Low-inertia Connection Points

Weak low-inertia connection points are susceptible to larger frequency swings as a result of normal PV plant operation and/or network contingency events. The instantaneous mismatches in the active power generated in a distribution system and its demand are balanced through the rotational kinetic energy of the synchronous machines in the system. The linkages between rotational kinetic energy, inertia and speed/frequency are expressed by the swing equation of [124]

$$\frac{d\omega}{dt} = \frac{1}{2H}(T_{\mathrm{m}} - T_{\mathrm{e}}) \tag{3.51}$$

where ω is the angular frequency (in pu) and H is the inertia constant (in seconds) while T_{m} and T_{e} are respectively the mechanical (driving) and electrical (load) torques (in pu). From (3.51), it can be seen that high-inertia systems have a reduced rate of change of frequency. This is illustrated in Figure 3.11 which depicts the expected responses of a diesel generator with different inertia constants for a 25% load step increase. From the figure, it can be seen that a higher inertia leads to a lower frequency deviation and rate of change of frequency.

Standalone power distribution systems in remote and rural areas or islands normally have low rotational inertia and are primarily supplied by diesel engine generators. They also tend to be small in total generation capacity and are therefore classified as weak low-inertia connection points for PV plants. Frequency stability along with generator dispatch and loading, as well as transient stability are three key issues that need to be assessed in such systems. As these issues are system-

wide global phenomena, the use of an equivalent network representation at (or near) the connection point of the PV plant is not valid for the assessment of weak low-inertia systems. For such systems, it is essential that the complete power system is modelled including all the generators and loads in the system rather than a limited section of the system to which the PV plant is to be connected.

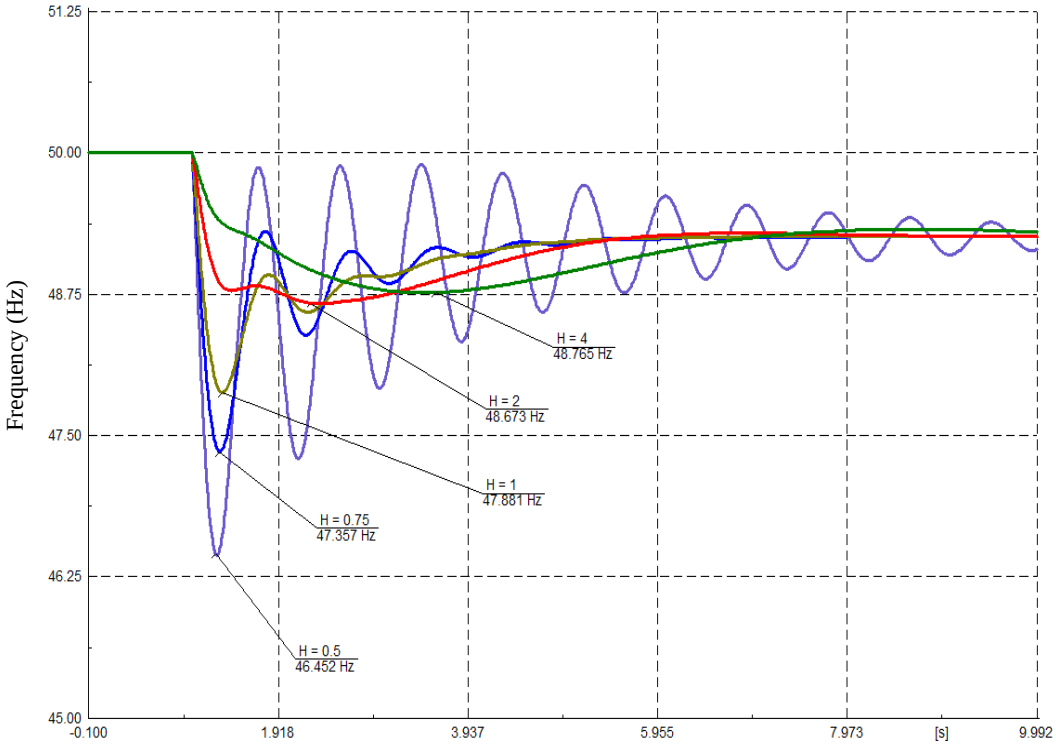

Figure 3.11. Various frequency drops and its rate of changes for a distribution system following a 25% demand increase, showing different performances when the system accommodates a diesel generator with various inertia constants

3.4.5.1 **Frequency Stability**

Replacing synchronous machine(s) of a weak grids by inertia-less PV plants or reducing their quantity will lead to a further reduction in the system's overall inertia, and consequently will adversely impact the frequency stability of the system, which is the system's ability to maintain its steady frequency following a disturbance, with the minimal unintentional loss of load [125]. When integrating a PV plant in a low-inertia system, the system is assumed stable if:

- the frequency-based protective relays do not trip the system during normal day-to-day variations in demand and output power of the PV plant (including short-term fluctuations and extreme ramping events), and
- the frequency does not collapse and reaches an operating equilibrium point following an abnormal system disturbance or network fault (i.e., leading to a loss of generator or PV plant). In this case, UFLS may be tolerated.

To validate the above two conditions for a weak grid to which a PV plant is being connected, the below criteria are suggested to be considered carefully:

- **Frequency-based protection:** All frequency-based protective schemes such as the UFLS, over-frequency, the rate of change of frequency, and the volts/Hz schemes.
- **Primary frequency control:** It is crucial to find the generator(s) responsible for the primary frequency control in the weak grids. The dynamic models of the governors of such generators need to be considered in the studies. Commercial arrangements may also need to be considered, i.e., certain generators may operate at fixed output power and may not be obliged to respond to system disturbances based on their commercial arrangements such as power purchase agreement.
- **Spinning reserve margin:** The studies should define the minimum spinning reserve required to maintain the frequency stability of the weak grids while considering commercial arrangements to determine the generator dispatch/merit order and requirements.

To analyse the above criteria, the following studies should be considered:

- **An extreme ramp event:** The rapid ramp up/down of the output power of the considered PV plant is highly probable by a large and fast-moving cloud crossing over (see Figure 3.12 captured for a PV plant in Java, Indonesia for 4 sample days). Previous studies indicate that the ramp rates of PV plants can reach extremes of up to 50% reduction in their output over one minute [126]. Empirical observations by the authors from operational plants in the Philippines, Indonesia and India support this assertion occurring during the monsoon season when there are sudden rain showers. Measurements from operational plants of 5–10 MWp show that they are affected less due to their larger area coverage. In such conditions, the resulting active power deficit in the system is typically picked up by synchronous generators with primary frequency control, but there is a corresponding frequency reduction in the process. This frequency drop should not be large enough to activate the UFLS protective relays which can trip a portion of the load. A study has to be carried out to explore the operation of the existing primary frequency control techniques after an extreme ramp event, as well as the possibility of UFLS activation.
- **Loss of the PV plant:** The weak grid should maintain stability during the transient period immediately after a sudden unplanned outage/loss of PV plant because of a fault condition. It should also reach its steady-state equilibrium point without sustained oscillations. A study has to be performed to examine the ability of the system to remain stable after the trip of the PV plant. Secondary assessment criteria pertain to the triggering of the UFLS system. In the ideal scenario, the disconnection of the PV plant does not

activate any UFLS protective relays; however, although load-shedding may be acceptable, a risk assessment is needed to evaluate the reliability of the PV plant's interconnection and the risk of frequent trips.

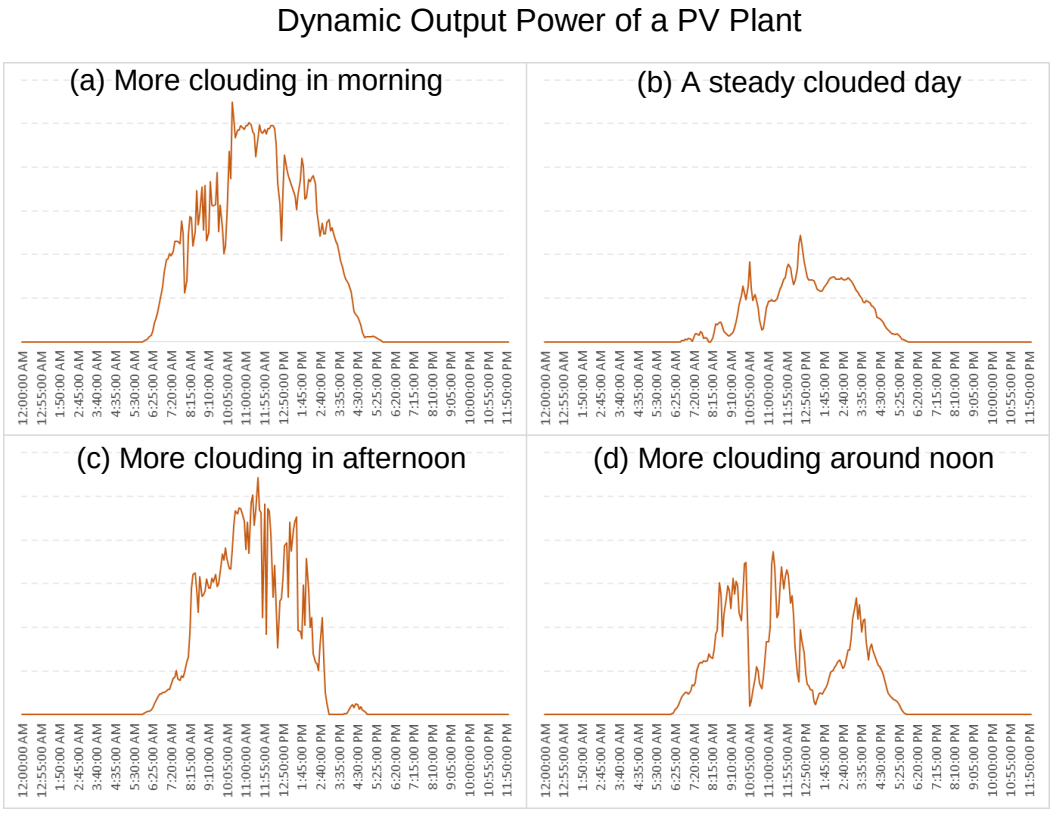

Figure 3.12. Measured output power profile for an operating PV plant in Java, Indonesia in 4 sample days, showing different and significant power ramp up/down due to moving clouds.

- **Loss of the largest synchronous generator**: Similar to the loss of the PV plant, the system should remain stable following the sudden loss of the largest synchronous generator. A study has to be conducted to examine the system's frequency stability following the loss of the PV plant and/or the largest synchronous generator as this can be the limiting factor for increasing the penetration of PV plants in low-inertia systems.

3.4.5.2 **Generator Dispatch and Loading**

Another factor which can limit the penetration level of PV plants at low-inertia connection points is the daytime minimum loading and the level of power that will be produced by the PV plant instead of the existing synchronous generators. This is of particular importance in systems without market-oriented generator dispatch mechanisms and with a mix of generator ownership from the utility, independent power producer, and rental schemes. In such cases, commercial/contractual arrangements may dictate which generators can be displaced by the PV plant. If the daytime minimum load is light, then there may not be much room for the power injected by the PV plant. On the other hand, synchronous generators normally have requirements for minimum continuous output power to maintain high fuel efficiency and/or prevent long-term damage (e.g., the loading of a diesel generator should be over 40% of its rated capacity to prevent long-term damage and over 70% to have a high fuel efficiency [127]). Finally, some network operators have a requirement for minimum spinning reserve (also called primary operating reserve), which is calculated based on system conditions and varies with time. This level is defined using different techniques by system operators around the world [128]). Furthermore, some operators also maintain active constraints on the penetration of non-synchronous generation [129].

Considering the above factors, the maximum size of the PV plant will be constrained by a combination of minimum loading of existing synchronous generators, contractual obligations, spinning reserve requirements and daytime minimum loads. It is also recommended to perform optimal power flow studies using electricity production cost, loss minimisation, or their combinations as the

objective function while taking into account all of the abovementioned dispatch constraints.

3.4.5.3 **Transient Stability**

The reduction in the system's total inertia after replacing the existing synchronous generators by PV plants may adversely affect the transient stability of the system, in particular, its critical fault clearing time (CFCT) [130]. For low-inertia systems, the CFCT needs to be recalculated and compared against the settings of the existing protective relays to ensure that clearing times are still below the revised CFCT.

3.4.6 **Common Studies for All Connection Points**

The following common studies are recommended for all connection points, irrespective of whether they are weak or strong:

- Grid evacuation of solar power: The power generated by the PV plant can be evacuated to the grid without overloading any branch elements (lines, transformers, etc.) in normal and N-1 contingency studies.
- Short-circuit levels: All fault levels in the system remain within equipment fault ratings when the system accommodates the PV plant at full capacity.
- Grid Code compliance: The performance of the PV plant at the connection point complies with the applicable Grid Codes (e.g., operating ranges, reactive power limits, fault ride-through, power quality, etc.)

3.4.7 **Recommended Data Requirements**

Practical experience has shown that operators of weak grids often do not have a comprehensive modeling data of their systems due to either the lack of

resources or the relative simplicity of their networks. Modeling data for standard equipment such as synchronous machines (e.g., transient and sub-transient reactances, time constants, inertia, etc.), power transformers (e.g., impedances, copper losses, etc.) and overhead lines (e.g., impedances, geometry, lengths, etc.) are often not documented in a systematic manner. Although the data is available, it is usually dispersed across the operations and planning staff, thus requiring close liaison with relevant personnel. Furthermore, some of the information might be outdated and/or inaccurate and should be cross-checked and validated.

Ideally, the network model has power flow solved cases that are tuned to recent operational data, which can be taken from the supervisory control and data acquisition (SCADA) systems for one or more representative days or averaged over a period of time (e.g., 1 year). To tune a base case network model, one typically requires:

- The daily load profile of the feeders,
- Power flow and power factor data measured at each feeder,
- Voltage profiles at main buses (at 30 or 60-min intervals),
- Daily generator dispatch profile or dispatch merit order and their commercial conditions (e.g., minimum dispatch requirements and/or limits),
- Set-points of generators' voltage control and transformers' automatic tap changers, and
- Status of tie-open points, capacitor banks, and shunt reactors

Dynamic modeling for the network requires additional data such as those of prime mover/governor, and excitation controller structures and settings. Complete control block diagrams and parameters are rarely available, and thus, they are

normally estimated from the vendors' datasheet. The dynamic models can potentially be tuned if waveform records from system disturbances are available.

Generators' inertia constants are not available often while they are critical for predicting the frequency deviations in low-inertia systems such as weak grids. As an example, let us consider Figure 3.11 which illustrates the load acceptance results of a 1.5 MVA diesel generator with varying inertia constants for a 25% demand increase. This figure shows a wide range of frequency deviation of 1.235 – 3.575 Hz (i.e., 2.47 – 7.15% of the nominal frequency) for inertia constants (H) of 0.5 – 4 seconds. From this figure, it can be seen that selection of appropriate inertia constants is crucial, particularly for frequency stability studies that investigate the triggering point of UFLS protective relays. Even though inertia constants are typically provided as normalised quantities, there can be a considerable variation in their values depending on generator type and nominal rating (i.e., smaller machines generally have lower inertia constants).

Table 3.4 Typical inertia constants for synchronous machines [153]

Generator Type	No. of Samples	Capacity [MVA]			Inertia Constant (H) [s]		
		min	max	median	min	max	median
Coal	45	28.6	904	389	2.08	5.70	3.172
Gas	47	22.5	588	99.5	1.92	8.90	4.996
Hydro	22	13.3	312.5	46.8	2.40	6.80	3.679
Diesel	26	0.3125	2.5	1.25	0.60	1.72	0.945

Table 3.4 shows the inertia constants for a range of generator types and sizes, based on a data set of power plants from the Australian national electricity market operator and manufacturer datasheets. In lieu of inertia constants, network

operators may provide observed quantities from system events such as the maximum frequency deviation seen after a generator trip (i.e., leading to the composite frequency response characteristic β in MW/Hz). These observations can be used to tune the dynamic models and ensure that the selected inertia constants and primary frequency controller parameters produce a similar response.

3.5 Estimating Load Relief for Frequency Stability Studies in Weak Grids

One of the key parameters for frequency stability studies using single-mass models is the load relief factor (LRF), which approximates the frequency dependencies of loads in a system at an aggregate level. As weak low-inertia grids are more sensitive to frequency deviations, the LRF becomes a crucial parameter for determining whether a weak grid remains stable after large contingencies.

3.5.1 Load Relief Factor Estimation

The standard practice for modelling loads with frequency dependencies is to multiply the load's nominal power consumption by a frequency-dependent LRF, as given by [131]

$$P_{\text{load}}(f) = P_{\text{load}}^{\text{nom}} \left(1 + \frac{k_p \times \Delta f}{f^{\text{nom}}}\right) \tag{3.52}$$

where $P_{\text{load}}(f)$ is the system load at frequency f (in MW), $P_{\text{load}}^{\text{nom}}$ is the system load at nominal frequency $f^{\text{nom}} = 50$ Hz, k_p is the frequency-dependent LRF (in MW/Hz), and $\Delta f = f - f^{\text{nom}}$ is the frequency deviation from nominal frequency (in Hz).

Given a series of measured values for $P(f)$ and f, the LRF k_p can be readily estimated by a linear regression with zero y-intercept (i.e., using an ordinary linear least squares solver).

This kind of analysis is straightforward for LRFs at specific buses in the system where the active power response can be directly measured. For bus level LRF estimation, voltage dependency terms are also normally added [132]:

$$P_{load}(f) = P_{\text{load}}^{\text{nom}} \left(\frac{V(f)}{V_0}\right)^{n_v} \left(1 + \frac{k_p \times \Delta f}{f^{\text{nom}}}\right) \tag{3.53}$$

where $V(f)$ is the measured bus voltage at frequency f (V), V_0 is the pre-contingent bus voltage (V) and n_v is the voltage dependency of the load. With a few simplifying assumptions, a log-linear regression analysis can be performed on (8.1) to estimate both k_p and n_v based on a set of 3-tuples (frequency, load, voltage).

However, it was shown in [132] that bus-level LRFs vary considerably across both space and time. Thus, were it even possible to obtain active power measurements at all load buses of the system and then calculate bus-level LRFs, it is unclear how these LRFs could be suitably aggregated to yield a system level LRF (this will be further demonstrated with a case study in Chapter 8). Thus, in order to estimate system-level LRFs, it is more desirable to estimate the overall system load response (particularly using measurement data currently at the disposal of the grid operator).

3.5.2 **System Load Response Estimation**

Except for very small systems, the total system load is typically not directly measured. Instead, the active power outputs of major generating units are often measured at high resolutions by fault recorders that trigger during contingency

events. Hence, the system load response can be inferred from a simplified formulation of the swing equation

$$\frac{df}{dt} = \frac{f^{\text{nom}} \times \Delta P}{2 \times KE_{sys}} \tag{3.54}$$

in which $\frac{df}{dt}$ is the rate of change of frequency (RoCoF) (in Hz/s), KE_{sys} is the post-contingent system inertia (in MWs) and ΔP is the active power imbalance in the system (in MW).

In the seconds after a generator or load contingency, the active power imbalance can be estimated as

$$\Delta P(t) = \Delta PFR(t) + \Delta P_{\text{cont}}(t) - \Delta P_{\text{load}}(t) \tag{3.55}$$

where $\Delta PFR(t)$ is the aggregate system primary frequency response (PFR), $\Delta P_{\text{cont}}(t)$ is the change in the active power of the tripped unit relative to its pre-event power output and $\Delta P_{\text{load}}(t)$ is the change in the system's load, all at time t.

The system load response is estimated using a discretised formulation of

$$\Delta P_{load}(t) = \Delta PFR(t) + \Delta P_{\text{cont}}(t) - \left(\frac{2\,KE_{sys}}{f_n}\right)\left(\frac{\Delta f}{\Delta t}\right) \tag{3.56}$$

in which $\Delta f = f(t + \Delta t) - f(t)$ is the change in frequency between two measurement intervals and Δt is the measurement resolution of the high-speed recorders (in second).

To filter out high-frequency noise from the system frequency measurements, the raw measured RoCoF is smoothed via a moving average filter with a window of 10 cycles (i.e., 200 ms). This is considered to be acceptable, particularly for larger grids, as the time constants for the system contingency response is in the order of seconds (i.e., high frequency transients are typically not expected from a generator or load contingency event) [135].

3.5.3 **System Level Load Relief Factor Estimation**

Based on the preceding sections, the following procedure is used to estimate system level LRFs:

a) Estimate the RoCoF using the high-speed frequency trace and taking the maximum of a sample-by-sample time derivative of the frequency measurements ($\Delta f/\Delta t$) smoothed with a 500ms sliding window
b) Estimate the total system inertia (including load inertia) using the RoCoF estimate from step (a) [KE_{sys}]
c) Collate the high-speed active power response traces from all major generators and system interruptible loads and combine them together to form a system-level primary frequency response (PFR) trace [$\Delta PFR(t)$]
d) Extract the high-speed active power response trace for the tripped unit [ΔP_{cont}]
e) Estimate the system load trace using (3.56)
f) Estimate the system load relief factor via linear regression of (3.52) using the estimated system load values in step (e)

3.6 **Summary**

This chapter has introduced five distinct concepts and techniques for analysing and/or improving stability in microgrids and weak grids, namely 1) a load flow-based initialisation method for the microgrid small-signal stability model, 2) a method for interconnecting two neighbouring microgrids via a back-to-back dc link to provide frequency stability support, 3) an optimal battery sizing method for smoothing out PV fluctuations in PV-diesel microgrids, 4) a structured framework for analysing PV integration into weak grids, and 5) a technique for

estimating system level load relief factors using high-speed fault recorder data. Each of the proposed concepts and techniques are validated with a set of sample case studies as demonstrated in Chapters 4 to 8.

Chapter 4 Small-Signal Stability in Converter Dominated Microgrids

In this chapter, the small-signal model and initialisation method proposed in Section 3.1 is validated with time-domain simulations. The initialisation method is then used to perform sensitivity analyses on the small-signal stability of microgrids with varying network parameters and topological characteristics.

4.1 Model Validation

The small-signal model and load flow initialisation method described in Section 3.1 is validated by numerical (time-domain) simulation of the large-signal model equations. If the small signal model is correctly formulated, then the limits of stability predicted by the small signal model should be well aligned with the time-domain simulations.

The differential algebraic equations (DAE) in the large signal model are solved numerically using a partitioned solution approach and the naive Euler method as the explicit numerical integrator, i.e., for a first-order ODE of the form $y'(t) = f(t, y(t))$ and the initial conditions $y_0 = y(t_0)$, then:

$$y_{n+1} = y_n + h \times f\big(t, y(t)\big) \tag{4.1}$$

where h is the integration step size.

4.1.1 **Test Network**

The small-signal model is used to analyse a 380V, 50Hz three-phase microgrid comprising three buses, three converters, two lines and two loads, as shown schematically in Figure 4.1.

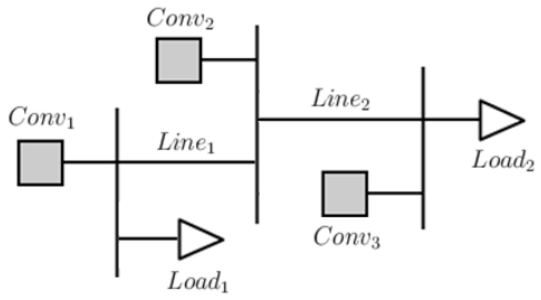

Figure 4.1. Microgrid test case for model validation

The microgrid loading is $P_{load1} = 5.76$ kW and $P_{load2} = 7.22$kW. Line impedances are $Z_{line1} = 0.23 + j0.2\Omega$ and $Z_{line1} = 0.35 + j0.58\Omega$. A virtual resistor of $R_V = 10^3\Omega$ is used. The converters are identical, share the load equally and each has parameters $\omega_c = 31.41$ rad/s, $L_f = 1.35$ mH, $C = 50\ \mu$F, $R_f = 0.1\ \Omega$, $\$L_c =$ 0.35mH and $R_c = 0.3\ \Omega$.

4.1.2 **Simulation Results**

The eigenvalues of the state-space matrix are calculated for a set of active power droop gains m between 10^{-4} and 30×10^{-4}. The plot in Figure 4.2a shows the trajectory of the critical eigenvalues for the range of active power droop gains. The microgrid is critically stable at $m \approx 2 \times 10^{-3}$.

In order to verify the accuracy of the small-signal stability model and load flow initialisation method, time-domain simulations of the test microgrid are performed for three load step cases in the vicinity of the critically stable operating point. If the results of the small-signal stability model are accurate, then one would expect that the time-domain simulations exhibit stable, critically stable and unstable responses to small

disturbances such as a minor load step. Indeed, this is what is observed from the simulation results (refer to Figure 4.2b-d), which confirm the critical operating points defined by the developed small-signal stability analysis.

(a)

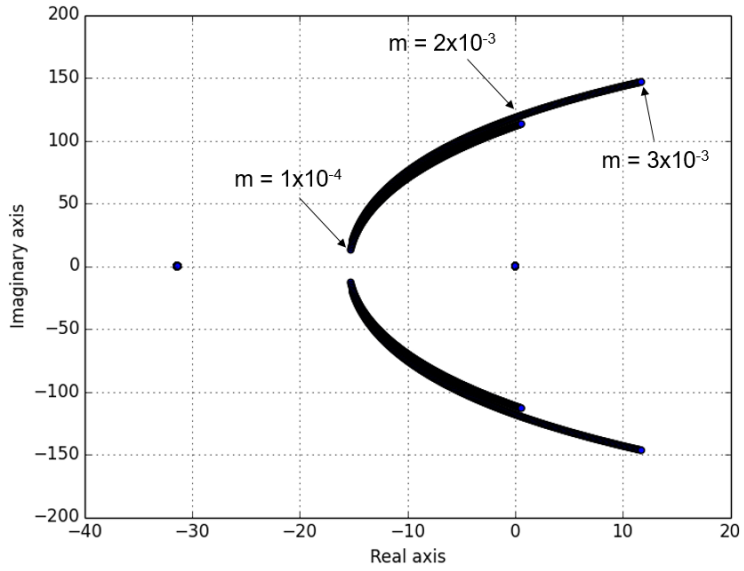

(b)

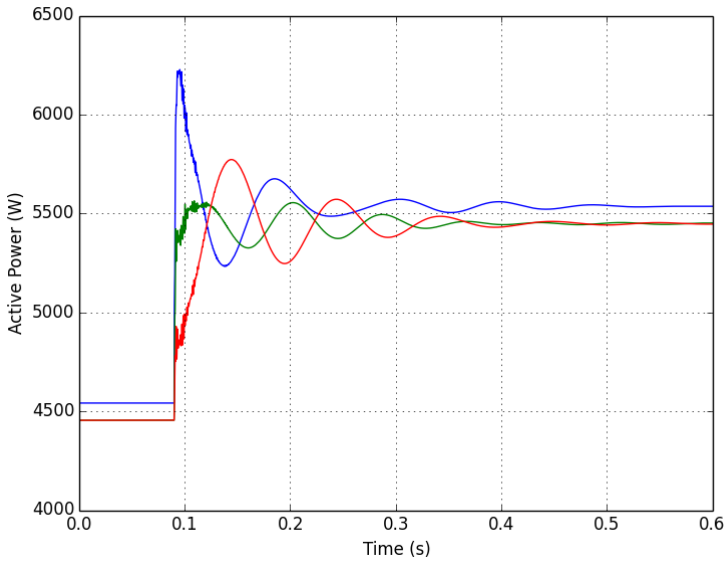

(c)

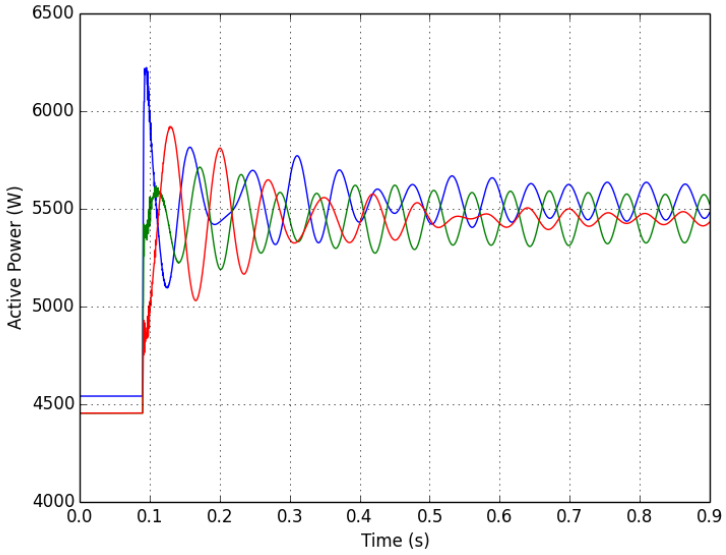

(d)

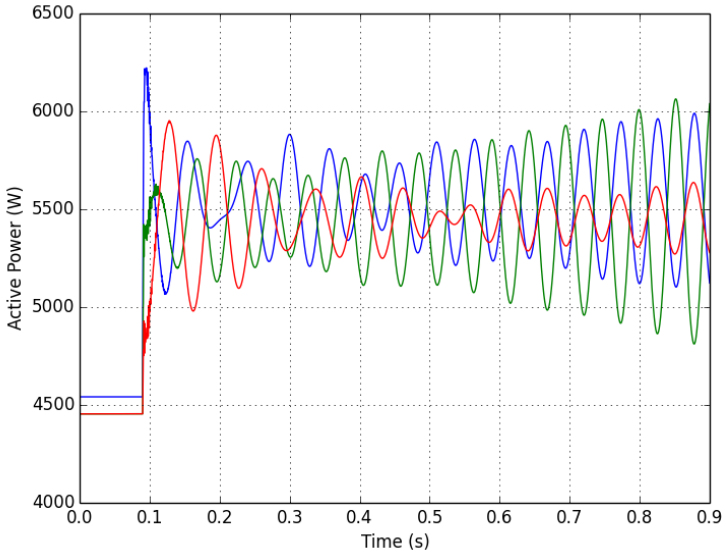

Figure 4.2. Model validation results, (a) eigenvalue trajectory with m changed in 10^{-4} increments, (b) stable case, $m = 1 \times 10^{-3}$, (c) critically stable case, $m = 1.9 \times 10^{-3}$, (d) unstable case, $m = 2.1 \times 10^{-3}$

It should be noted that the initial conditions calculated by the proposed load flow method, while stable, may not be a state that a practical microgrid moves to and stays at. Furthermore, the load flow method only calculates initial conditions at the fundamental frequency and neglects voltage and current harmonics, which may also have an influence on small-signal stability. Therefore, the developed technique could

be used as a screening tool in the planning phase of a project, where a microgrid network design is checked for stability and the converter parameters are tuned to ensure that small-signal stability is achieved.

4.2 Network Parameter Sensitivity Analysis

Since the steady-state initial values are calculated by a load flow simulation, it follows that a sensitivity analysis involving network quantities can be easily automated. The same test network described in Section 4.1.1 is used to perform the sensitivity of the microgrid to changes in the following network parameters: i) line impedances, ii) line X/R ratios, and iii) load power factor.

4.2.1 Sensitivity to Line Impedances

Impedances of both lines adjusted linearly from $Z_{L1} = 0.3\,\Omega$ and $Z_{L2} = 0.68\,\Omega$ to $Z_{L1} = 6.4\,\Omega$ and $Z_{L2} = 14.2\,\Omega$. The eigenvalue trajectories are shown in Figure 4.3. This figure shows that increasing the line impedances moves the eigenvalues right along the real axis but does not lead to instability.

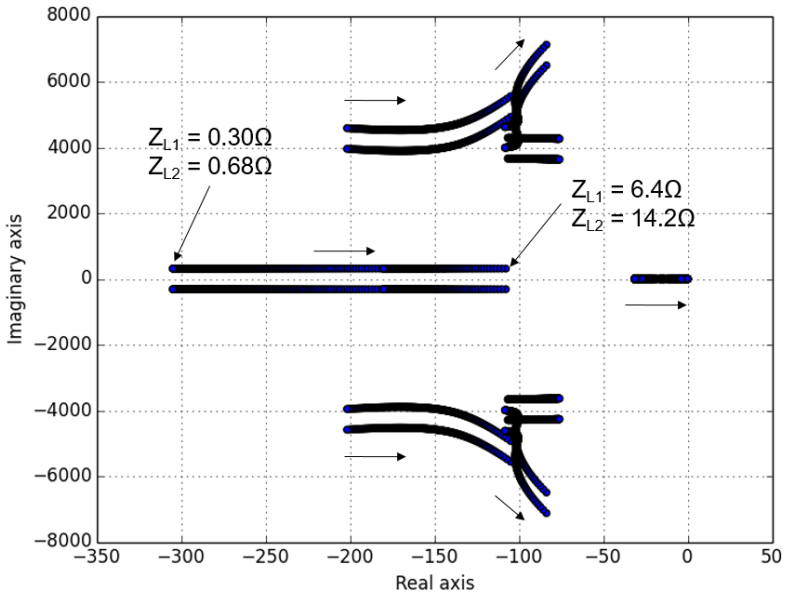

Figure 4.3. Sensitivity to line impedances

4.2.2 **Sensitivity to Line X/R Ratios**

Line X/R ratios adjusted from $X/R_{L1} = 0.87$ and $X/R_{L2} = 1.66$ to $X/R_{L1} = 0.009$ and $X/R_{L2} = 0.017$, with the respective line impedances remaining constant. The eigenvalue trajectories are shown in Figure 4.4. This figure shows that decreasing the line X/R ratios moves the eigenvalues right along the real axis and decreases damping but does not cause instability.

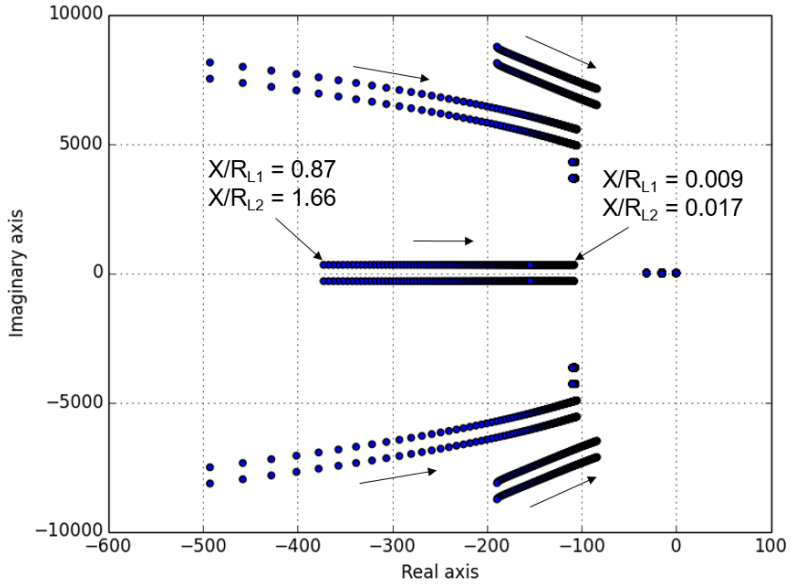

Figure 4.4. Sensitivity to line X/R ratios

4.2.3 **Sensitivity to Load Power Factor**

Load power factors adjusted from $pf = 1.0\,pf$ to $pf = 0.13\,pf$, with active power demand remaining constant. The eigenvalue trajectories are shown in Figure 4.5. As seen from the figure, the system becomes unstable at very low power factors, e.g., in the vicinity of $0.13\,pf$.

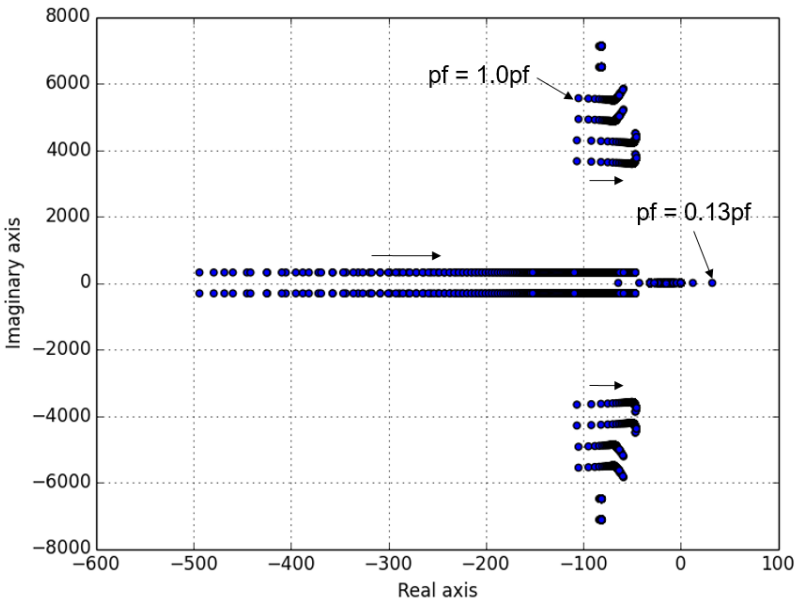

Figure 4.5. Sensitivity to load power factor

4.3 **Impact of Microgrid Topology**

To facilitate an analysis of different microgrid topologies and operating points, it is desirable to automatically generate random microgrid networks. The following algorithm was developed for generating a random microgrid network:

a) Generate random number of nodes in microgrid, $N \sim U[n_{min}, n_{max}]$ where n_{min} and n_{max} are the minimum and maximum number of nodes, respectively.

b) Generate random number of converters in microgrid, $N_c \sim U[1, N]$ and locations. Randomly select node locations for each converter. Set converter-1 at node-1 (the slack bus).

c) Generate random number of loads in microgrid, $N_l \sim U[1, N]$ and locations.

d) Generate random total apparent power demand in microgrid, $S_{tot} \sim U[0, S_{c,tot}]$, where $S_{c,tot}$ is total capacity of VSCs.

e) Generate individual load active and reactive power demands and converter dispatches using normalised random weight vectors.

f) Generate line resistances, $R_l \sim U[0, R_{max}]\ \Omega$, and X/R ratios, $X/R \sim U[0, X/R_{max}]$, where R_{max} and X/R_{max} are the maximum line resistance and X/R ratio respectively.

The parameters considered in this research are listed in Table 4.1 below.

Table 4.1. Randomly generated microgrid parameters

Parameter Description	Symbol	Value
Minimum number of nodes	n_{min}	3
Maximum number of nodes	n_{max}	20
Individual converter capacity	S_c	10 kVA
Maximum line resistance	R_{max}	1 Ω
Maximum X/R ratio	X/R_{max}	20

The number of lines and their interconnection with nodes depend on the desired microgrid network topology. In this study, the three basic topologies in Figure 4.6 are analysed, i.e.,

a) Radial (*daisy-chain*): $N - 1$ lines

b) Ring: N lines

c) Triangular mesh: $2N - 3$ lines

A randomly generated microgrid is considered to be valid if a steady-state solution is found (i.e., the load flow converges) and bus voltages are all within a range of 0.6 to 1.15pu.

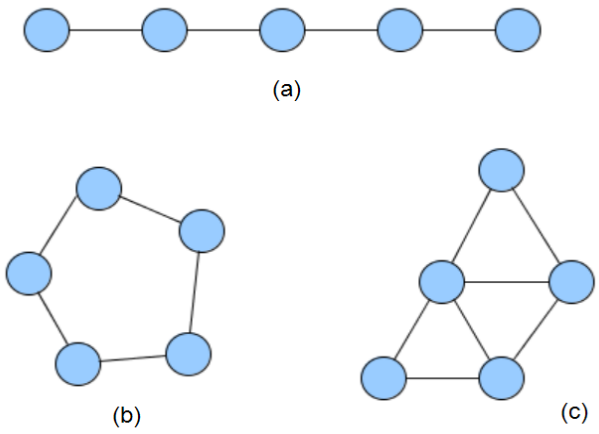

Figure 4.6. Basic microgrid topologies, (a) radial, (b) ring, (c) triangular mesh

A Monte Carlo analysis using 15,000 randomly generated microgrids was conducted to investigate the effects of network topology on microgrid small-signal stability. The parameters in Table 4.1 were used to create each randomly generated microgrid sample. The stability margin, which is defined as the active power droop gain (m) at which the system is critically stable, was then calculated for each randomly generated microgrid.

The results in Figure 4.7a show a basic scatter plot of the stability margins for each of three basic topologies analysed. It can be seen that the radial topology has the highest stability margins, followed by the ring and then triangular mesh topologies. The implication is that greater network meshing leads to lower small-signal stability (in general). Figure 4.7b presents the stability margin plotted against converter minimum distance, which is the minimum electrical distance (in Ohms) between two converters in a microgrid. The plot shows that there is a fairly strong positive correlation ($r = 0.8945$) between minimum distance and stability margin, i.e., higher minimum distance leads to higher stability.

(a)

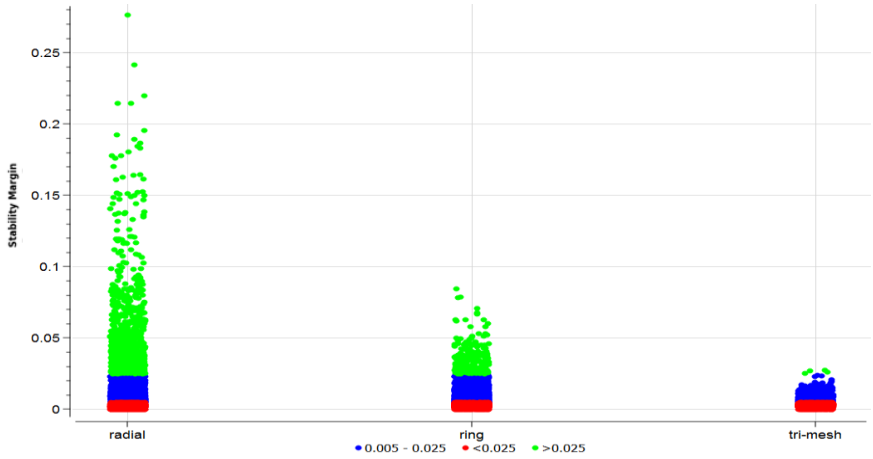

(b)

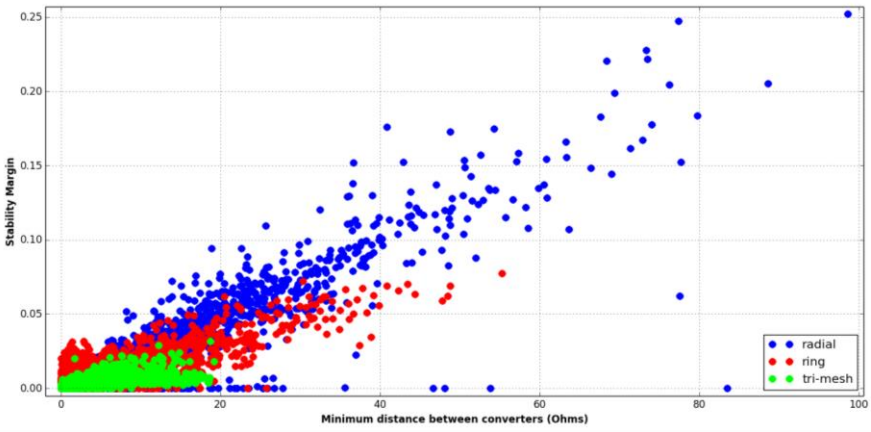

Figure 4.7. Monte Carlo analysis results, (a) stability margin vs topology, (b) stability margin vs minimum converter distance

This is consistent with observations in [14] and in the results herein that reducing the impedance of the line between two converters leads to instability. When two converters are separated by a low impedance, there is potentially more active power exchange and converter interactions during load-generation fluctuations which the simulations imply can lead to more unstable operating conditions. Table 4.2 shows the microgrid network properties with the highest correlation coefficients. It can be seen that apart from the minimum converter distance, the other network properties are more or less linearly uncorrelated with the stability margin.

Table 4.2. Correlation coefficients for microgrid network properties

Network Property	r
Number of converters	-0.2830
Total microgrid active power	-0.2211
Average voltage magnitude	-0.2170
Total microgrid reactive power	-0.2107
Maximum load	-0.1818
Average line impedance	0.1910
Minimum converter distance	0.8945

4.4 **Summary**

In this chapter, the proposed method for initialising small-signal models of microgrids with a load flow simulation was validated to be accurate via time-domain simulations. The proposed approach facilitates the rapid assessment of small signal stability in a converter-dominated microgrid system over a range of network conditions (e.g., loads, topologies, etc).

Using the proposed initialisation method and a series of Monte Carlo simulations, this study also examined how network characteristics and topology can affect the small-signal stability of a converter-dominated microgrid. The results of the study show distinct differences in stability margins with respect to microgrid topology and the electrical distances between two adjacent converters. Simple radial topologies are found to be the most stable, though are less resilient to faults on the microgrid from a reliability perspective. The greater the level of meshing, the less stable the system becomes.

Chapter 5 Interconnecting Microgrids for Dynamic Frequency Support

This chapter presents the performance evaluation of the back-to-back dc link connecting neighbouring microgrids as proposed in Section 3.2, with the objective of providing dynamic frequency stability support. The performance evaluation is performed via computer simulations of three operating states, i) normal operation with both microgrid clusters running autonomously and requiring no support, ii) overload operation of one microgrid cluster without support from the back-to-back dc link, and finally iii) overload operation of one microgrid with support from the other microgrid via the back-to-back dc link.

5.1 Test Network

The interconnected microgrid structure comprising two microgrid clusters and a back-to-back dc link (as shown in Figure 3.3a) is modelled. Each microgrid cluster is topologically identical as shown in Figure 3.3b. The DERs in each microgrid comprise one 6 kVA diesel generator, as modelled in Figure 3.3c and two 10 kW three-phase converter-interfaced DER units, as modelled in Figure 3.3d. Each microgrid cluster is assumed to be a low voltage (415 V) system with two PQ loads connected. A combined engine, flywheel and alternator inertia constant of H = 1 s is used for the diesel generator set.

At steady state, each microgrid cluster operates autonomously, with the DERs supplying the loads in the microgrid. The primary controllers in each DER are set to 5% voltage and frequency droop, while the secondary controllers are set to recalculate the voltage and frequency reference values at discrete intervals of 3 seconds. The interchange converter consists of two 30 kVA converters, as shown in Figure 3.5a with 3% series coupling inductances connected together via a line with total resistance of 1.2 Ω.

The operation of the proposed interconnected microgrid system is investigated through simulations in DIgSILENT PowerFactory v15.1 software.

5.2 Microgrid Normal Operation

During normal operation, the local DERs in each microgrid supply the active and reactive power demand of the local loads. In Case 1, a modest load step is simulated in MG-1 such that the total load after the event is still within the combined capacity of the DER units.

To investigate the performance of the interconnected microgrid system under such a condition, let us assume that in the steady state, each microgrid has a load demand of 5kW at pf = 0.85 lagging. It is also assumed that, based on the secondary controller, this power is shared with a ratio of 60/40 % between the two converter-interfaced DERs while the diesel generator is assumed to be running at no-load condition. The microgrid frequency and voltage magnitude are respectively 50 Hz and 1.001 pu. The results of the simulation are shown in Figure 5.1.

At t = 1 s, a 3 kW load (with pf = 0.85 lagging) is added to MG-1 (Figure 5.1a). It can be seen that this additional demand is picked up by the two converter-interfaced DERs (i.e., converter-A, B) from both active power (Figure 5.1b) and reactive power

(Figure 5.1c) points of view, based on the assigned 60/40 % ratio. It is to be noted that although the diesel generator contributes during the transient period, it does not contribute to this additional load when the system reaches the steady-state condition at t = 12.5 s (Figure 5.1b-c).

The microgrid frequency is restored to 50 Hz when the system reaches the steady-state condition (Figure 5.1d) while the voltage rms restores back to 1 pu at this time (Figure 5.1e).

Due to the slight changes in the dc link voltage (Figure 5.3c), the step load applied to MG-1 causes some oscillations in the system of MG-2; however, these oscillations are damped very quickly. At steady-state, it can be seen that the additional load demand in MG-1 is adequately supplied by the local DERs (converter-A and B), and there is very limited contribution from converter-C and D in MG-2 (Figure 5.2a-b). Hence, the frequency and voltage rms of MG-2 restore back to their initial values (Figure 5.2c-d). The presence of the interchange converter causes the frequency disturbance in MG-1 to ripple through to MG-2, but the effects are very small (i.e., 0.3%). The active and reactive power exchange through the interchange converter is negligible at this condition (Figure 5.3a-b).

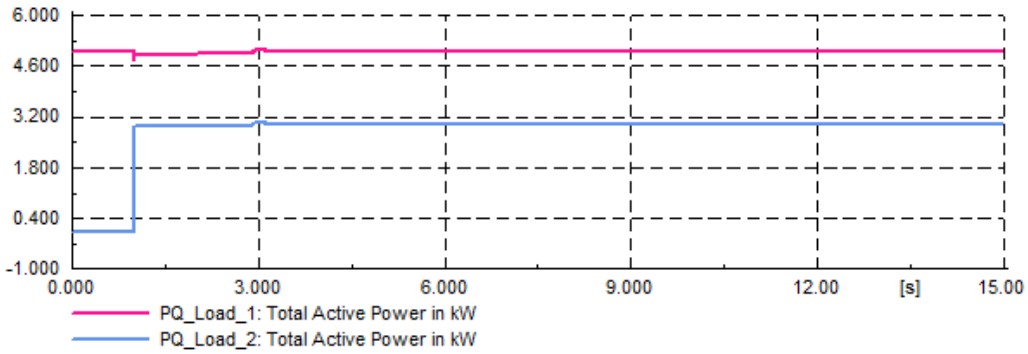

a) Load demand on MG-1

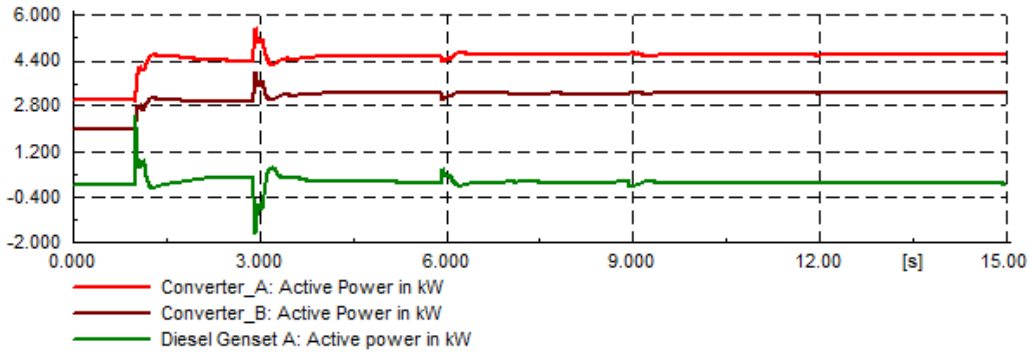

b) Active power output of DERs in MG-1

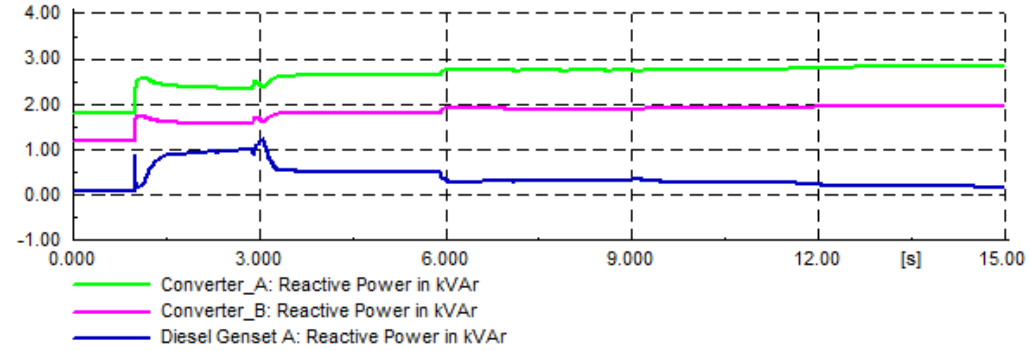

c) Reactive power output of DERs in MG-1

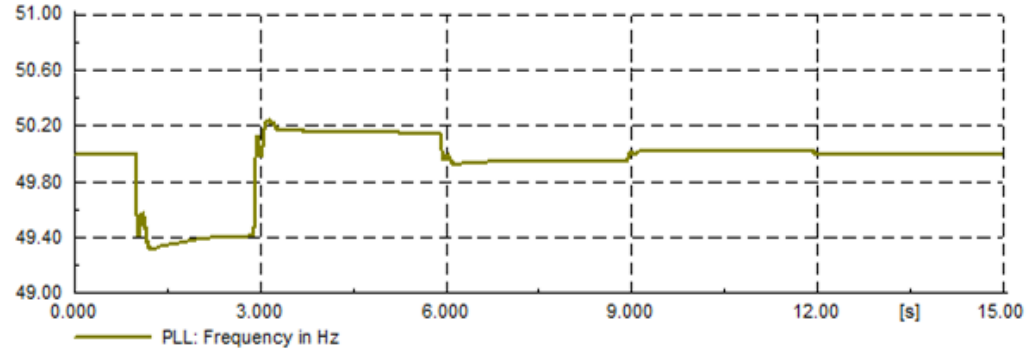

d) MG-1 frequency

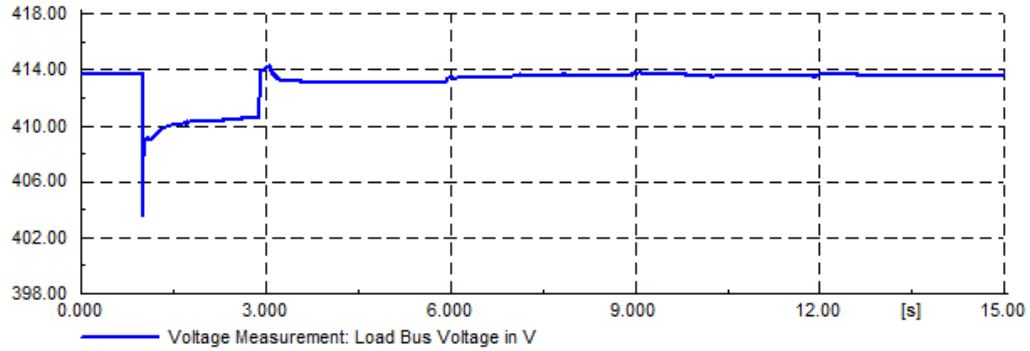

e) MG-1 voltage (rms)

Figure 5.1. Case 1 simulation results – MG-1

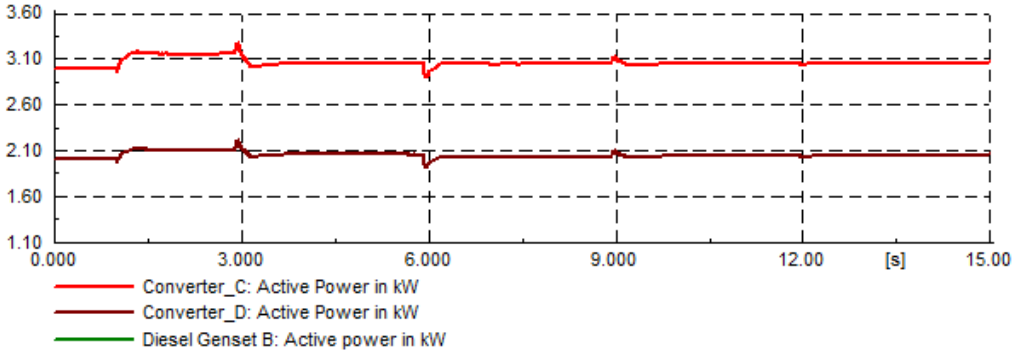

a) Active power output of DERs in MG-2

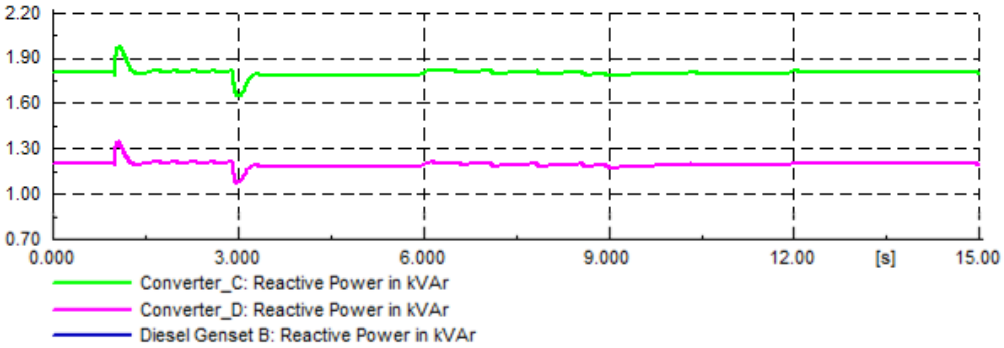

b) Reactive power output of DERs in MG-2

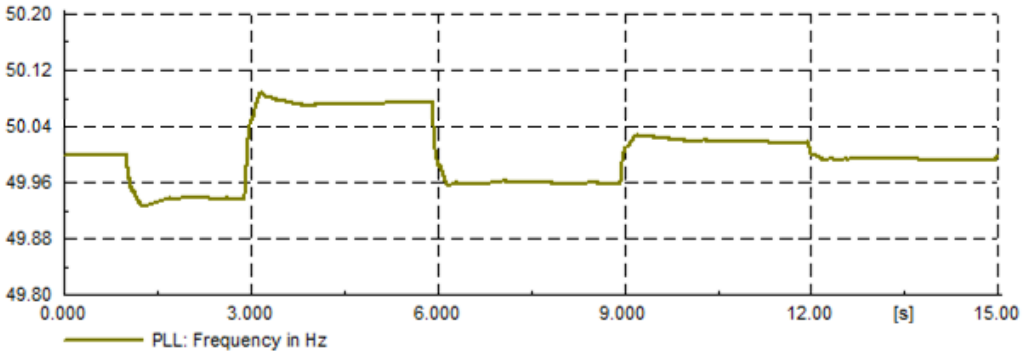

c) MG-2 frequency

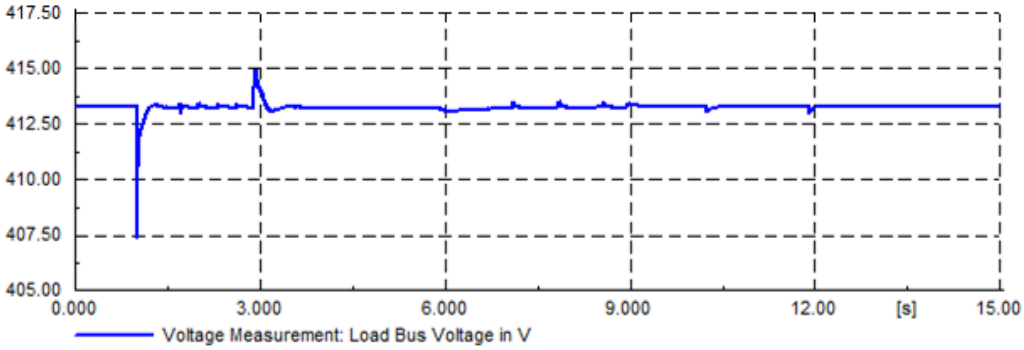

d) MG-2 voltage (rms)

Figure 5.2. Case 1 simulation results – MG-2

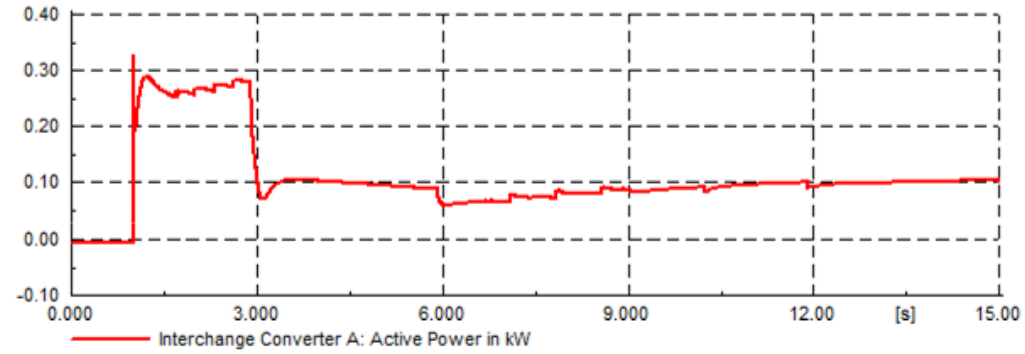

a) Active power exchange over interchange converter

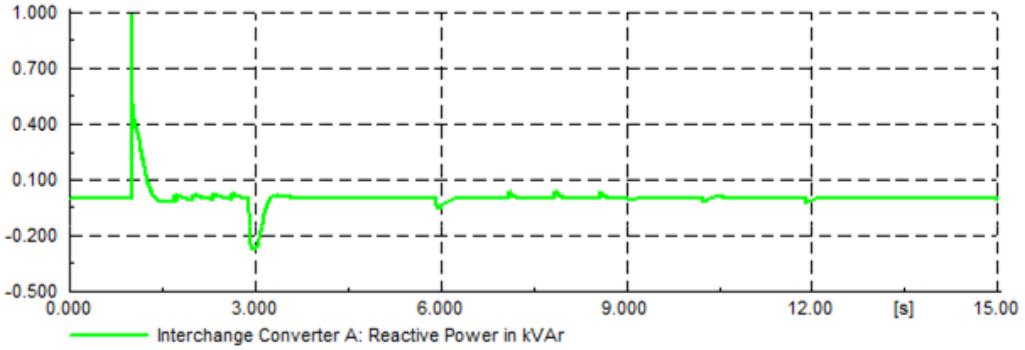

b) Reactive power exchange over interchange converter

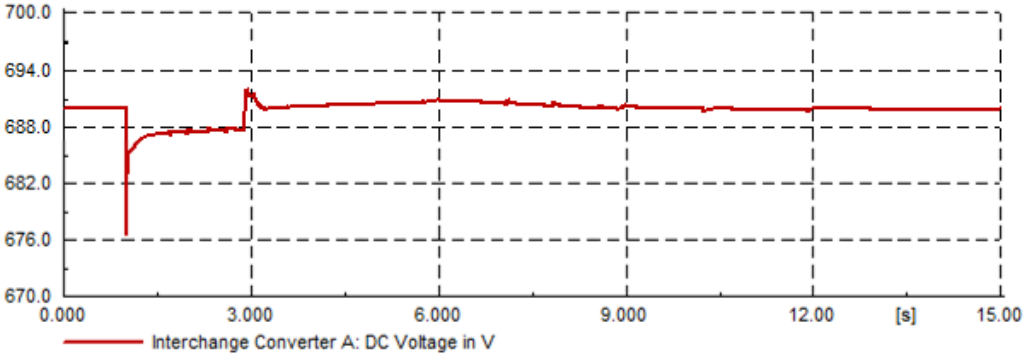

c) dc link voltage

Figure 5.3. Case 1 simulation results – Interchange converter

5.3 **Microgrid Overload Operation without Interchange Converter**

When one of the microgrids is overloaded, the total load demand in a microgrid exceeds the generation/storage capacity of the DERs. In Case 2, the performance of the microgrid is first examined without the influence of the interchange converter.

Let us assume in the steady state, MG-1 has a load demand of 16 kW while MG-2 has a load demand of 5kW, both at pf = 0.85 lagging. It is also assumed that, based on the secondary controller, in each microgrid this power is shared with a ratio of 60/40

% between the two converter-interfaced DERs while the diesel generator is assumed to be running at no-load condition.

At t = 1 s, a 10 kW load demand (with pf = 0.85 lagging) is added to MG-1 (Figure 5.4a), bringing the total load demand to 26 kW and thereby overloading MG-1. The results of the simulation are shown in Figure 5.4 for MG-1.

As expected, it can be seen that the DERs in MG-1 reach their active and reactive power limits (i.e., 10 kVA) quickly after the load change (Figure 5.4b-c). As a result of the overloading condition, the frequency and voltage decline rapidly to below the acceptable limits of 49 Hz and 0.9 pu voltage within 1.3 seconds (Figure 5.4d-e).

The diesel generator also reaches its active power limit soon after the load change (Figure 5.4b), but the overloading condition causes the rotational speed of the shaft to slow down and consequently a decline in frequency.

Under-frequency or under-voltage protection relays are not modelled in this research, but such an overloading condition would result in load shedding through the activation of under-frequency or under-voltage relays or in the worst case, a system blackout.

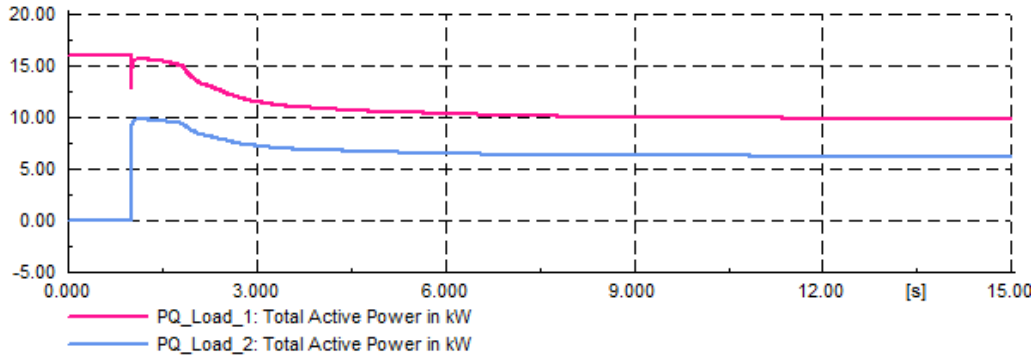

a) Load demand on MG-1

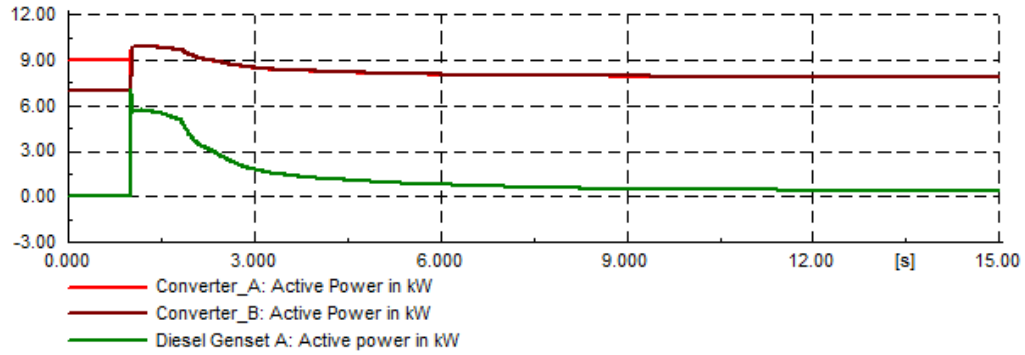

b) Active power output of DERs in MG-1

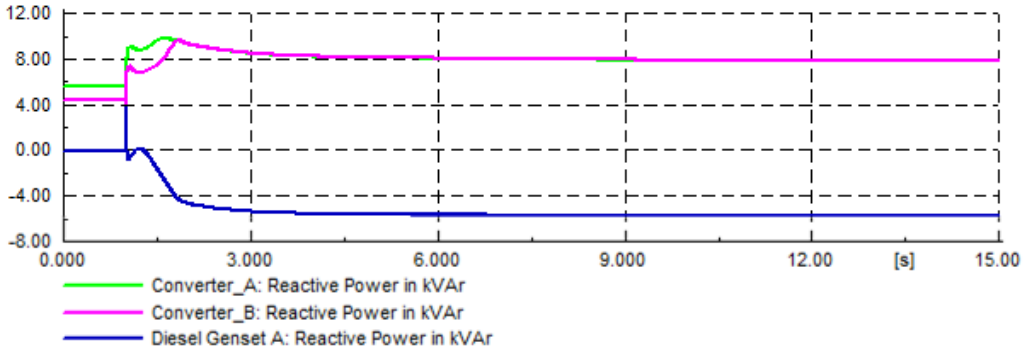

c) Reactive power output of DERs in MG-1

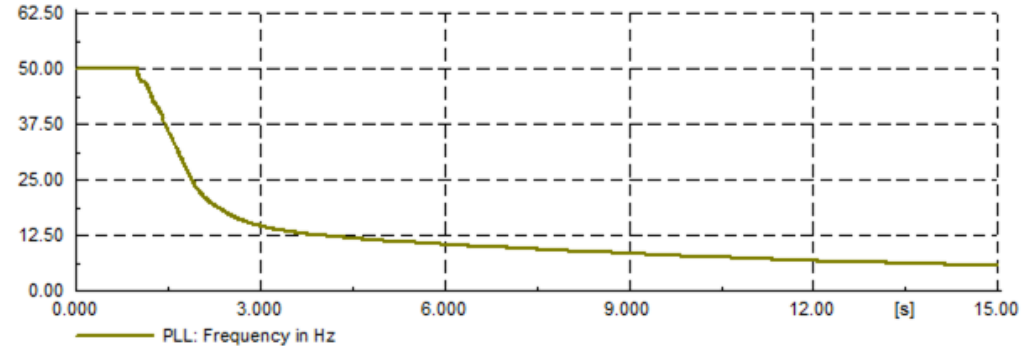

d) MG-1 frequency

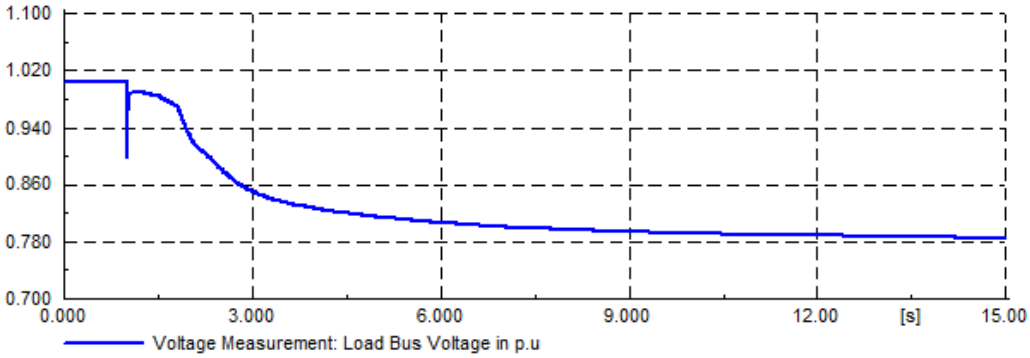

e) MG-1 voltage (rms)

Figure 5.4. Case 2 simulation results

5.4 Microgrid Overload Operation with Interchange Converter

The interchange converter is intended to provide frequency support by facilitating active power exchange between microgrid clusters (in the event of overloading within one microgrid cluster). In Case 3, the interchange converter is put in service and the overload simulation in Case 2 is repeated.

Let us assume the steady state conditions same as Case 2. At t = 1 s, a 10 kW load demand is added to MG-1. The results of the simulation are shown in Figure 5.5.

For the power demand variation in MG-1 (Figure 5.5a), similar to Case 2, the DERs in MG-1 (converter-A and B) quickly reach their active and reactive power limits of 10 kVA (Figure 5.5b-c) and the frequency and voltage rms in MG-1 drops (Figure 5.5d-e). However in this case, the DERs (converter-C and D) increase their output power with the pre-assigned ratio of 60/40 % (Figure 5.6a-b). Hence, after this increase, the frequency of MG-2 is decreased from 50 Hz to 49.2 Hz (Figure 5.6c) and the voltage rms drops from 1.00 pu to 0.96 pu (Figure 5.6d), after the increase in the output power of these two converters.

The diesel generator in MG-1 increases its active power output in response to the load change and quickly reaches its limits. However, the active power support from MG-2 allows the diesel generator to reduce its power output, finally settling at 1.6 kW through droop control action (Figure 5.5b). There is negligible response from the diesel generator in MG-2.

Hence, based on the frequency drop in MG-1, the interchange converter acts to facilitate active power transfer of approximately 5 kW and zero kVAr from MG-2 to MG-1 (Figure 5.7a-b), allowing the frequency and voltage in MG-1 to recover to nominal values.

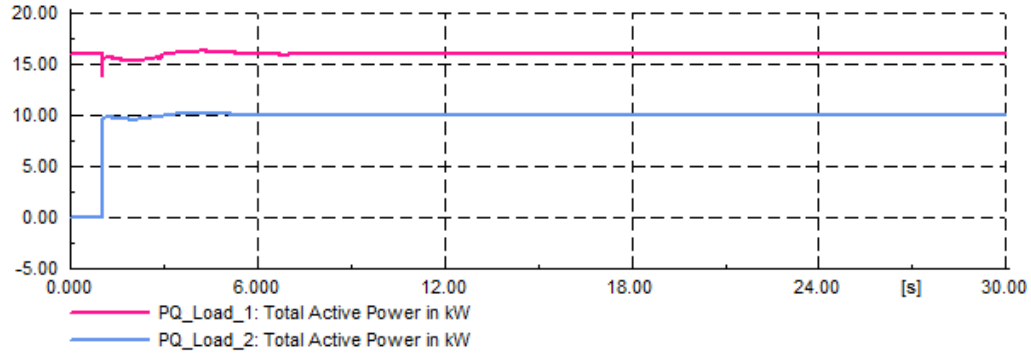

a) Load demand on MG-1

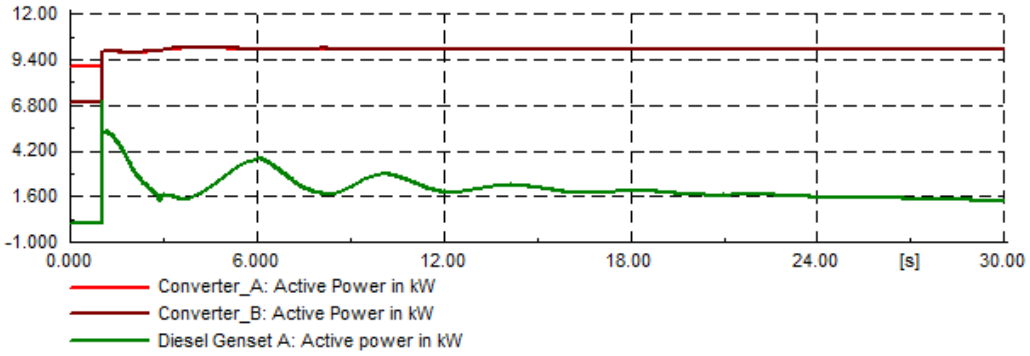

b) Active power output of DERs in MG-1

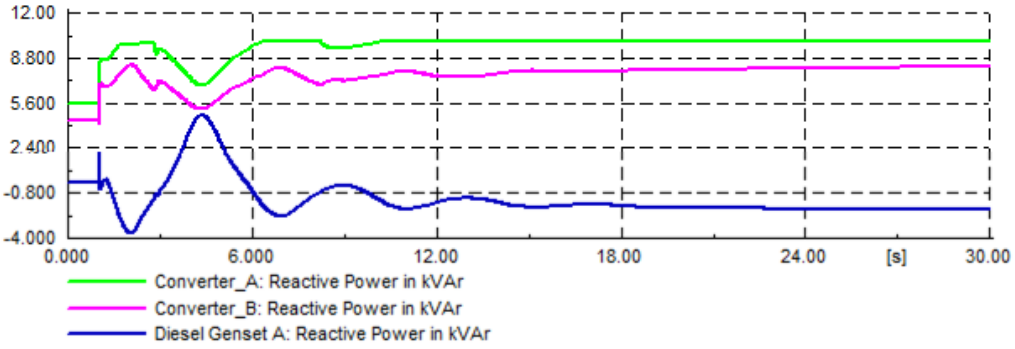

c) Reactive power output of DERs in MG-1

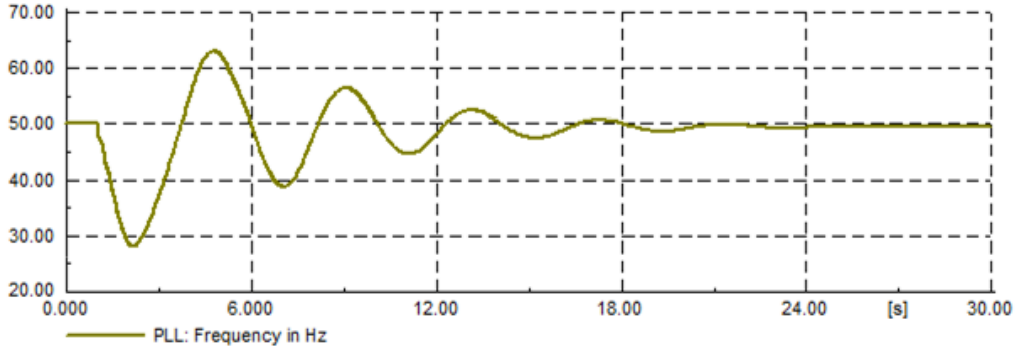

d) MG-1 frequency

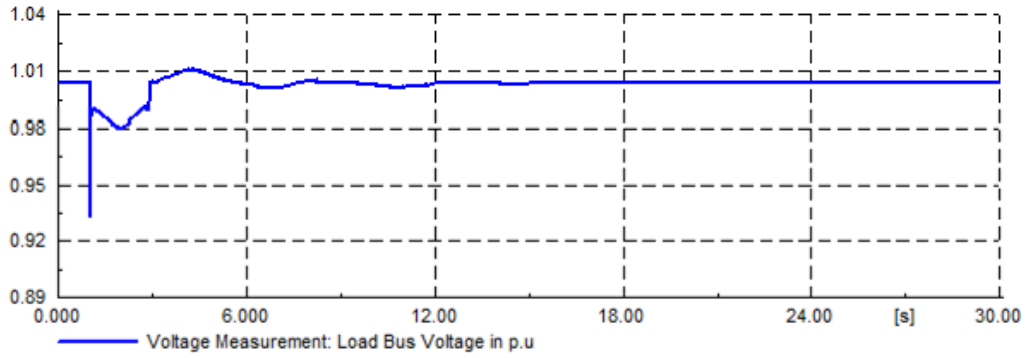

e) MG-1 voltage (rms)

Figure 5.5. Case 3 simulation results – MG-1

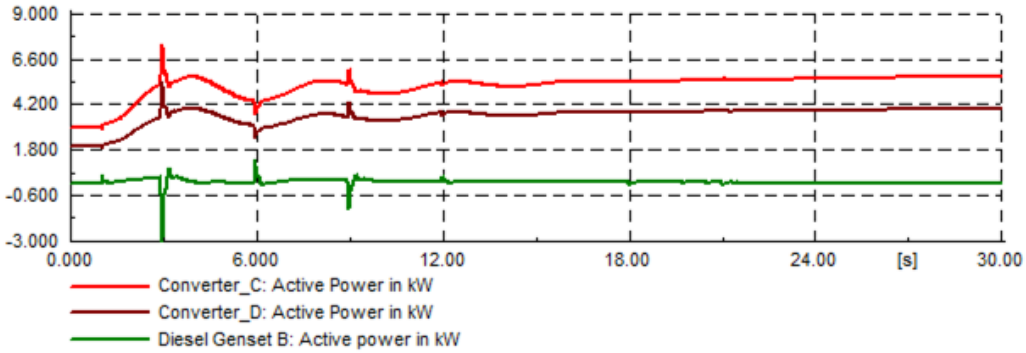

a) Active power output of DERs in MG-2

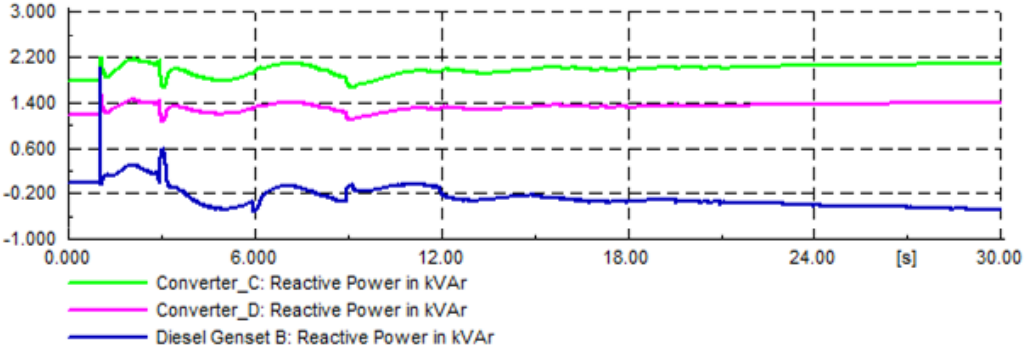

b) Reactive power output of DERs in MG-2

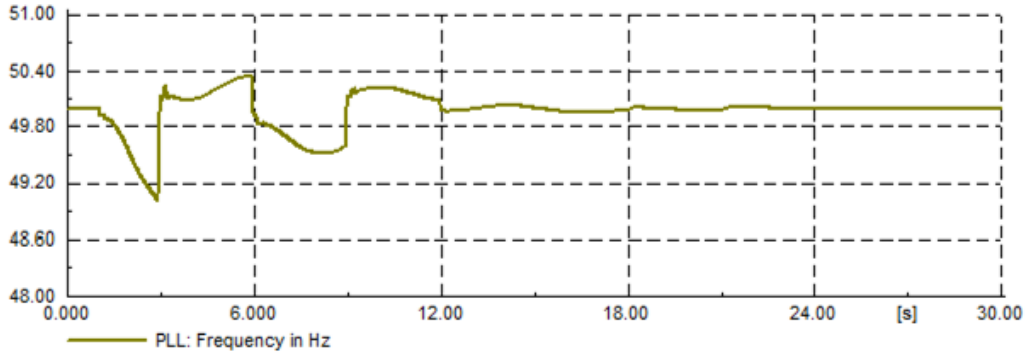

c) MG-2 frequency

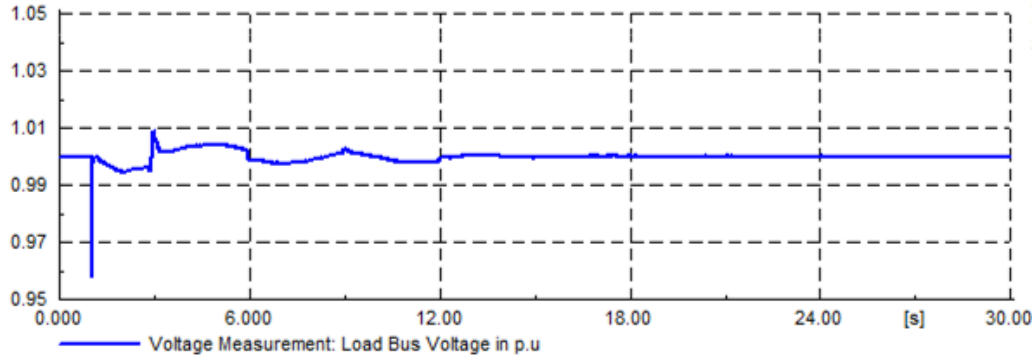

d) MG-2 voltage (rms)

Figure 5.6. Case 3 simulation results – MG-2

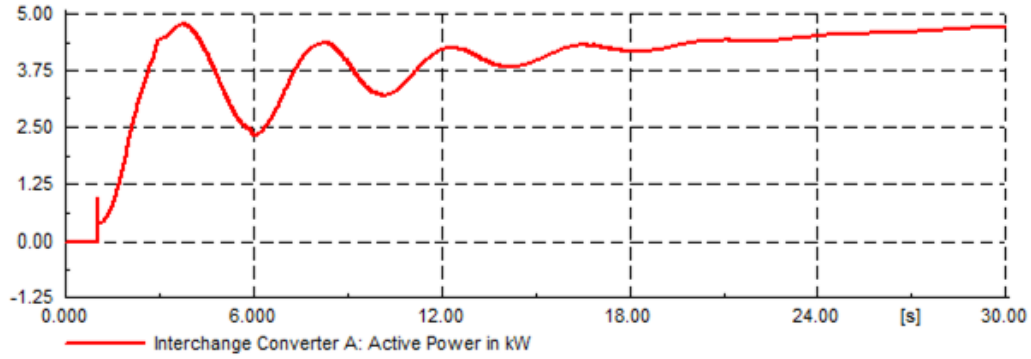

a) Active power exchange over interchange converter

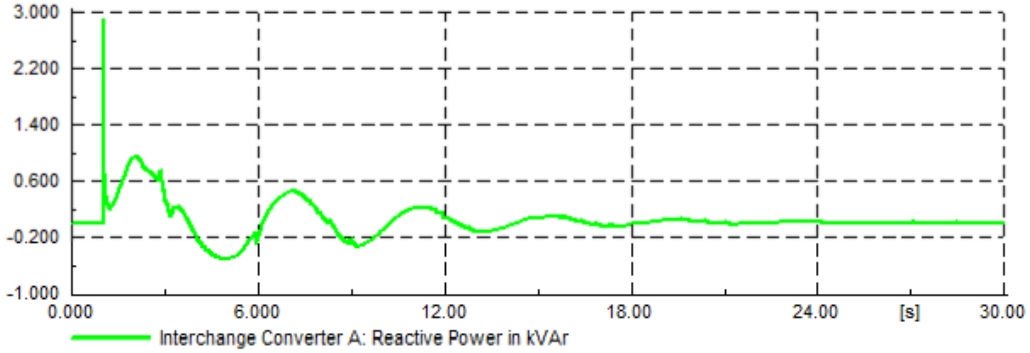

b) Reactive power exchange over interchange converter

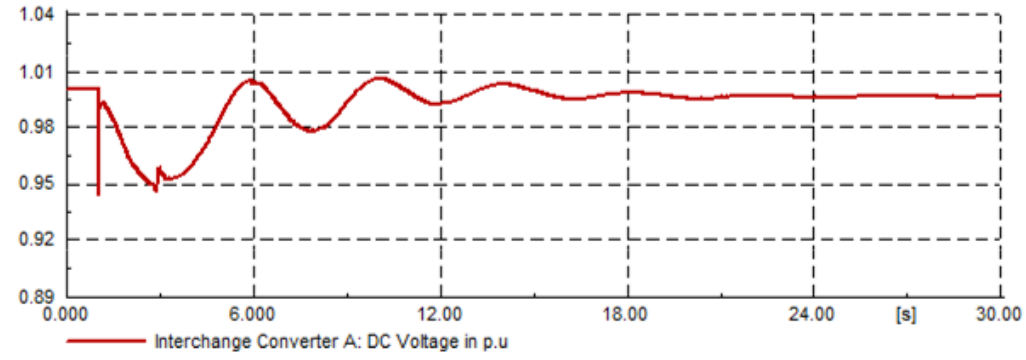

c) dc link voltage

Figure 5.7. Case 3 simulation results – Interchange converter

5.5 **Summary**

The concept of interconnecting two neighbouring autonomous microgrids via a back-to-back dc link (interchange converter) has been analysed as a method to improve frequency stability and prevent load shedding or frequency collapse. This interconnection configuration provides dynamic frequency support for the microgrids in case of overloading or deficiency in power generation in either of the microgrid clusters. Through the simulation studies, it is demonstrated that the interchange converter successfully facilitates active power flow from one microgrid to the other microgrid based on the frequency deviation.

However, it should be noted that interconnected microgrids are not necessarily more stable than standalone microgrids. For example, excessive overloads and/or faults in one microgrid could be transferred to an interconnected microgrid and potentially cause the collapse of both systems. Interconnecting microgrids could also lead to small-signal instability due to the interaction of fast power electronic control systems [28].

Chapter 6 Optimal Smoothing Battery Sizing for PV-Diesel Microgrids

In this chapter, the optimal smoothing battery sizing method proposed in Section 3.3 is applied to a simulated test microgrid using real solar irradiance measurement data from the Australian Bureau of Meteorology. The proposed method is compared against other smoothing battery sizing methods found in the literature and a sensitivity analysis is performed on some of the key input parameters to the model.

6.1 Performance Evaluation

The hybrid PV-diesel microgrid shown in Figure 3.8 is considered in the performance evaluation studies. The microgrid comprises a standard crystalline silicon PV array connected via a grid-tied inverter and a deep-cycle valve regulated lead-acid smoothing battery connected to the microgrid via a bi-directional converter.

The modelling of the PV and smoothing battery are as per Section 3.3.2 and the model parameters for the PV modules are as per Table 6.1. The smoothing battery's assumed discharge characteristics are based on an Olympic Batteries DC2-500 type battery [137], as listed in Table 6.2, and used to estimate the parameters in the assumed Kinetic battery model. The bi-directional converter for the smoothing battery is considered to have an efficiency of 94%, based on data from a Tier-1 manufacturer [138].

Table 6.1. Considered PV parameters in the simulations

Parameter	Symbol	Value	Remarks
PV nominal rating	P_{nom}	1000 [Wp]	
Environmental derating factor	k_e	90 [%]	Assuming light to moderate soiling and dust
Manufacturer output tolerance	k_m	95 [%]	AS/NZS 4509.2 Recommendation [111]
Power-temperature coefficient	k_{pt}	0.38 [%]	Datasheet value for a crystalline silicon module from a Tier-1 manufacturer [139]
Inverter efficiency	η_{inv}	95 [%]	Average value for a grid-tied PV inverter from a Tier-1 manufacturer [140]

Table 6.2. Smoothing battery's discharge characteristics [137]

Discharge time (hours)	1	3	5	8	10
Discharge current (A)	242.4	115.7	79.8	55.23	47.01

For the base case optimisation studies, the smoothing battery's DoD is assumed as 70% and the smoothing battery is configured at the beginning of each day with an initial SoC of 80%. The ambient temperature data is retrieved from the Bureau of Meteorology; however, only historical daytime maximum temperatures for each day were accessible in the public dataset. Therefore, the ambient temperature is assumed to be constant through-out the day and set as the historical maximum temperature in the studies. This is a conservative assumption and leads to a higher temperature derating of the PV's output power.

6.1.1 **Single Day Study Results**

The simulation model is run for a 24-hour period for site-1 on 5/2/2017 to illustrate the effects of the moving average and ramp rate-based techniques on the smoothing battery's output power and the final smoothed output from the combined PV-battery system. The considered day is a mixed-sky day with a moderately high $SIVI$ of 20.91. For the single day simulations, an unoptimised smoothing battery capacity of 1 kWh is applied in order to facilitate comparisons of the smoothing battery's performance between simulation results. The results of the study are demonstrated in Figure 6.1 and Figure 6.2, respectively for the moving average and ramp rate-based techniques. For each technique, the study was conducted with two different smoothing parameters (i.e., moving average window and ramp rate limit) to demonstrate the impact of more onerous smoothing requirements. As can be seen from these figures, a larger moving average window (20 vs 5 min) or a tighter ramp rate limit (1 vs 10%) produces a smoother output, but at the cost of a higher SBOC.

6.1.2 **Smoothing Battery Optimisation Results**

The detailed method described in Section 3.3.2 has been applied for the 11 sites of Table 3.1, for each day over the full calendar year of 2017. Figure 6.3a and b illustrate the results for 4 sites when respectively the moving average and ramp rate techniques are employed.

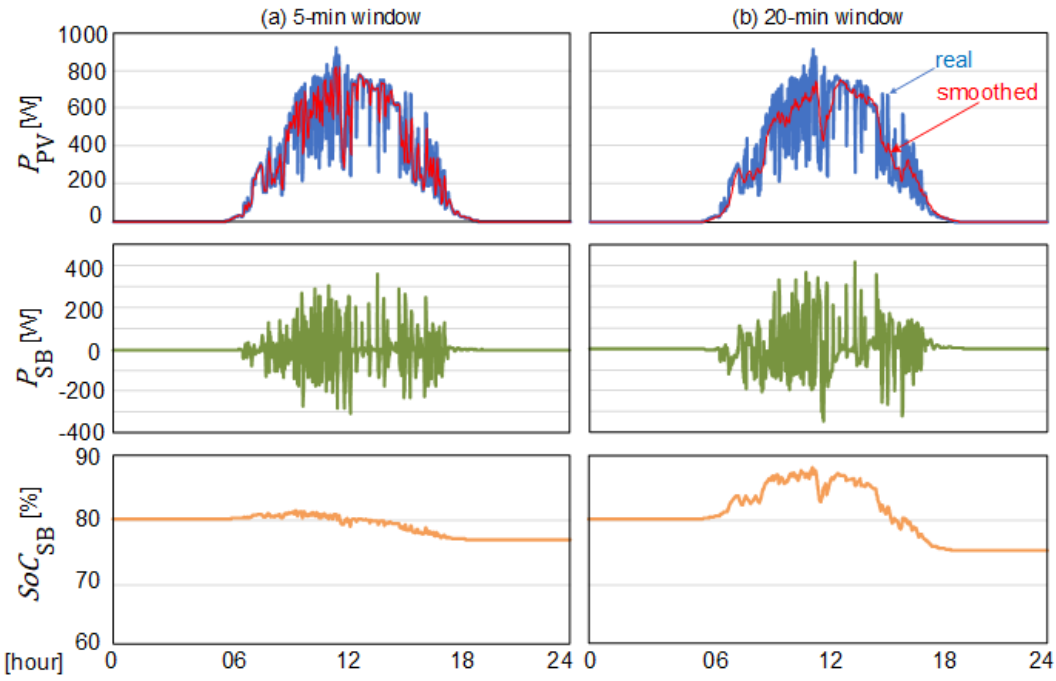

Figure 6.1. Performance of the microgrid in Figure 3.8 when using a smoothing battery, defined under the moving average technique for a single day (15/02/2017 at site-1) with a window of (a) 5, (b) 20 minutes

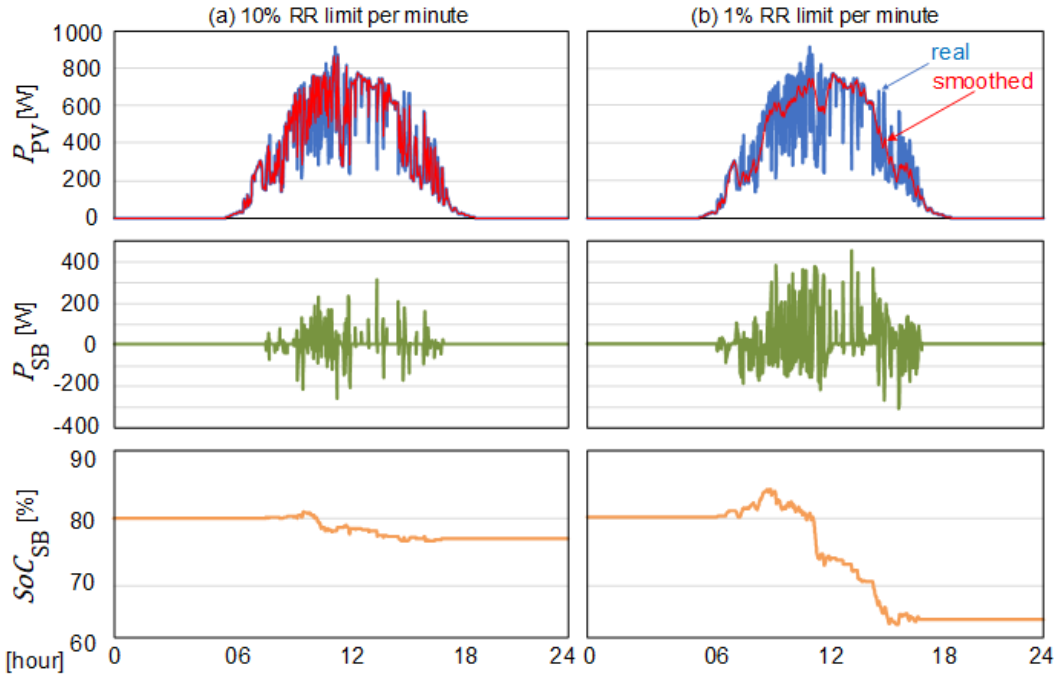

Figure 6.2. Performance of the microgrid in Figure 3.8 when using a smoothing battery, defined under the ramp rate technique for a single day (15/02/2017 at site-1) assuming a ramp rate limit of (a) 10%, (b) 1%

The study attempts to determine the minimum SBOC, required to meet the selected smoothing criteria, for a given day and site. For each site, the results are presented as a scatter plot where each point represents the smoothing battery's optimised capacity for a single day (on the y-axis) and the corresponding SIVI for that day (on the x-axis). An empirical CDF of the optimised smoothing battery capacities over the full year is also shown to illustrate how the optimisation results are distributed and aid in the SBOC's selection.

The optimisation results are expressed in kWh of the smoothing battery's capacity per kWp of the PVs, and can be scaled linearly to any desired PV capacity. As such, if the optimisation results yield an SBOC of 0.4 kWh per kWp, then a 100 kWp PV would require a smoothing battery with a capacity of 40 kWh.

The optimisation results for the moving average-based technique in Figure 6.3a illustrates a clear positive correlation between the SBOC and the SIVI. This result is according to the general expectation of observing higher levels of smoothing battery's charge/discharge during days of high SIVI and vice versa. However, the results for the ramp rate-based technique in Figure 6.3b demonstrate a weaker correlation between the SBOC and the SIVI. Indeed, a comparison of the Pearson correlation coefficients between the SBOC using the moving average and ramp rate techniques with the observed SIVI in Table 6.3 indicates that, across all studied sites, the ramp rate-based technique is less strongly correlated than the moving average-based technique (e.g., the average correlation coefficient across all sites is 0.7862 when using the moving average technique versus 0.5556 when the ramp rate technique).

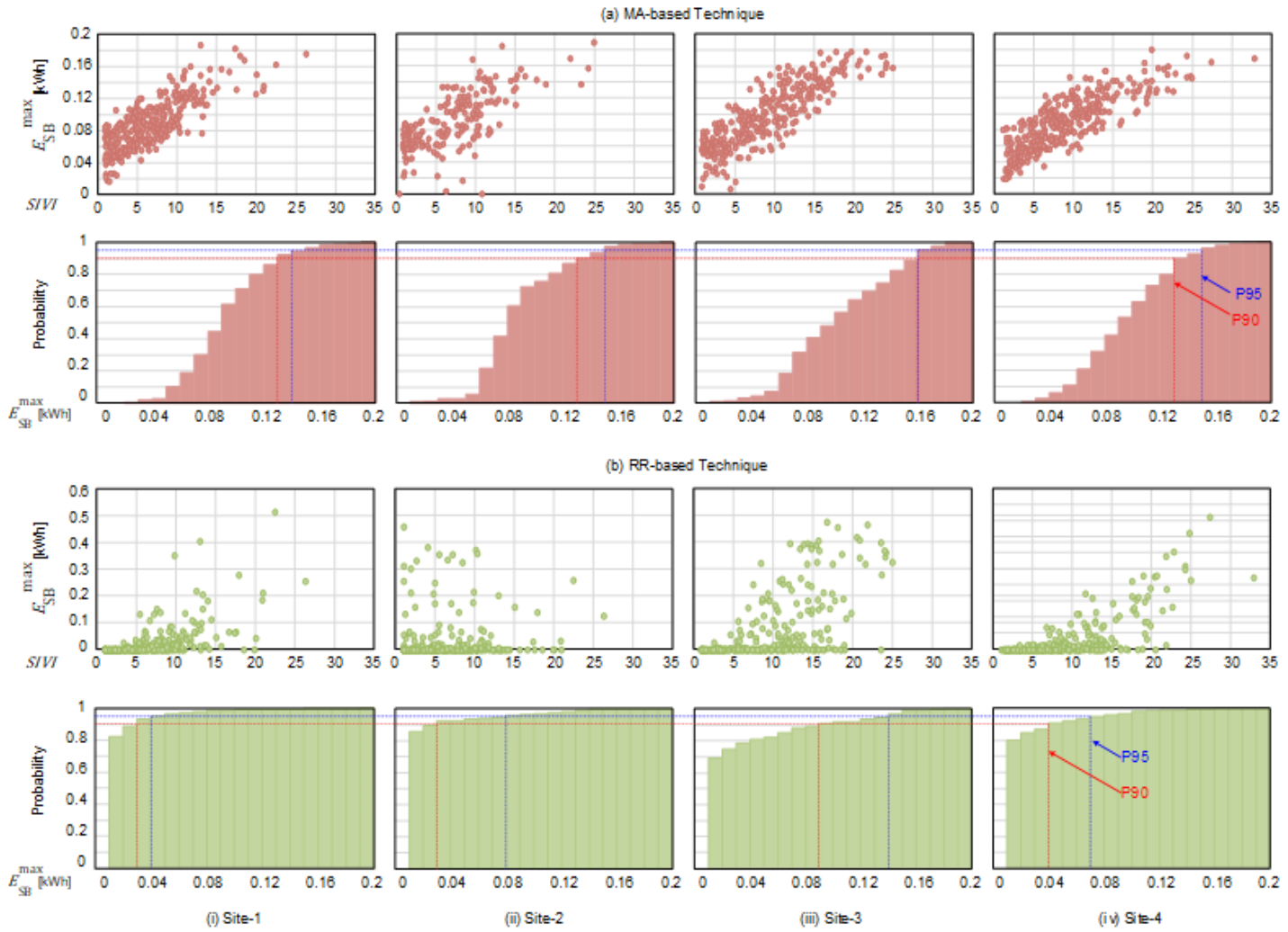

Figure 6.3. Smoothing battery optimisation results (scatter plot of the SBOC versus SIVI and their CDF) using the detailed model with P90 or P95 criterion at site-1 to 4 of Table 3.1 while employing (a) the moving average-based technique with a 10-min window, (b) the ramp rate-based technique with a 5% limit

Table 6.3. The Pearson correlation coefficient between the determined SBOC and the SIVI for the considered sites in Table 3.1

Site no.	Moving Average (10 min)	Ramp Rate limit (5%)
1	0.7786	0.5633
2	0.7348	0.5750
3	0.8577	0.5966
4	0.8180	0.6981
5	0.7724	0.6914
6	0.7755	0.5629
7	0.7302	0.4431
8	0.8294	0.6383
9	0.7521	0.4469
10	0.7849	0.4334
11	0.8149	0.4621
Average of all sites	0.7862	0.5556

Comparing the empirical CDFs for the moving average and ramp rate techniques, respectively given in Figure 6.3a and b, indicates that while the SBOC determined by the moving average technique appears symmetrically distributed, the ramp rate is positively skewed with the mode centred around zero. This makes intuitive sense as with ramp rate control, there are clear-sky days for more than 80% of the studied time (i.e., SIVI close to 1) where no smoothing is required; thus a smaller SBOC is needed. On the other hand, the diurnal nature of the sun results in the moving average algorithm to require energy exchange with the smoothing battery, even during clear sky days (provided that the moving average window is sufficiently large) [109]. This is in line with the finding of [60] which shows increased smoothing battery

cycling and degradation under the moving average technique relative to the ramp rate technique.

To understand why ramp rate control is less strongly correlated with SIVI, let us consider the single day simulations at site-5 for two different days of 20/11/2017 and 18/12/2017, illustrated respectively in Figure 6.4a and b. In the first day, the SIVI is 10.43 and Figure 6.4a shows a mainly clear-sky day with rapidly moving cloud bands occurring in the middle of the day and afternoon. In contrast, the SIVI in the second day is 23.04, and Figure 6.4b shows a highly variable mixed-sky day with solar irradiance fluctuations occurring consistently throughout the day. However, the SBOC for the relatively low SIVI at the mainly clear-sky day of Figure 6.4a is 0.2837 kWh/kWp, while it is almost 10 times lower (0.029 kWh/kWp) for the high SIVI in the mixed-sky day of Figure 6.4b which is in contrary to what is expected.

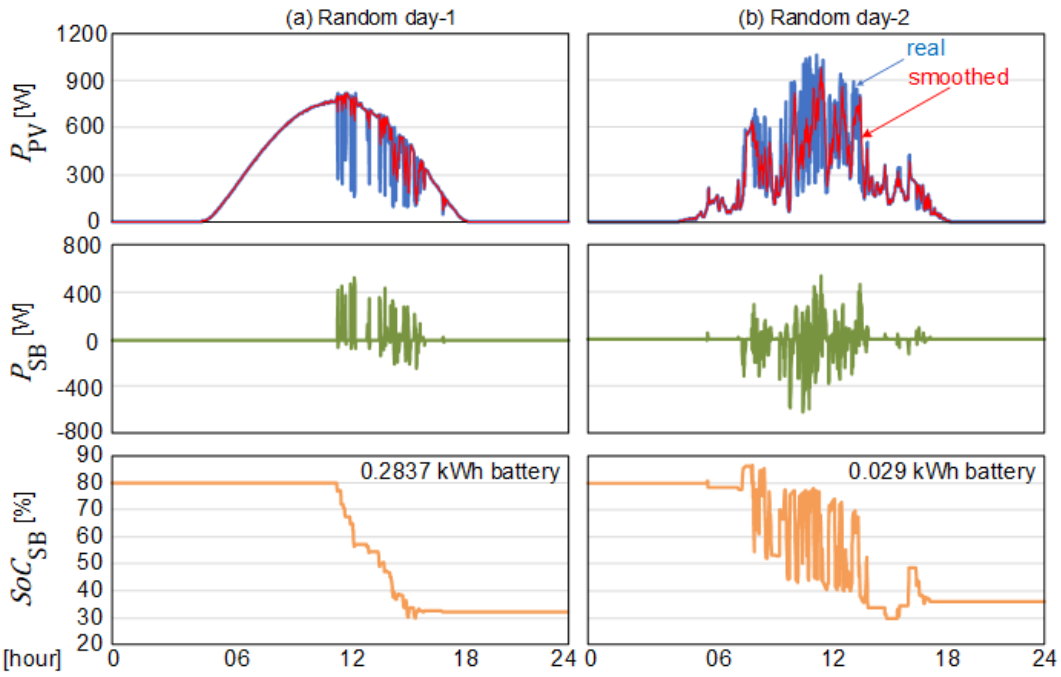

Figure 6.4. Performance of the microgrid when using a smoothing battery, defined under the ramp rate technique with 10% limit at site-5 on two random days of (a) 20/11/2017, (b) 18/12/2017

The difference between the two days is the number of upward and downward ramps. The day with a relatively low SIVI has mainly downward ramps; thus, requiring the smoothing battery to discharge for most of the day. On the other hand, the day with a high SIVI has more symmetrical distribution of upward and downward ramps, allowing the smoothing battery to both charge and discharge throughout the day. Therefore, for the ramp rate technique, the direction of ramping events is a key factor for sizing the smoothing battery. The SIVI provides a crude proxy for the amount of ramping that will be observed since a day with a high SIVI is more likely to exhibit asymmetrical ramping events requiring higher SBOC. However, the outliers in these two figures show that this is not always the case.

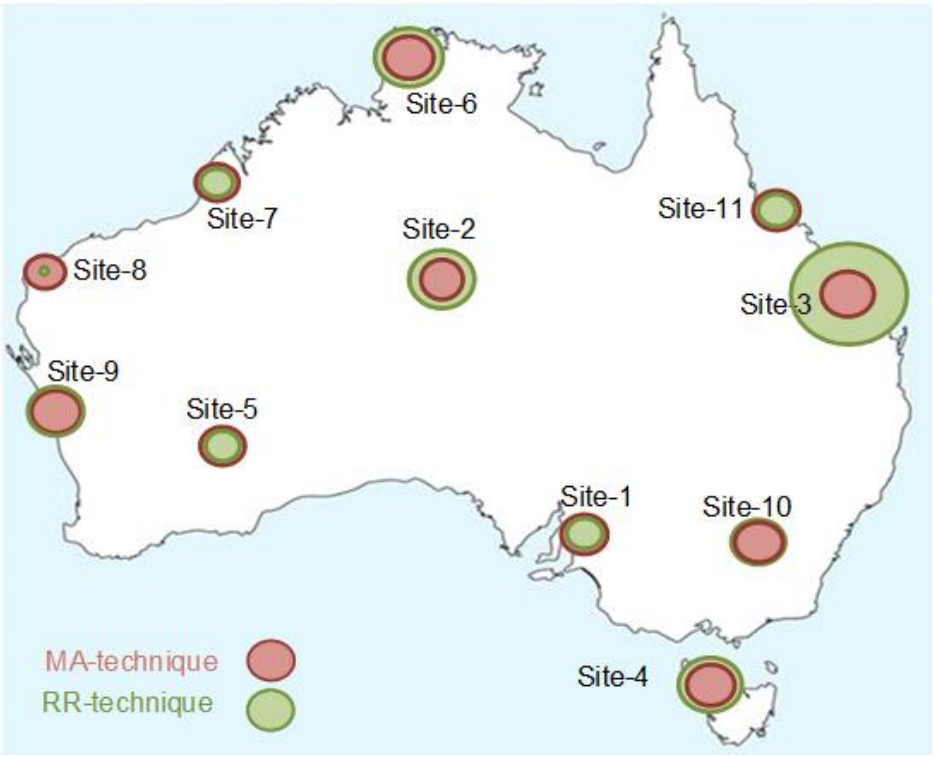

Figure 6.5. Comparison of the detailed model based determined SBOC using a 10-min moving average and 5% ramp rate techniques for the 11 study sites considered in Table 3.1

Figure 6.5 demonstrates the SBOC selected for P95 PONE at the 11 study sites of Table 3.1, using the moving average and ramp rate-based techniques. This figure

illustrates the results using the detailed model while Table 6.4 lists the results from the detailed model, as well as the proposed approximate model, using the linear regression and the observed SIVI, and their difference. The results support the previous observation that moving average is strongly correlated with SIVI. The approximate method is inherently conservative because it adds the standard error to the linear regression and the results in Table 6.4 show a fairly consistent positive deviation of around 10 to 20%. On the other hand, the large positive and negative deviations found in the results for the ramp rate technique indicate that the approximate method does not accurately predict the SBOC.

Table 6.4. Comparison of the determined SBOC by the detailed and proposed approximate models and their difference, using the P95 desired level for all considered sites in Table 3.1 under the 10-min moving average and 5% ramp rate techniques

Site no.	Moving Average (10-min)			Ramp Rate Limit (5%)		
Model	Detailed [kWh/kWp]	Approximate [kWh/kWp]	Deviation [%]	Detailed [kWh/kWp]	Approximate [kWh/kWp]	Deviation [%]
1	0.140	0.150	7.1	0.111	0.149	34.2
2	0.142	0.152	7.0	0.212	0.152	– 28.3
3	0.159	0.175	10.1	0.362	0.188	– 48.1
4	0.144	0.179	24.3	0.198	0.194	– 2.0
5	0.136	0.163	19.9	0.109	0.168	54.1
6	0.150	0.167	11.3	0.214	0.176	– 17.8
7	0.130	0.152	16.9	0.100	0.151	51.0
8	0.123	0.140	13.8	0.019	0.132	594.7
9	0.151	0.177	17.2	0.174	0.192	10.3
10	0.144	0.165	14.6	0.166	0.173	4.2
11	0.140	0.154	10.0	0.118	0.155	31.4

Figure 6.6a and b show the linear regression using the moving average and ramp rate techniques and with data from all sites that have been used in the study. The regression coefficients for the moving average and ramp rate algorithms, used in (7), are provided in Table 6.5. It is to be noted that these coefficients are based on model parameters used in this study (i.e., the smoothing battery's type, chemistry and DoD, the PV parameters, etc.) and may not be accurate if these parameters are changed.

Table 6.5. Coefficients for the suggested approximate method used in the SBOC's calculation

Technique	α	β	σ
Moving average with 10-min window	0.0046	0.0567	0.0315
Ramp rate with 5% ramp limit	0.0074	-0.0221	0.0709

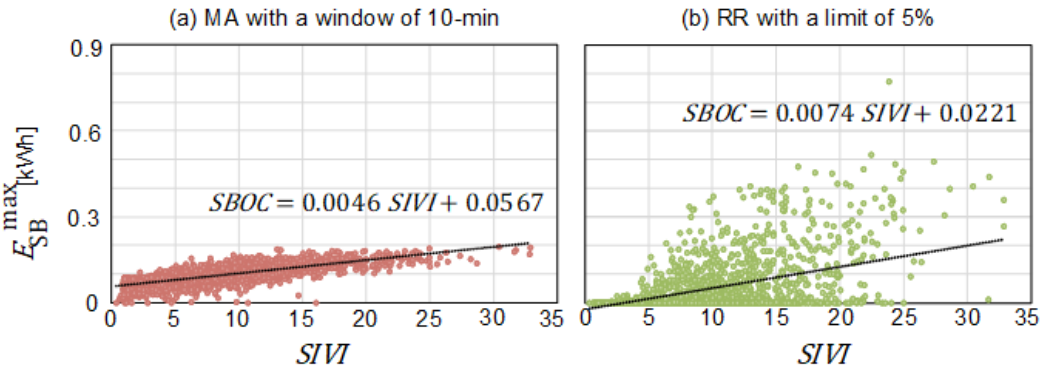

Figure 6.6. Linear regression results for all sites using a) moving average-based technique with a 10-min window and b) ramp rate-based technique with a limit of 5% of the nominal rating per minute.

6.2 **Comparative Analysis**

To illustrate the superior performance of the proposed technique versus existing similar techniques, the detailed model described in this study is compared against two SBOC sizing approaches that are commonly found in the literature.

The first method is the peak energy exchange method [64-66]. In this method, the energy exchanged between the smoothing battery and the microgrid is integrated over an entire day (allowing for recharging at night), and the maximum value denotes the peak energy exchange for the day.

This process is repeated for each day of the year, and the maximum value of the year is selected as the SBOC. The second common method is the hourly chronological simulation method [62-63]. This method is structurally similar to the detailed method used in this study with the key differences being that the sampling resolution is hourly, and the smoothing battery is sized to have sufficient capacity for the entire year (i.e., there is no nightly recharging).

The above smoothing battery sizing methods are implemented for site-1 using the moving average technique with a 10-min window. To facilitate a fair comparison between methods, a maximum allowed DoD of 70% and initial SoC of 80% is applied and nightly recharging is assumed. The results of the comparison are presented in Table 6.6, showing the SBOC and the implied coverage over the full year, i.e., coverage of 95% means that the smoothing battery is sufficiently sized for 95% of the year (347 days). The proposed methods (both detailed and approximate) yield similar SBOC values to the peak energy ex-change method, although the SBOC from the peak energy ex-change method has lower coverage as this method does not con-sider the smoothing battery's efficiencies or charge/discharge characteristics. Note also that the coverage in the proposed methods is a selected de-sired value and can be modified based on the smoothing battery's design criteria. As can be expected, the hourly chronological simulation method yields a significantly larger SBOC than the other methods, due to the effect of the course 1-hour sampling, resolution filtering out short-term variations in solar irradiance.

Table 6.6. Comparison of SBOC sizing methods for site-1 using the moving average-based technique with a 10-min window

	SBOC sizing method	SBOC [kWh/kWp]	Annual Coverage [%]
Existing methods	Peak energy exchange	0.131	92.8
	Hourly chronological simulation	0.619	100.0
Proposed method	Detailed method (P95 desired level)	0.140	95.0
	Approximate method (P95 desired level)	0.150	96.5

6.3 **Sensitivity Analysis**

A sensitivity analysis is carried out to evaluate the variations in the determined SBOC against the key assumptions in the studies; i.e., the window size of the moving average technique, the limit of the ramp rate technique, as well as the smoothing battery's maximum allowed DoD and the desired initial SoC. The results of these studies are presented in Figure 6.7a to d, respectively while in each of the sensitivity analyses, all other key parameters are assumed fixed as per Section 6.1.

6.3.1.1 **Window Size of the Moving Average Technique**

As seen in Figure 6.7a, as expected, the SBOC increases as the moving average window size is expanded from 5 to 20 minutes, with roughly a threefold increase. There is also an increase in the dispersion of the SBOC as the window size is expanded, with $\sigma = 0.0191$ for a 5-minute window and $\sigma = 0.0494$ for a 20-minute window.

6.3.1.2 **Ramp Rate Limit of the Ramp Rate Technique**

As shown in Figure 6.7b, the SBOC increases as the ramp rate limit decreases from 15 to 1% of the nominal rating per minute. As an example, an average SBOC of

0.0024 kWh/kWp is observed for a 15% ramp rate limit while an average SBOC of 0.0615 kWh/kWp is seen for a 1% ramp rate limit. Similar to the window size of the moving average technique, there is an increase in the dispersion of the SBOC as the limit of the ramp rate technique is tightened, with $\sigma = 0.0102$ for a 15% limit and $\sigma = 0.1311$ for a 1% limit.

6.3.1.3 **Smoothing Battery's Maximum Allowed DoD**

As illustrated by Figure 6.7c, the SBOC increases as its maximum allowed DoD decreases from 80 to 50%. At an allowed DoD of 80%, the mean SBOC is 0.0564 kWh/kWp while it increases to 0.1254 kWh/kWp for a DoD of 50%.

6.3.1.4 **Smoothing Battery's Initial SoC**

As seen in Figure 6.7d, the SBOC increases as the smoothing battery's expected initial SoC decreases from 90 to 60%; however, the impacts are relatively small, e.g., the mean SBOC is 0.0822 kWh/kWp for an initial SoC of 90% which slightly increases to 0.0949 kWh/kWp for an initial SoC of 60%. As such, through the above sensitivity analyses, it can be seen that the SBOC is largely invariant to the initial SoC and a value of 70-80% is suggested to provide sufficient headroom for the smoothing battery's charging and discharging. The sensitivity analyses also show that the maximum allowed DoD has a moderate impact on the SBOC and it is recommended that it is set above 60%, although cycle-life considerations should also be taken into account.

The sensitivity analyses also showed that ramp rate becomes less correlated with SIVI as the ramp rate limit increases, e.g., r = 0.5927 for a ramp rate limit of 1%, and r = 0.43587 for ramp rate limit of 15%. This is because a day with a high SIVI can have many small fluctuations that do not exceed the ramp rate limit, thus the smoothing battery does not need to be called into action.

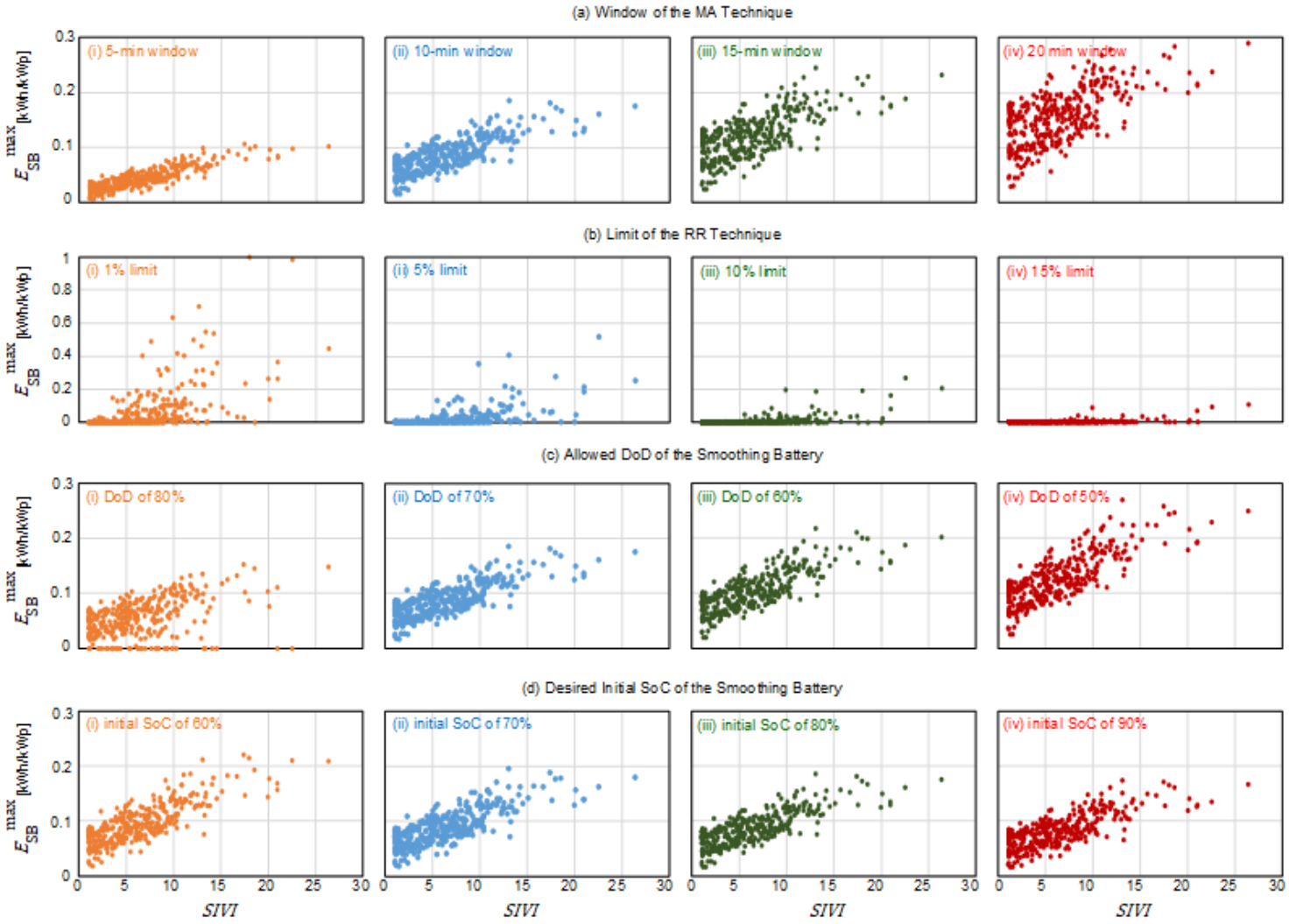

Figure 6.7. Sensitivity of the determined SBOC to the (a) the moving average window size for a window (between 5 and 20 minutes), (b) the ramp rate limit (between 1 and 15%), (c) a maximum allowed DoD of 80 to 50% for the smoothing battery, (d) an initial SoC of 60 to 90% for the smoothing battery, versus the observed SIVI

6.4 **Practical Considerations and Limitations**

This study uses solar irradiance data with a 1-min resolution to capture the short-term temporal SIVI in the output power of the PV. A question that arises is whether a 1-min resolution adequately covers the range of temporal fluctuations in solar irradiance. For example, [141] reports variations of above 50% in 1-second for a 48 kWp solar PV system. However, the empirical probability of such variations was found to be 0.000235% (or roughly 2 hours in a year). Ref. [141] also reports that variations of less than 10% in 1-second represent 99.86% of all observations. For 1-min resolutions, variations of less than 10% represent 95.11% of all observations. Based on these findings, it is proposed that 1-min resolution data be considered as the minimum resolution while below 1-min resolutions may be used for higher coverage.

It is worth noting that the Bureau of Meteorology's weather stations are single measurement points and any natural smoothing effects due to spatial diversity [75] are ignored in this study. For small centralised microgrid systems, the absence of spatial smoothing is unlikely to have any significant impact on the results; however, the ignoring the spatial smoothing for larger PVs or distributed systems will lead to more conservative (less optimal) results.

Furthermore, this study suggests employing at least one year of solar irradiance data when determining the SBOC to cover seasonal variations. However, it may be more prudent to use multi-year data to capture longer-term (inter-year) variations, such as natural climate cycles, e.g., El Niño and La Niña events. Yet, in practice, this may be contingent on the availability and/or project economics of collecting longer-term data.

6.5 **Summary**

This chapter has focused on deriving a correlation between the SBOC and the SIVI, based on the two most commonly used smoothing techniques of moving average and ramp rate control. The studies were based on a real large solar irradiance dataset with a 1-minute resolution for a full calendar year and across 11 locations.

The studies show that the calculated SBOC under the moving average technique is quite strongly correlated with the daily SIVI, and this observation can be used to develop relatively accurate empirical estimates for the SBOC, which is solely based on the SIVI.

A comparison with other SBOC sizing methods indicates that the proposed method is comparable to the peak energy exchange method, but has greater flexibility since the level of coverage is an input variable for the smoothing battery's sizing algorithm. The main advantage of the proposed approximate method is that the system planner or designer does not need high-resolution irradiance data at the specific site location but can use an estimate of the SIVI or the SIVI measured at a nearby location. This is because, in principle, the linear regression (in Table 6.5) is applicable to any arbitrary site, provided that an estimate of the SIVI is known.

Sensitivity analyses also show that the SBOC is not significantly influenced by the smoothing battery's initial SoC and maximum allowed DoD. The results of this study also indicate that the determined SBOC by the ramp rate control technique is weakly correlated with the SIVI, and as a result, the approximate empirical method using the ramp rate control technique-based linear regressions has limited accuracy.

Chapter 7 PV Integration into Weak Grids

A framework for integrating solar PV into weak grids was proposed in Section 3.4. In this chapter, five case studies are presented as examples from actual project developments in Indonesia, Philippines and Bangladesh. The case studies have been selected to cover both successful and abandoned developments and serve to illustrate how the proposed framework is applied in practice. Table 7.1 lists these projects and the issues addressed in each case study.

7.1 Case Study 1: Lampung, Indonesia

The Krui project in Lampung province, Indonesia, was a 4 MWp PV plant development. The grid connection studies were performed for this project after completing the initial site surveys and data collection. The preliminary network analysis revealed that the nearest connection point of the PV plant was near the end of a 191 km radial 20 kV distribution feeder (see Figure 7.1). There was no generation or reactive power support on the feeder and the fault level at the connection point was estimated to be 10.5 MVA through short-circuit studies. For a 4 MWp PV plant, the SCR was estimated to be 2.625, thus making it a weak high-impedance connection point.

Table 7.1. Key issues addressed in the practical case studies

Key issue	Case 1	Case 2	Case 3	Case 4	Case 5
Issues associated with weak high-impedance connection points					
Voltage regulation and stability	✓	✓	✓		
Line thermal ratings	✓				
Power losses		✓			
Connection point reliability					✓
Issues associated with weak low inertia connection points					
Frequency stability				✓	✓
Generator dispatch and loading				✓	

Figure 7.1. A PV plant considered to be connected to a weak grid in Lampung, Indonesia

Figure 7.2 shows the voltage profile along the distribution feeder with the PV plant connected near the end of the feeder. With the PV plant operating under voltage control mode, the studies demonstrate that the PV plant is able to effectively manage the steady-state voltage profile at the end of the feeder. However, since the feeder

voltage is supported at each end, a voltage sag is observed near the feeder's midpoint, and in this case, the midpoint voltage falls under the steady-state limit of 0.9 pu.

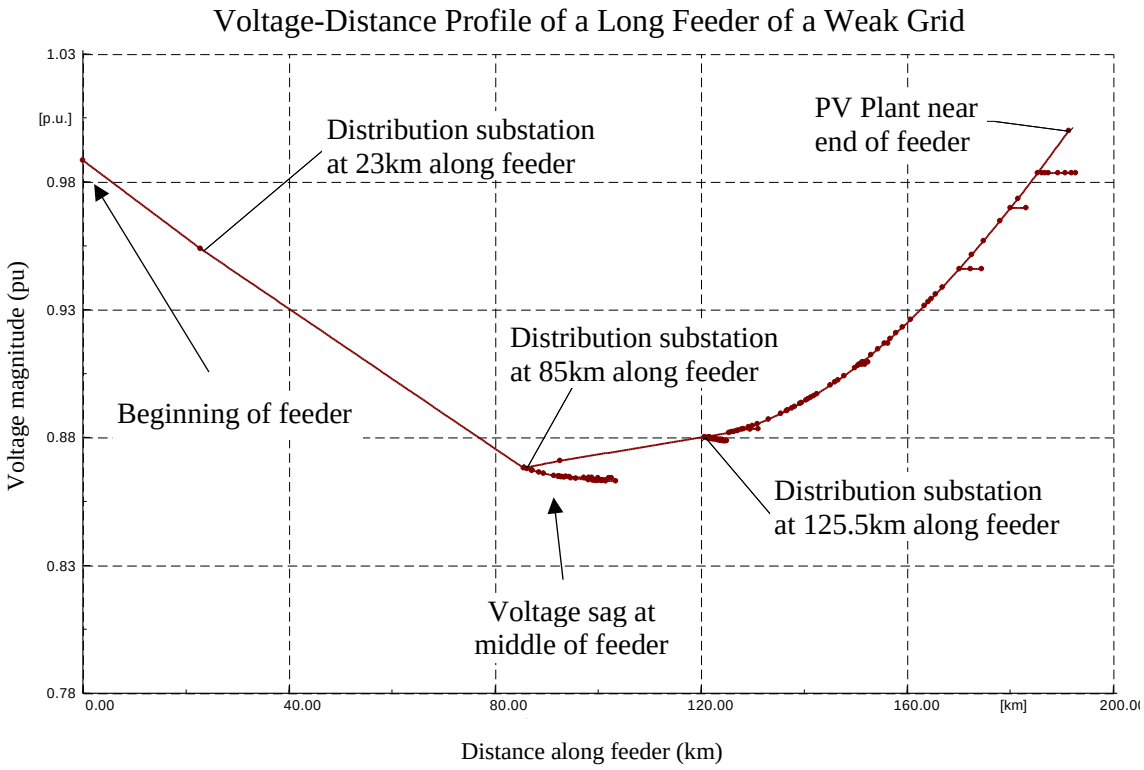

Figure 7.2. Voltage-distance plot of a long feeder of a weak grid accommodating a PV plant operating under voltage control mode at the end of the feeder

Figure 7.3 shows a pair of Q-V curves for the distribution network with and without the PV plant connected to the system. It can be seen from this figure that without the PV plant, the system operates near the point of voltage collapse, with a reactive power margin close to zero. This simulated finding agreed with the actual historical data from the utility, which indicated that the feeder had a track record of frequent voltage collapses. With the PV plant connected, the studies demonstrated that the reactive power margin can improve to 425 kVAr. However, the network voltage at the connection point (i.e., a very stressed system) is actually outside the allowable voltage range of normally available PV inverters.

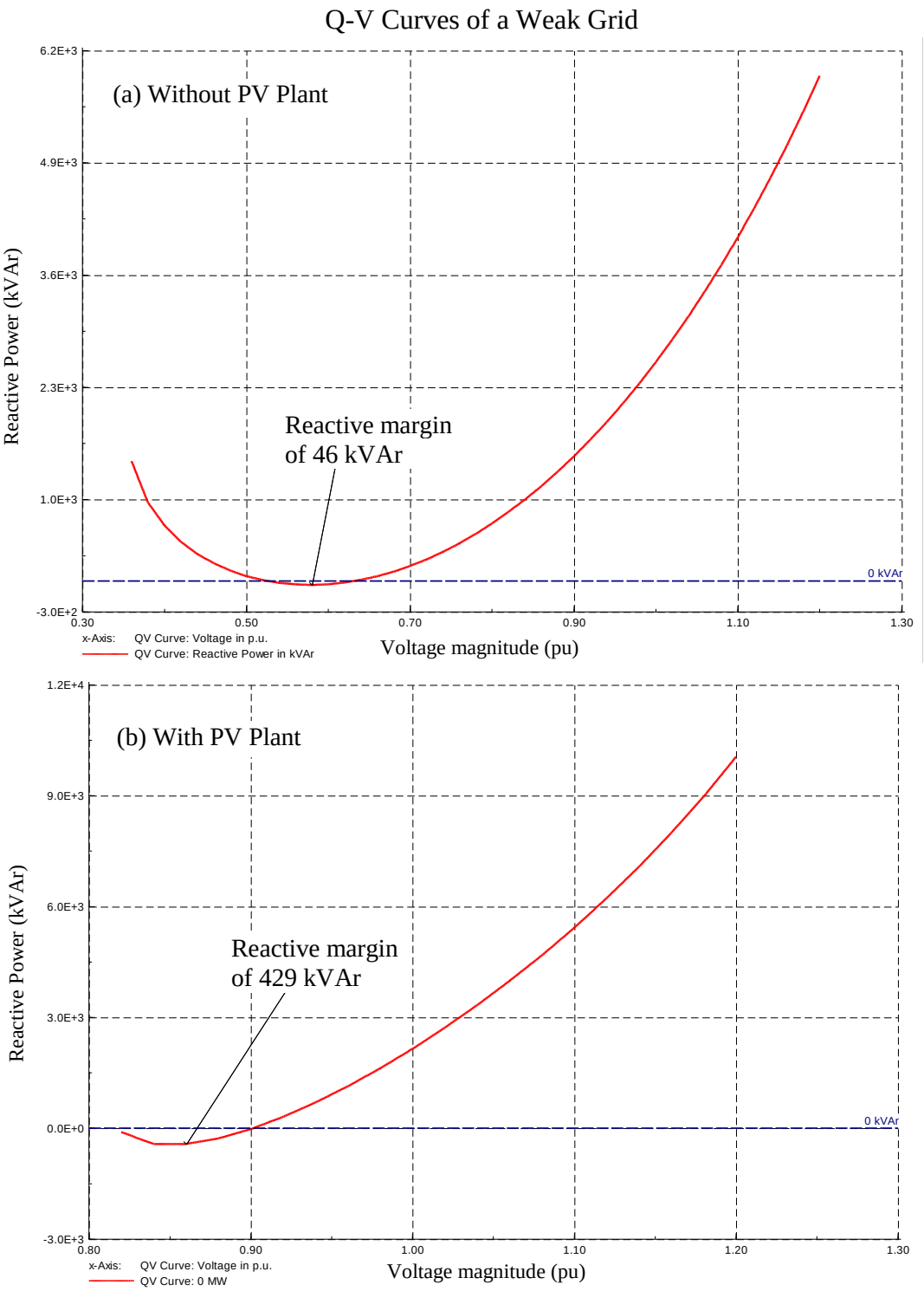

Figure 7.3. Q-V curves for a weak grid with and without a PV plant, showing the effect of the PV plant on reactive margin at the end of a long feeder

Furthermore, approximately halfway along the distribution feeder, the size of the overhead line conductors was reduced commensurate with the declining load on the

feeder. It was found that the thermal rating of the reduced conductors was not high enough to accommodate the full capacity of a 4 MWp PV plant and needed to be upgraded.

The grid connection studies identified a number of critical issues arising from a weak high-impedance connection point. The cost of resolving these issues was deemed economically unfeasible, and the PV plant development was abandoned as a result.

7.2 **Case Study 2: Kishoreganj, Bangladesh**

The Mirzapur project in Kishoreganj district, Bangladesh, is a 25 MWp PV plant development. It was decided that the PV plant would be connected to the upstream network via a 14.3 km, 33kV overhead line. The studies on this project demonstrated that a PV plant could cause high active power losses in the weak grid to which it is connected despite providing valuable ancillary services such as voltage support.

Figure 7.4 illustrates the use of this PV plant to provide reactive power compensation and voltage control. This figure shows the 24-hour voltage profiles at the three substations closest to the PV plant for the cases with and without the PV plant. From this figure, it can be seen that the PV plant facilitates a more stable voltage profile throughout the day and night in its nearby buses.

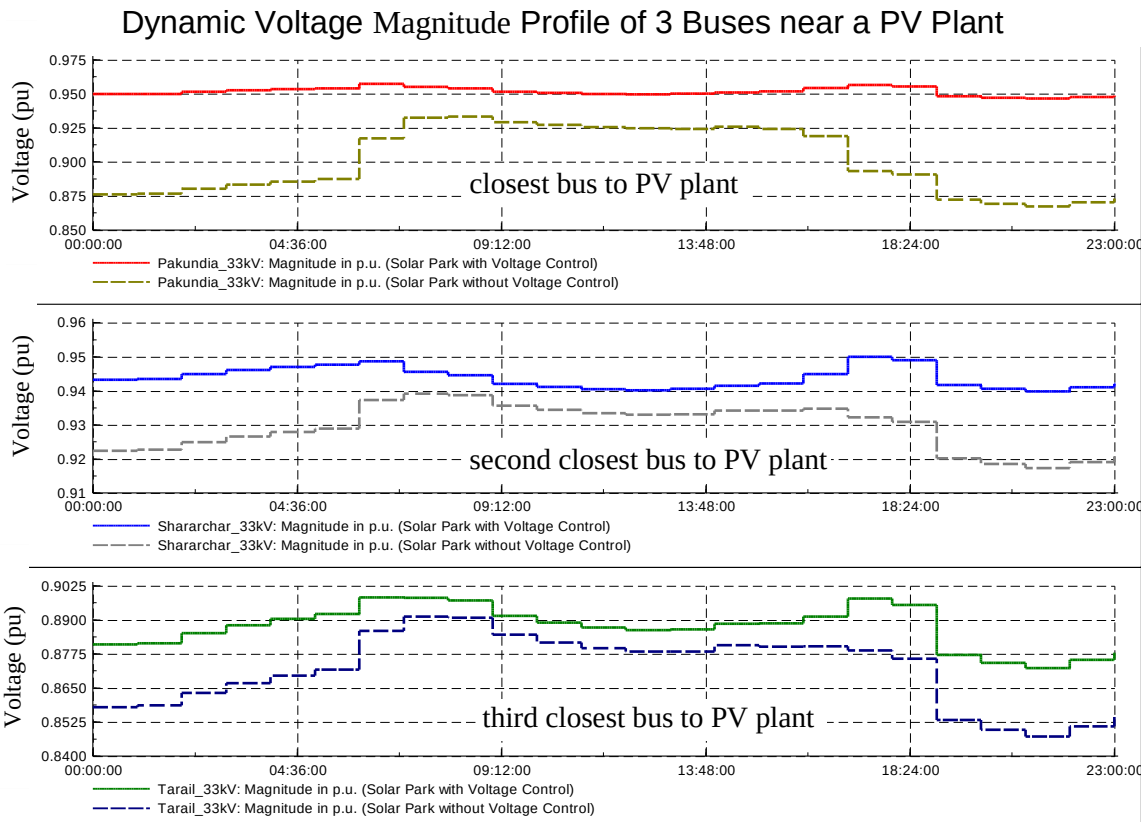

Figure 7.4. Comparison of voltage magnitude profile at three nearby buses of a weak grid accommodating a PV plant operating under normal and voltage control modes of operation

On the other hand, Figure 7.5 shows the results of the active power loss calculations over a 24-hr period in the Kishoreganj power distribution system. As can be seen from the figure, the PV plant produces more power than is required at the local (nearby) loads during peak sunlight hours. Therefore, the excess active power from the PV plant flows upstream along radial feeders to other substations before being reticulated to other feeders/loads. This leads to an increase in losses during the day. However, when the output of the PV plant is low (e.g., in the morning or late afternoon), most of the generated power can be consumed locally, and there is a corresponding reduction in the network losses.

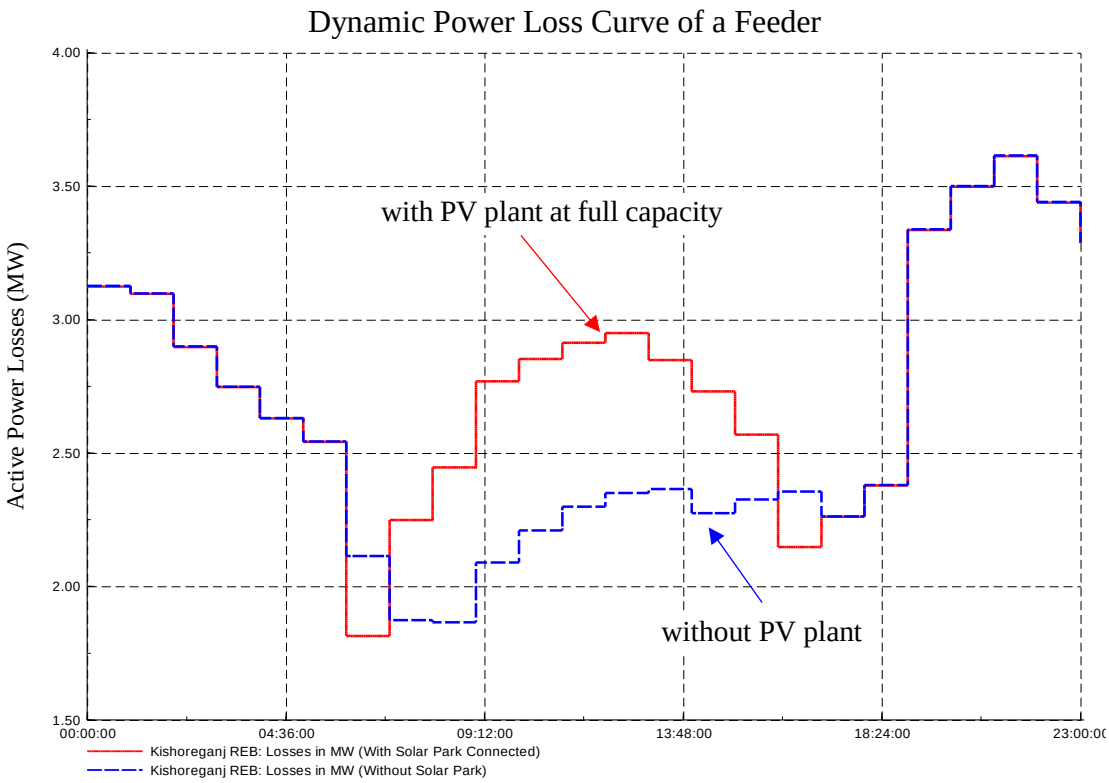

Figure 7.5. Comparison of the dynamic power losses in a feeder of a weak grid with and without a PV plant, showing increased power losses due to the upstream flow of the generated power from PV plant

7.3 **Case Study 3: Tarlac, Philippines**

The Dalayap project is an operating 7.48 MWp PV plant located near Tarlac City, Philippines. The PV plant is connected to the distribution grid via a tee connection into an existing 6 km, 13.8 kV feeder. This case study illustrates the sensitivity of a weak grid's voltage to daily PV plant fluctuations. Figure 7.6 shows four days of grid voltage measurements (at 5-minute resolution) with the PV plant connected and operating without any reactive power support functionality enabled. The plot in Figure 7.6a shows a prominent undulation in grid voltage that is highly correlated with the PV plant output, i.e., voltage rises during the day and falls at night. This is an example of a distribution network with a low X/R ratio, which exhibits higher coupling between active power and voltage. The voltage swings between day

and night would have been even higher were it not for manual tap changer action by the network operator at the upstream 69/13.8 kV substation to manage grid voltages. Figure 7.6b and Figure 7.6c show how the reactive power control features of a PV plant can be used to manage grid voltages in weak grids better while Figure 7.6d shows that with the PV plant operating in reactive power support mode, the PV plant absorbs reactive power during the day and helps control grid voltages without manual tap changing by the network operator. The effects can be seen in Figure 7.6b, where there is no noticeable day and night voltage swings.

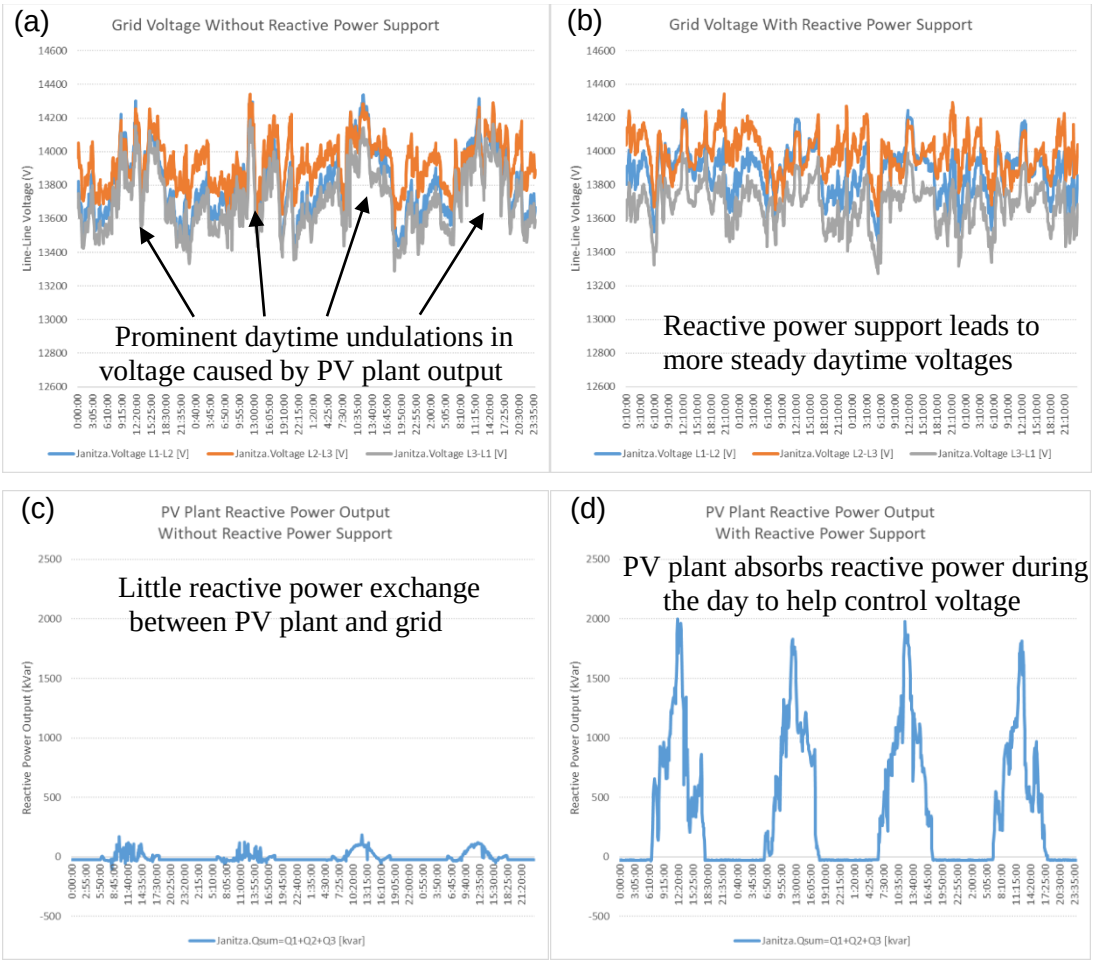

Figure 7.6. Use of a PV plant's reactive power support functionality to regulate grid voltages in weak grids

7.4 **Case Study 4: Nusa Tenggara Barat, Indonesia**

The Lombok project is a planned 5 MWp PV plant to be constructed in Nusa Tenggara Barat province, Indonesia. The original proposal was a PV plant of 10 MWp; however, it was evolved and reduced to 5 MWp based on the results of the grid connection study and negotiations with the network operator. The PV plant will be connected to the nearest substation via a 3 km, 20kV overhead line. The upstream network is an island power system with approximately 300 MW of installed generation capacity, most of which is composed of diesel generators. Based on empirical observations by the network operator, the stiffness of the system was estimated to be approximately 11 MW/Hz. For a 5 MWp PV plant, the SR was estimated to be 1.6, thus making it a weak low-inertia connection point.

Generators Dispatch Daily Profile in a Distribution System Accommodating a PV Plant

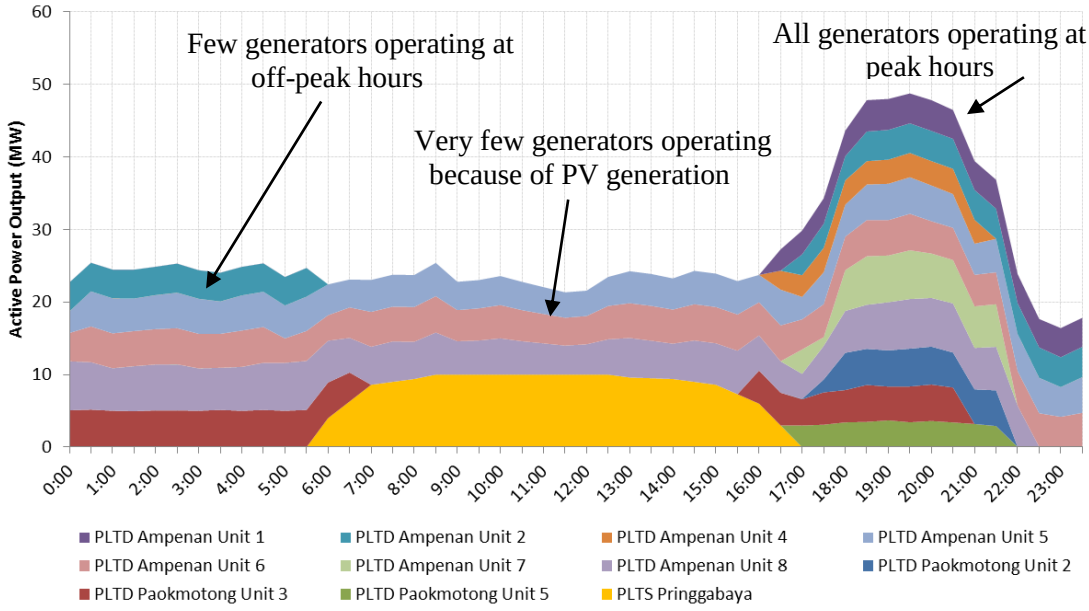

Figure 7.7. Variations of the output power of some generators following a power generation increase from a PV plant at day times

Figure 7.7 shows a 24-hour generator dispatch profile with an ideal PV plant output over a typical day and illustrates how the 10 MWp PV plant was expected to displace diesel generation during the day while maintaining a minimum output of 70% for the dispatched machines. It can be seen that when the PV plant is generating at full capacity, two conventional generators can be switched off during the day while the other machines can still operate above 70% of their capacity.

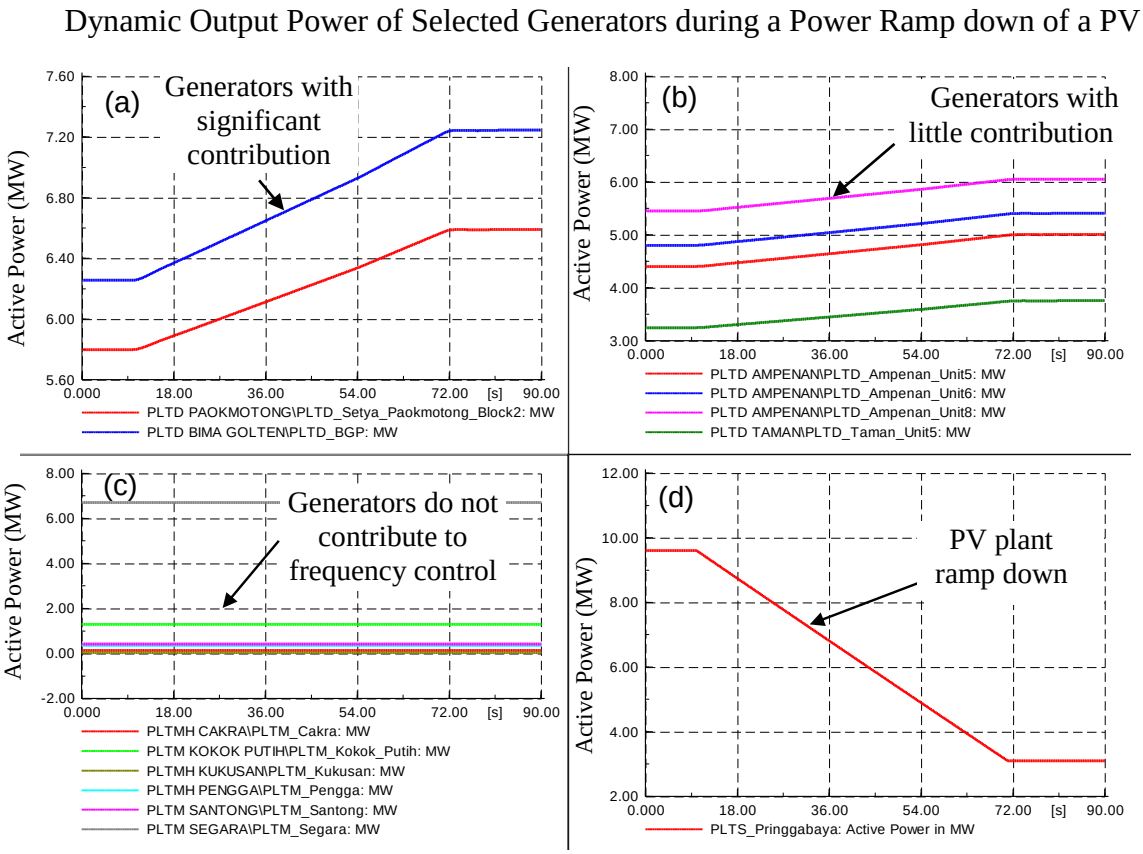

Figure 7.8. Output power variations of selected generators in a distribution system following an extreme ramp down of the output power from a PV plant

Figure 7.8 shows the dynamic response of the conventional generators in this system during an extreme ramp down event where the output power of the PV plant decreases by 70% within one minute. It can be seen from the figure that there are some generators in the system that operate at fixed output powers and do not contribute to primary frequency control. It is crucial to identify these generators as assuming that

all machines operate with droop-controlled governors can lead to overly optimistic simulation results. At this stage, the grid connection studies for a 10 MWp PV plant had satisfied the network operator's requirements.

Frequency Response of a Weak Grid Hosting a PV Plant with Various Capacities

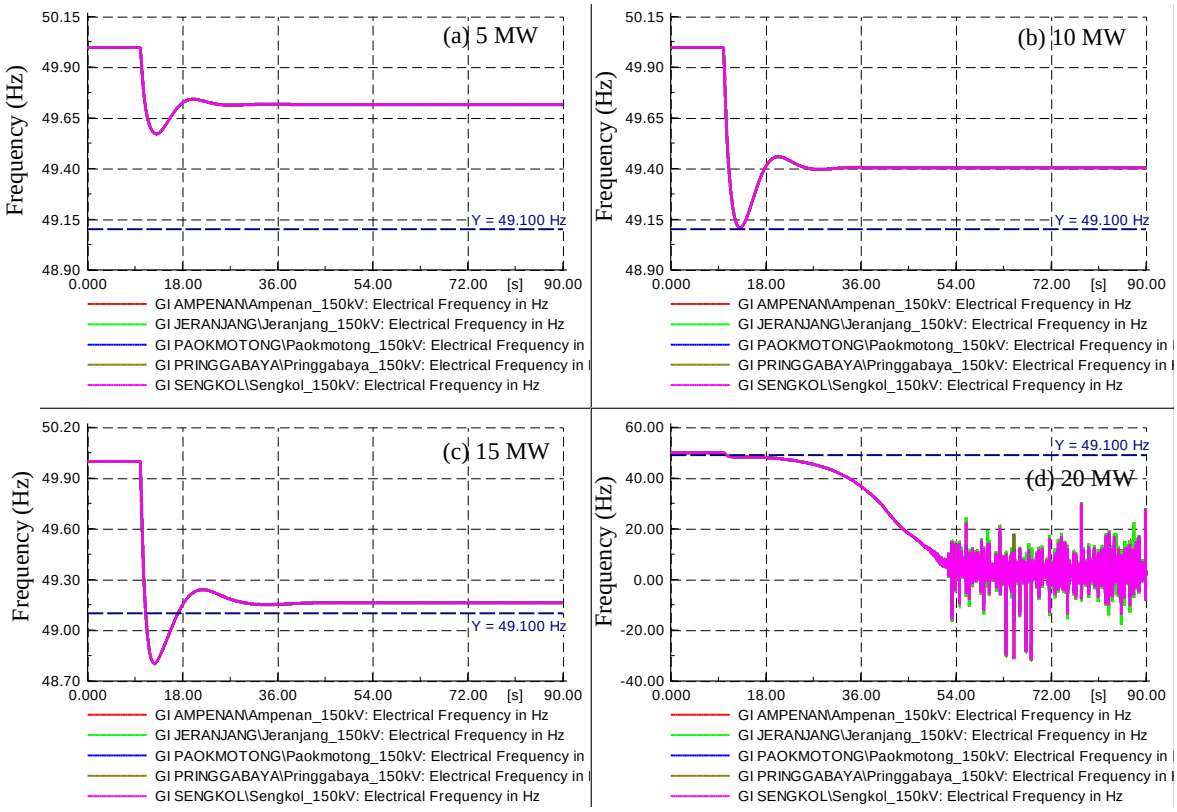

Figure 7.9. Stable and unstable frequency responses of a distribution system accommodating a PV plant with various capacities following the loss of the PV plant

However, the maximum capacity of the PV plant was reduced to 5 MWp based on the frequency stability analysis shown in Figure 7.9. From this figure, it can be seen that for the loss of a 5 MWp PV plant event, the system will reach a frequency nadir of 49.57 Hz shortly after the event, and then settle at a steady-state value of 49.72 Hz after 30 seconds. In the case of a 10 MWp PV plant, the frequency nadir is 49.12 Hz. In both cases, the frequency is above the threshold of 49.1 Hz for the UFLS protective relays, and they are not tripped. In the case of a 15 MWp PV plant, the frequency drops

below this threshold and activates the UFLS protective relays. However, in the case of a 20 MWp PV plant, the same disturbance leads to frequency instability and system collapse. Based on these results, the network operator was uncomfortable with the response of the 10 MWp PV plant, where the frequency nadir was very close to the UFLS threshold, and as a result, the PV plant's maximum capacity was reduced to 5 MWp.

7.5 Case Study 5: Sulawesi Tenggara, Indonesia

The Bau Bau project in Sulawesi Tenggara province, Indonesia was a 6 MWp PV plant development. The PV plant was intended to be built in a rural area, approximately 20 km from the nearest substation. A 20 kV distribution feeder ran within 1 km of the PV plant location, and a tee connection was proposed to this line. However, during consultation with the network operator, it was found that the 20 kV feeder was susceptible to frequent earth faults, as many as one per day based on the records from the previous three years. The grid connection studies also showed that a complete PV plant trip would trigger the UFLS scheme. This was unacceptable to the network operator, and the project was required to reduce the proposed PV plant capacity to 1.5 MWp and build a dedicated 20 km overhead line to the substation. These provisions made the project economically unfeasible and the project development was ultimately abandoned.

7.6 Summary

This chapter presented a structured technical framework for analysing the connection of PV plants to weak grids, giving due consideration to the specific issues arising from weak grid connections. The proposed framework was used successfully

on several PV plant developments in Southeast and South Asia, as illustrated in the practical case studies. This study showed that in many cases, a standard steady-state/load flow analysis is not adequate to determine the maximum penetration level of a PV plant connected to a weak grid and will yield overly optimistic results that can lead to serious stability problems during operation. The proposed framework suggests the detailed studies that are required to specifically investigate voltage and/or frequency stability issues.

The main contributions of this framework to the research field are twofold: 1) the development of metrics to systematically identify and classify weak points within the distribution networks of remote areas and islands, and 2) the development of a structured process to be used by the distribution network operators at the decision-making process for approving PV plant connection to the networks in remote areas and islands and the possible mitigation techniques when technical criteria are not met.

Finally, it should be highlighted that the development of PV plants is primarily a commercial activity where project bankability is one of the most important factors for whether a project materialises. Many recommendations for mitigating grid instability risks (e.g., synchronous condensers, static compensators, flywheels, etc.) are technically feasible, but may not be economically practical. Therefore, the main challenge for the PV plant developer is to work together with network operators to ensure that system security (stability, reliability, and integrity) is maintained, while keeping the project economically viable.

Chapter 8 Estimating Load Relief for Frequency Stability Studies in Weak Grids

In this chapter, the system LRF estimation method proposed in Section 3.5 is tested on real contingency event data from the Southwest Interconnected System (SWIS) in Western Australia.

The SWIS is a medium-scale islanded power system with a peak demand of 4,300 MW, but covering a vast geographic area of approximately 261,000 square kilometres (greater than the land area of the United Kingdom). The SWIS can be regarded as a moderately weak grid due to the influx of VRE into the system, particularly at distribution level from residential rooftop PV.

The SWIS has a fleet of fault recorders, installed at selected substations throughout the network, which are triggered on frequency contingencies above a pre-set threshold. Therefore, they provide high resolution (10 ms) visibility over all the major power stations in the system during disturbances. These fault recorders are used to accurately measure system frequency, aggregate system PFR (including interruptible loads that trigger at 49.5 Hz and 49.25 Hz) and the active power change from the contingency itself.

8.1 Contingency Test Cases

Three generator contingency test cases (shown in Table 8.1) are used to estimate the system LRFs using the method proposed in Section 3.5. Note that only generator contingencies are considered as the fault recordings can provide unambiguous measurements for the size of a generator contingency. For load contingencies, it is more difficult to assess the true size of the contingency, particularly when precipitated by transmission line faults within meshed networks. Moreover, determining the aggregate PFR is further complicated by the fact that the over-frequency responses of wind farms, solar farms and DERs (such as rooftop PV) are not directly measured by the fault recorders.

Table 8.1. Considered generator contingency cases

Parameter	Unit	Event-1	Event-2	Event-3
Contingency size	MW	198	197	200
Initial system load	MW	2,432	2,123	2,463
Post-contingent total system inertia	MW.s	21,521	17,100	17,361

The post-contingent total system inertia is estimated by re-arranging (3.53), which is considered to adequately express the relationship between RoCoF and inertia in the first few seconds immediately after a contingency [60-61]. This equation is sensitive to the value of the RoCoF that is used, which is typically calculated from taking the sample time derivative of the measured frequency trace. But the measured frequency trace is subject to transients, oscillations, quantisation errors and noise, and needs to be filtered before it can be used for calculations with inertial time scales. Following the approach taken by [60-62], the RoCoF is calculated by finding the maximum value of a sample-by-sample time derivative smoothed out by a 500-ms sliding window.

8.2 Substation Level LRF Estimation Results

Since there are high-speed fault recorders installed at most transmission substations in the SWIS, it is possible to obtain high resolution, time-synchronised load data at the substation level for a series of generator contingencies. Thus, LRFs can be estimated at the individual substation level using the frequency and voltage dependent load model described in Eq. (3.53).

The load relief and voltage dependency factor estimates for Event 1 are shown for a sample of substations in Table 8.2.

Table 8.2. Estimated substation level LRFs for Event 1

Substation	n_v	k_p
Balcatta	1.33045	0.96704
Bibra Lake	1.34870	0.11295
Binningup	0.35445	3.49955
Boddington	0.53563	2.96157
Boulder	0.81777	-0.61926
Bunbury	-1.44160	4.78739
Busselton	1.84820	0.07898
Clarkson	5.27341	1.49201
Cottesloe	1.38980	-0.64034
CSBP	0.00000	0.01202
East Perth	0.76622	-1.15828
Eneabba	1.15694	-0.90818
Hazelmere	0.79753	-0.32717
Joondalup	2.43768	1.12017
Karara	1.29406	2.96353
Kewdale	1.79136	-0.64879
Manjimup	0.56522	0.38851

Substation	n_v	k_p
Margaret River	1.12304	-1.50615
Mason Rd	1.21128	1.98074
Midland Junction	0.84419	-1.77776
Morley	1.39546	-0.34990
Muchea	0.72250	-0.52541
Murdoch	1.13751	-0.61145
Narrogin	-5.17798	-5.46074
Northam	2.23595	0.67988
North Perth	1.20334	-1.99055
Padbury	1.46786	-1.08759
Picton	1.39689	-0.26478
Pinjarra	0.57791	0.00107
Rivervale	0.27829	-1.05744
Shenton Park	1.16412	-0.89050
South Fremantle	0.95284	0.55585
Three Springs	1.23134	-0.29603

A selection of the substation load responses from the same event is shown in Figure 8.1, depicting examples from three different types of load responses: a) industrial, b) mixed-use commercial and residential, and c) rural.

It can be seen from the results in Table 8.2 that the substation level LRF estimates vary considerably across substations, as was found in [135] for sites in a different system in Australia (the National Electricity Market). As can be expected, industrial substations such as Binningup (desalination plant), Karara (iron ore mine), Boddington (gold mine) and Mason Rd (Kwinana industrial estate) have high load relief factors (ranging from 2 to 3.5), owing to the prevalence of induction motor use

at these sites. On the other hand, residential or mixed-use substations such as Balcatta, Bibra Lake, Cottesloe and Murdoch exhibit low or even negative load relief factors.

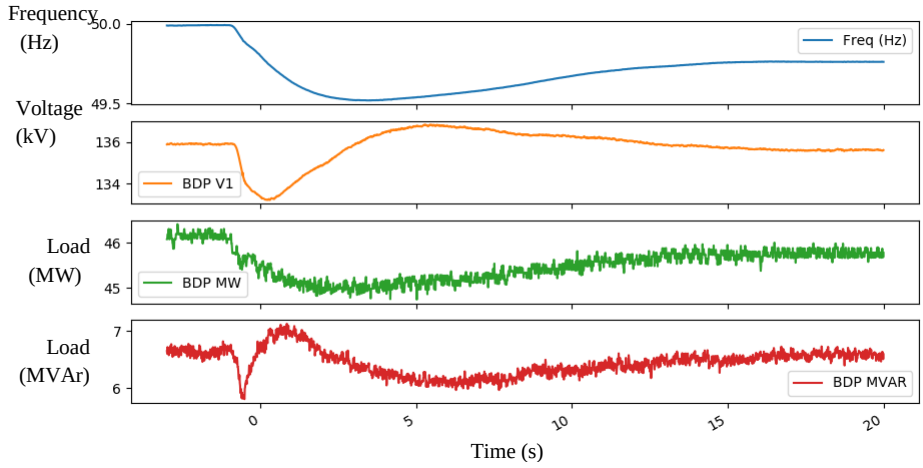

(a) Binningup Desalination Plant (BDP) – Industrial (k_p = 3.50)

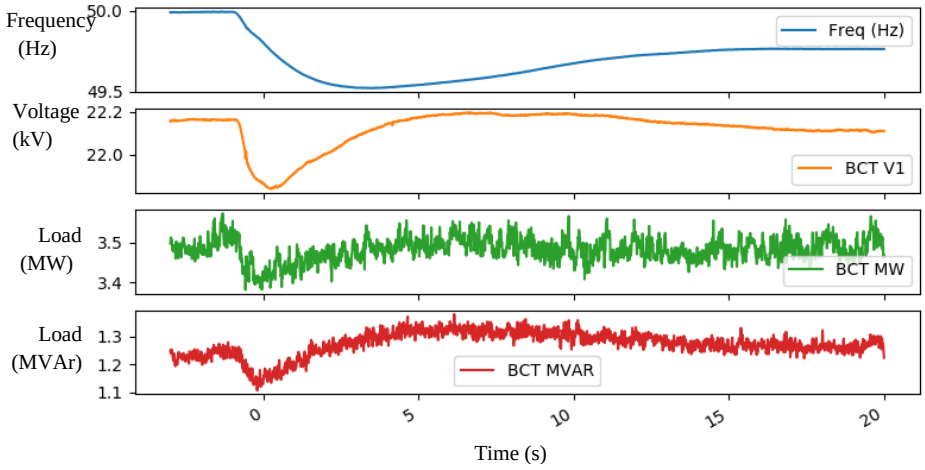

(b) Balcatta (BCT) – Metro commercial / residential (k_p = 0.97)

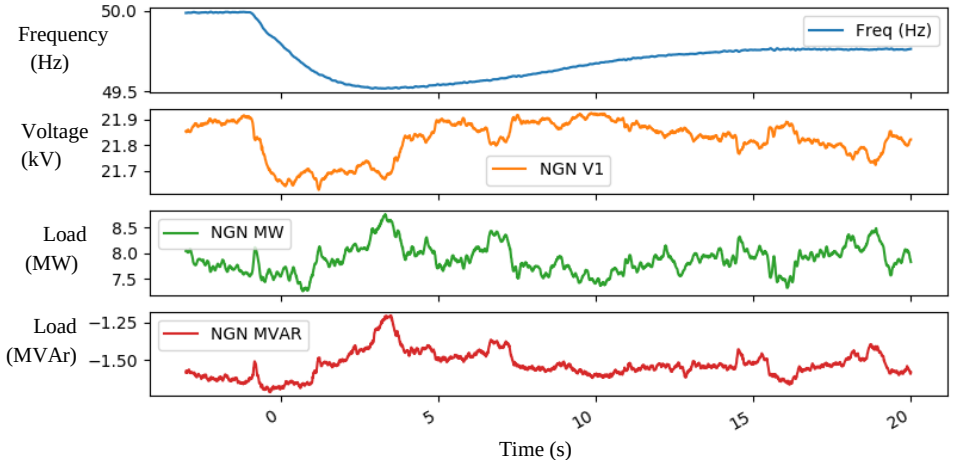

(c) Narrogin (NGN) – Rural (k_p = -5.46)

Figure 8.1. Load response at selected substations from Event-1

The individual substation traces shown in Figure 8.1 further highlight the variations in LRF estimates. The load response in Figure 8.1(a) for the Binningup desalination plant exemplifies the classical frequency-dependent load response that would be expected from a facility with a high share of induction motors, where a strong correlation between load and frequency is clearly visible. This is also reflected in the high load relief factor of 3.5.

On the other hand, the load response shown in Figure 8.1(b), corresponding to a mixed-use residential and commercial zone substation in the Perth metro area, appears more correlated with changes in bus voltage than frequency. However, a mild correlation with frequency can still be discerned (reflected in the lower load relief factor of 0.97%).

The load response shown in Figure 8.1(c) from the rural wheatbelt town of Narrogin was chosen here to highlight the wide variation in load responses at substation level (and does not necessarily reflect any inherent attributes of rural loads). From the plot, the Narrogin load appears to be more or less uncorrelated with both voltage and frequency. The large negative load relief factor of -5.46% is likely an artefact of random load movements at the substation during the event, which may have masked the true load relief effects (repeating the estimates across many events would hopefully remove the influence of this randomness).

Ultimately, the wide range of load relief factors across the substations in the SWIS raises an important question: how can individual substation-level load relief factor estimates be credibly aggregated to a system-level estimate? An average of the individual load relief factors weighted by the normalised substation load is one possibility, but a more direct method for estimating system level load relief seems to be a simpler and more attractive pathway. A further complication is that not all

substations have fault recorders and that not all fault recorders trigger on a generator contingency. So then what is the minimum sample of substation data required to form a usable aggregate estimate?

8.3 System Level LRF Estimation Results

The estimated system loads, along with the measured system frequency and PFR traces, are shown in Figure 8.2 to Figure 8.4 for each event. The estimated system LRFs, which are calculated based on linear regressions of the measured frequency and estimated load traces (sampled at 10 ms resolution over the time interval from 0s to 20s) are also presented in Table 8.3.

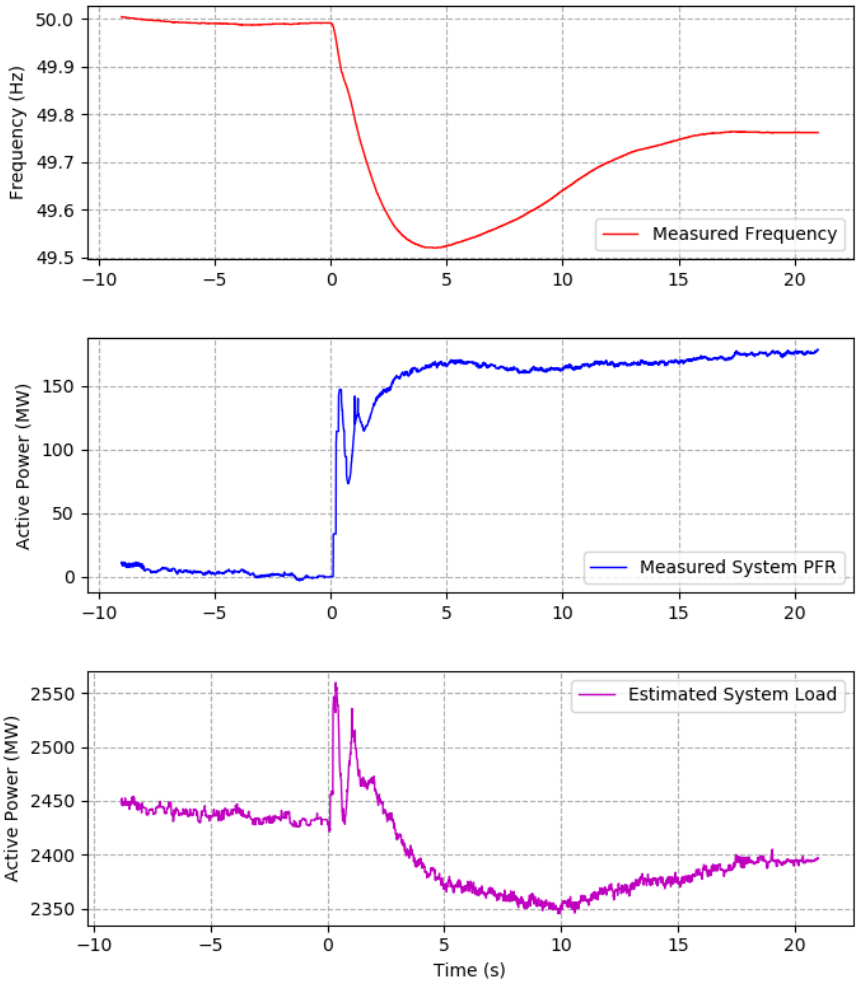

Figure 8.2. (a) The measured frequency, (b) The measured system primary frequency response, (c) The estimated system load response for Event-1

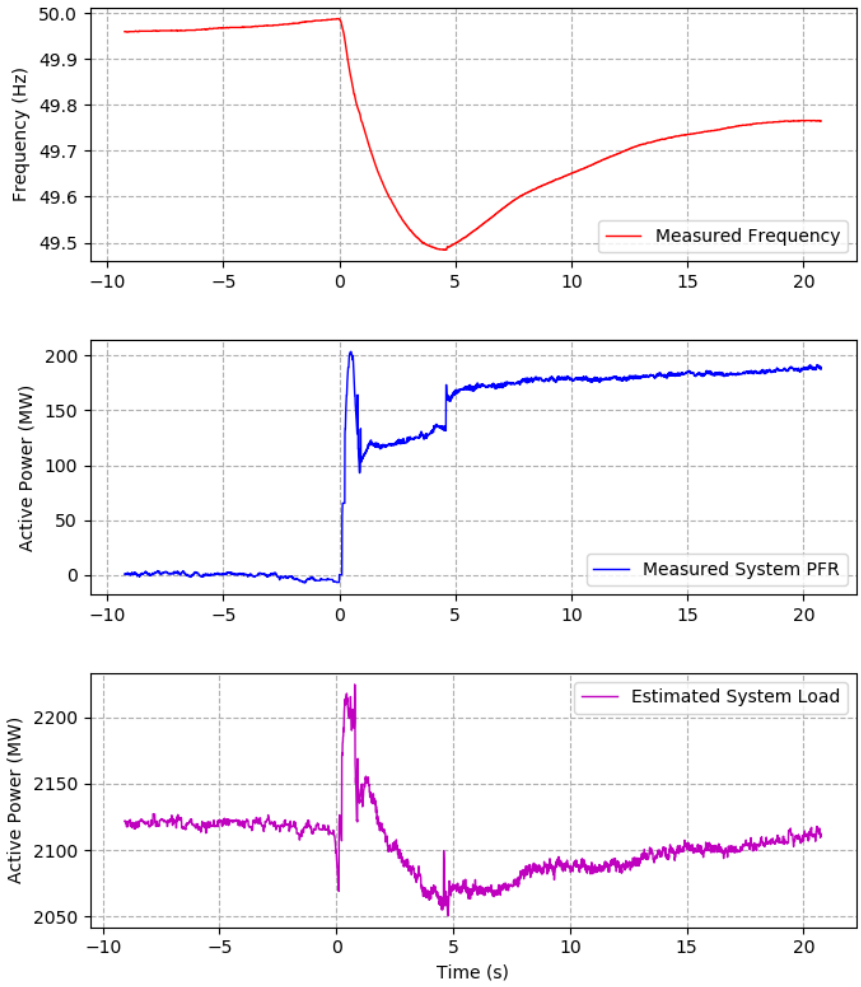

Figure 8.3. (a) The measured frequency, (b) The measured system primary frequency response, (c) The estimated system load response for Event-2

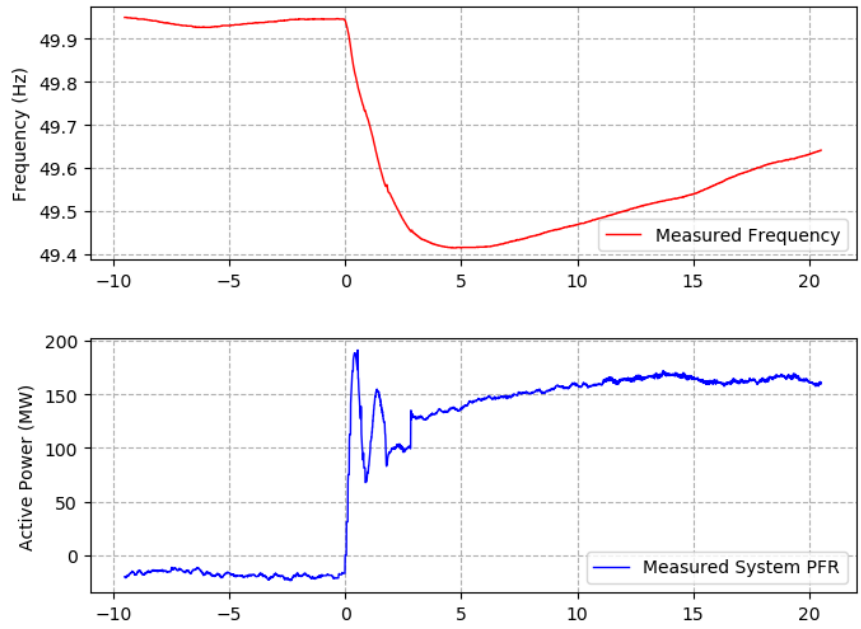

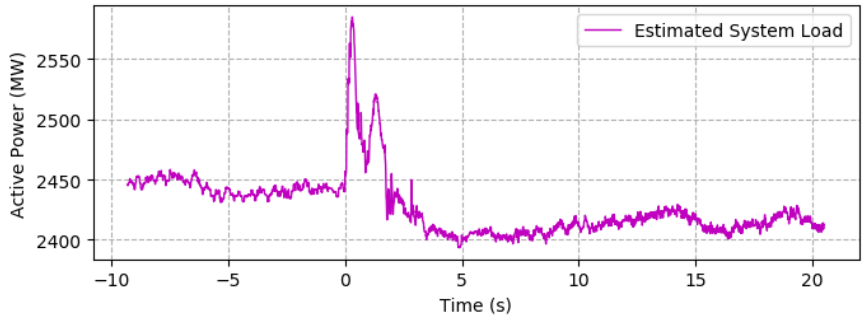

Figure 8.4. (a) The measured frequency, (b) The measured system primary frequency response, (c) The estimated system load response for Event-3

Table 8.3. Estimated system LRFs

Event	Estimated System LRF (k_p)
1	2.7302
2	2.0828
3	1.8938

The system level LRF estimates shown in Table 8.3 are broadly aligned with previous estimates reported by the SWIS network operator, which were reported to be in a range of 1.0 to 2.6 (with a mean of 1.8) [136]. It should be noted that these previous estimates were based on 4-second resolution system load (as-generated) measurements from the EMS and were subject to the synchronisation and time-averaging issues, as discussed earlier.

A noticeable element in each of the estimated system load responses is a transient spike at the onset of the contingency (t = 0). This spike occurs because the measured system PFR from the fault recorder data also includes the inertial responses of the generators. Since the proposed method is based on a reformulation of the swing equation, the inertial components are endogenous to the model and should theoretically be removed from the measured PFR trace.

One option for removing the influence of the inertial components is to discard the estimated load response in the first few seconds after the contingency when the inertial contribution is the highest (one would expect the inertial contribution to decay rapidly thereafter). Figure 8.5 shows the scatter plots of the change in frequency (x-axis) vs the change in load (y-axis) for Event-2. The LRF is estimated by taking the linear least squares fit of the points in the scatter plot. It can be seen in Figure 8.5a that when all samples are used, the inertial components are visible in the upper-right region of the plot. As samples are discarded, e.g., the first 2, 4 and 6 second in Figure 8.5b-d, respectively, the influence of the inertial components is removed and the estimated LRF increases.

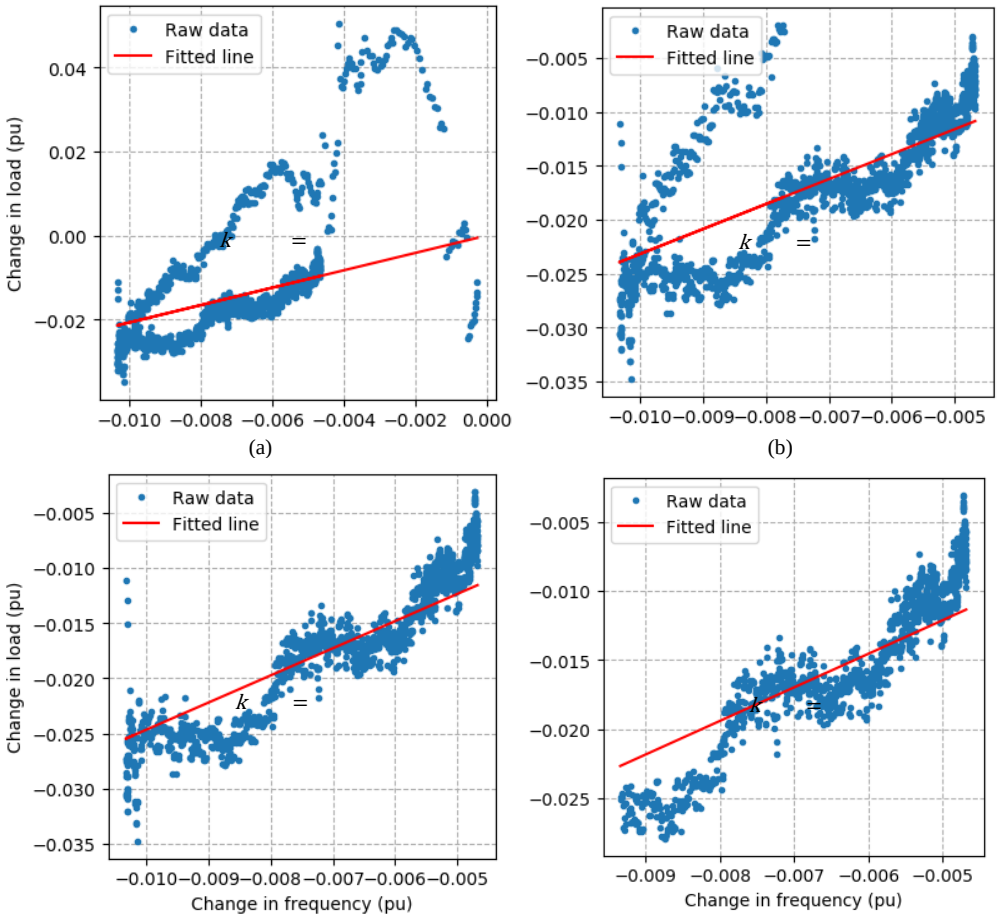

Figure 8.5. Load response scatter plot for Event-2 with varying sampling intervals of (a) 0-20, (b) 2-20, (c) 4-20, (d) 6-20 seconds, and their corresponding LRFs in MW/Hz

Figure 8.6 shows the sensitivity of the estimated LRF to the sampling interval start time, e.g., a start time of 5 sec denotes a sampling interval of 5 – 20s. It can be seen that the estimated LRFs for Event-2 and 3 are in a fairly stable range between 1.8 and 2.5. However, the estimated LRF for Event-1 increases significantly as more samples are discarded, suggesting that other material PFR contributions that were not captured in the aggregated PFR measurements. This can arise when there is incomplete fault recorder data due to improper triggering or recorder malfunction.

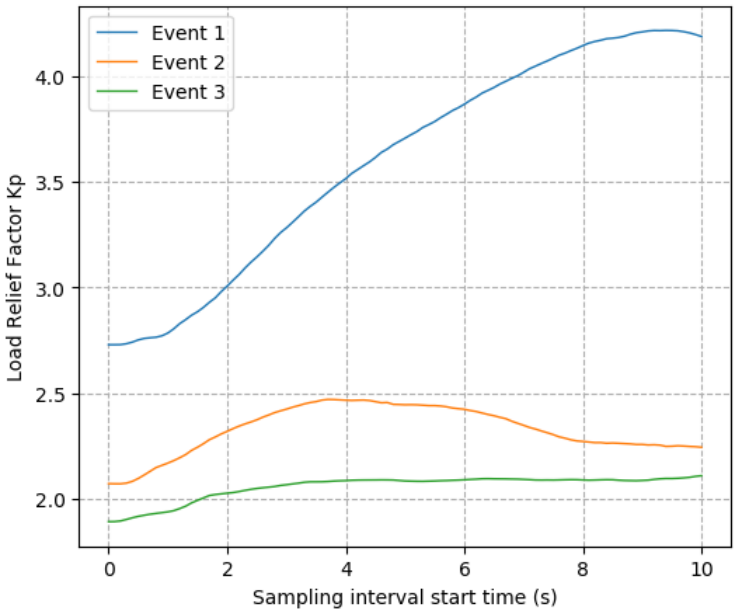

Figure 8.6. LRF estimates with varying interval start time

It is worth noting that the presence of additional droop responses in the SWIS from embedded (behind the meter) generation, including some large industrial co-gen units are not visible by the installed fault recorders. These responses are not considered in the aggregate PFR and instead form part of the system load response, which would increase the estimated LRF.

8.4 **Summary**

This chapter has evaluated the performance of a new method for estimating system-level LRFs which does not require any subjective inference on the amount of load change during frequency excursion events. This issue has hampered the consistency and repeatability of previous LRF estimates. The proposed method was tested on real generator contingency events in a medium-sized islanded network in Western Australia and the results yielded the same range of values as previous estimates.

Chapter 9 Conclusions and Future Work

The main objective of the research work presented in this thesis was to develop tools and techniques to better understand and manage stability issues in microgrids and weak grids with high shares of VRE generation. In attempting to fulfil this overarching objective, the thesis focused on several broadly connected facets of the problem.

9.1 Conclusions

The general conclusions and findings of this thesis are as follows:

(1) Topological network features have a material impact on the small-signal stability of inertia-less converter dominated microgrids with active power-frequency droop control. It was found that simple radial (unmeshed) topologies are the most stable topologies and that greater meshing leads to lower stability. The electrical distance between two converters was also found to be a significant factor, with converters that are electrically closer together (i.e., separated by a low impedance) tending to be less stable.

Therefore, from a microgrid planning perspective, the research findings support the notion that network topologies should be kept as simple as possible or operate in a ring configuration with a tie-open point.

Converters should also be installed with enough electrical decoupling

from each other to prevent unstable interactions between any two adjacent converters.

(2) Neighbouring autonomous microgrids of different nominal frequencies and voltages can be interconnected via back-to-back dc links to provide dynamic frequency support. This improves frequency stability by helping to alleviate active power imbalances in one of the autonomous microgrids, e.g., due to generation deficits or over-loading. The research results showed that such back-to-back dc links can successfully prevent frequency collapse by dynamically facilitating active power transfers from one microgrid to the other.

(3) Another frequency stability measure for microgrids with high shares of PV is to install a BESS to smooth out active power fluctuations due to PV intermittency. A novel optimal smoothing battery sizing method was proposed that explicitly takes into account the natural variability of the solar irradiation at the site location. This allows for a more optimally sized smoothing battery that is customised to the specific site location.

It was found that an approximate formulation based on a linear regression (and using the SIVI as the dependent variable) can estimate the optimal smoothing battery size using a moving-average technique with reasonable accuracy. However, it was found that the SIVI was not the well correlated with the optimal smoothing battery size when the ramp rate control technique was used.

(4) Connecting VRE generation to weak grids requires considerations not typically covered in conventional Grid Codes in order to maintain system stability and security. A technical framework was introduced to

specifically assess the integration of PV into weak grids. The framework tests for two types of weakness commonly found in weak grids (high impedance connection points (low system strength) and low-inertia connection points), and recommends studies and considerations specific to the type of weakness.

Based on a sample of case studies from actual PV project developments in South and Southeast Asia, it was found that the framework was able to uncover issues specific to weak grids that would not have been identified from analysis using conventional Grid Codes.

(5) Weak grids with low inertia are sensitive to frequency stability issues caused by large generator contingencies. As weak grids are typically smaller in scale and are more likely to have coherent generation, an aggregate single mass model can often be used for frequency stability studies. The load relief or load damping in the system is an important input into this model, but is usually estimated using coarse resolution load data. A new load relief factor (LRF) estimation method was developed using high resolution data gleaned from high-speed fault recorders. An attractive feature of the proposed LRF estimation method is that it can be run automatically without any subjective inference by the user.

The research found that the LRF estimation method yielded results that were in line with expectations and previous estimates when tested on real contingency events in a medium-sized islanded system.

9.2 Future Work

Potential future research topics in the area of this thesis are presented below:

9.2.1 Topological analysis of interconnected microgrids

The load flow initialisation method proposed in this thesis was used to analyse the impacts of microgrid topology (e.g., radial, ring and triangular mesh) to small-signal stability. This analysis could be extended from a single microgrid to interconnected microgrids, in particular the stability impacts of one or more interconnections to different microgrid clusters.

9.2.2 Multi-terminal dc links to interconnect multiple microgrids

In this thesis, it was assumed that two neighbouring microgrids were connected together via a back-to-back dc link. As a direction for future research, the operation of more than two microgrids, interconnected through multi-terminal dc links could also be investigated.

9.2.3 More accurate approximate method for sizing smoothing batteries using the ramp rate limit technique

The results of the optimal smoothing battery sizing studies in Chapter 6 indicate that the calculated SBOC using the ramp-rate limit technique is weakly correlated with the SIVI, and as a result, the approximate empirical method using the ramp rate technique-based linear regressions has limited accuracy. A future research direction can be focused on identifying a more appropriate metric than SIVI to quantify the solar irradiance variabilities when using the ramp rate technique.

9.2.4 **Enhanced load relief factor estimation and monitoring**

The results of the LRF estimation studies in Chapter 8 suggest that the proposed method could be improved if the inertial component from the measured PFR traces is removed. This could potentially be done by estimating the inertial response of each unit and then subtracting the estimated response from the PFR trace.

Another direction for future research is to monitor and track the trajectory of the estimated LRFs in order to assess the impacts of de-industrialisation and changing load composition, such as the greater use of inverter-interfaced induction motors (e.g., air conditioners) within the system.

References

Every reasonable effort has been made to acknowledge the owners of copyright materials. I would be pleased to hear from any copyright owner who has been omitted or incorrectly acknowledged.

[1] Lazard, "Lazard's levelized cost of energy analysis," Version 12.0, pp. 1-20, https://www.lazard.com/media/450784/lazards-levelized-cost-of-energy-version-120-vfinal.pdf, 2018.

[2] C.S. Lai, and M.D. McCulloch, "Levelized cost of electricity for solar photovoltaic and electrical energy storage", *Applied Energy*, 190:191-203, 2017.

[3] Global Market Outlook for 2017-2021, SolarPower Europe, http://www.solarpowereurope.org/reports/global-market-outlook-2017/, 2017.

[4] P. Huang, S.O. Negro, M.P. Hekkert, and K. Bi, "How China became a leader in solar PV: An innovation system analysis", *Renewable and Sustainable Energy Reviews*, 64: 777-789, 2016.

[5] M.K. Hairat, and S. Ghosh, "100 GW solar power in India by 2022 – A critical review", *Renewable and Sustainable Energy Reviews*, 73:1041-1050, 2017

[6] L. Ali, and F. Shahnia, "Determination of an economically-suitable and sustainable standalone power system for an off-grid town in Western Australia", *Renewable Energy*, 106:243-254, 2017.

[7] Deutsche Gesellschaft für Internationale Zusammenarbeit (GIZ), "Analysis of system stability in developing and emerging countries: Impact of variable renewable energies on power system reliability and system security",

Technical Report, https://www.giz.de/fachexpertise/downloads/giz2013-en-power-system-stability-developing-emerging-countries.pdf, 2013.

[8] C. Nayar, “Innovative remote micro-grid systems”, *International Journal of Environment & Sustainability*, vol. 1, no. 3, pp. 53-65, 2012.

[9] N. Hatziargyriou, H. Asano, R. Iravani and C. Marnay, “Microgrids”, *IEEE Power Energy Magazine*, vol. 5, no. 4, pp. 78–94, Jul./Aug. 2007.

[10] G. Pepermans, J. Driesen, D. Haeseldonckx, et al. “Distributed generation: definition, benefits and issues", *Energy Policy*, vol. 33, Issue 6, pp. 787-798, April, 2005.

[11] R.H. Lasseter, “Microgrids and distributed generation”, *Journal of Energy Engineering*, vol. 133, no. 3, pp. 144-149, Sept. 2007.

[12] A. Zaman, “100% Variable Renewable Energy Grid: Survey of Possibilities”, MSc Thesis, University of Michigan, 2018.

[13] M. C. Chandorkar, D. M. Divan, and R. Adapa, “Control of parallel connected inverters in standalone ac supply systems”, *IEEE Transactions on Industry Applications*, 29(1):136-143, 1993.

[14] E. A. A. Coehlo, P. C. Cortizo, and P. F. Garcia, “Small-signal stability for parallel-connected inverters in stand-alone ac supply systems”. *IEEE Transactions on Industrial Applications*, 38(2), 2002.

[15] R. H. Lasseter, “Microgrids”, *IEEE Power Engineering Society Winter Meeting*, 2:305-308, Jan 2002.

[16] R. Chandrasena, F. Shahnia, and S. Rajakaruna, “Control, Operation and Power Sharing among Parallel Converter Interfaced DERs in a Microgrid in the Presence of Unbalanced and Harmonic Loads”, *Australasian Universities Power Engineering Conference (AUPEC)*, 2013.

[17] K. De Brabandere, K. Vanthournout, J. Driesen, G. Deconinck, and R. Belmans, “Control of Microgrids”, *2007 IEEE Power Engineering Society General Meeting*, pages 1-7, June 2007.

[18] R. Majumder, “Some aspects of stability in microgrids”, *IEEE Transactions on Power Systems*, 28(3):3245{3252, 2013.

[19] J. Schiffer, A. Anta, T. D. Trung, J. Raisch, and T. Sezi, “On power sharing and stability in autonomous inverter-based microgrids”, *IEEE Conference on Decision and Control*, 2012.

[20] R.D. Middlebrook, “Input filter consideration in design and application of switching regulators”, *IEEE Industrial Application Society Annual Meeting*, 366-382, 1976.

[21] J. Sun, “Small-signal methods for ac distributed power systems–A review”, *IEEE Trans. Power Electronics*, 24(11):2545-2554, 2009.

[22] N. Pogaku, M. Prodanovic, and T.C. Green, “Modeling, analysis and testing of autonomous operation of an inverter-based microgrid”, *IEEE Trans. Power Electronics*, 22(2):613-625, 2007.

[23] M.N. Marwali, J.W. Jung, and A. Keyhani, “Stability analysis of load sharing control for distributed generation systems”, *IEEE Trans. Energy Conversion*, 22(3):737-745, 2007.

[24] E. Barklund, N. Pogaku, M. Prodanovic, et al., “Energy management in autonomous microgrid using stability-constrained droop control of inverters”, *IEEE Trans. Power Electronics*, 23(5):2346-2352, 2008.

[25] S. D’Arco, J.A. Suul, and O.B. Fosso, “Small-signal modeling and parametric sensitivity of a virtual synchronous machine in islanded operation”, *Int. J. of Electrical Power & Energy Systems*, 72:3-15, 2015.

[26] M. Rasheduzzaman, et al., “An accurate small-signal model of inverter-dominated islanded microgrids using dq reference frame”, *IEEE Journal of Emerging & Selected Topics in Power Electronics*, 2(4):1070-1080, 2014.

[27] F. Shahnia, “Stability and eigenanalysis of a sustainable remote area microgrid with a transforming structure”, *Sus. Energy, Grids & Networks*, 8:37-50, 2016.

[28] F. Shahnia, and A. Arefi, “Eigenanalysis-based small signal stability of the system of coupled sustainable microgrids”, *Int. J. of Electrical Power & Energy Systems*, 91:42-60, 2017.

[29] S. Mishra, and D. Ramasubramanian, “Improving the small signal stability of a PV-DE-dynamic load-based microgrid using an auxiliary signal in the PV control Loop”, *IEEE Trans. Power Systems*, 30(1):166-176, 2015.

[30] A. Jamehbozorg, and G. Radman, "Small signal analysis of power systems with wind and energy storage units", *IEEE Trans. Power Sys.*, 30(1):298-305, 2015.

[31] A.V. Jayawardena, et al., "Representation of a grid-tied microgrid as a reduced order entity for distribution system dynamics and stability studies", *Int. J. of Electrical Power & Energy Systems*, 73:591-600, 2015.

[32] V. Mariani, F. Vasca, J.C. Vasquez, and J.M. Guerrero, "Model order reductions for stability analysis of islanded microgrids with droop control", *IEEE Trans. Industrial Electronics*, 62(7):4344-4354, 2015.

[33] C. Ahumada, R. Cardenas, D. Saez, and J.M. Guerrero, "Secondary control strategies for frequency restoration in islanded microgrids with consideration of communication delays", *IEEE Trans. Smart Grid*, 7(3): 1430-1441, 2016.

[34] N. Bottrell, M. Prodanovic, and T.C. Green, "Dynamic stability of a microgrid with an active load", *IEEE Trans. Power Electronics*, 28(11):5107-5119, 2013.

[35] A.A.A. Radwan, and Y.A.R.I. Mohamed, "Stabilization of medium-frequency modes in isolated microgrids supplying direct online induction motor loads", *IEEE Trans. Smart Grid*, 5(1):358-370, 2014.

[36] F.M. Uriarte, C. Smith, S. Van Broekhoven, and R.E. Hebner, "Microgrid ramp rates and the inertial stability margin", *IEEE Trans. Power Systems*, 30(6):3209-3216, 2015.

[37] S. Tabatabaee, H. R. Karshenas, A. Bakhshai, and P. Jain, "Investigation of droop characteristics and x/r ratio on small-signal stability of autonomous microgrid", *Power Electronics, Drive Systems and Technologies Conference (PEDSTC)*, pages 223-228, 2011.

[38] R. Majumder, B. Chaudhuri, A. Ghosh, R. Majumder, G. Ledwich, and F. Zare, "Improvement of stability and load sharing in an autonomous microgrid using supplementary droop control loop", *Power and Energy Society General Meeting*, 2010 IEEE, July 2010.

[39] A. A. A. Radwan and Y. A. R. I. Mohamed, "Modeling, analysis, and stabilization of converter-fed ac microgrids with high penetration of converter-interfaced loads", *IEEE Transactions on Smart Grid*, 3(3):1213-1225, Sept 2012.

[40] I.P. Nikolakakos, et al., “Stability evaluation of interconnected multi-inverter microgrids through critical clusters”, *IEEE Trans. Power Systems*, 31(4):3060-3072, 2016.

[41] D.E. Olivares, A. Mehrizi-Sani, A.H. Etemadi, C.A. Canizares, R. Iravani, M. Kazerani, A.H. Hajimiragha, O. Gomis-Bellmunt, M. Saeedifard, R. Palma-Behnke, G.A. Jimenez-Estevez, and N.D. Hatziargyriou, “Trends in microgrid control”, *IEEE Transactions on Smart Grid*, 5(4):1905-1919, July 2014

[42] X. Chen, W. Pei, and X. Tang, “Transient stability analyses of micro-grids with multiple distributed generations”, *Power System Technology (POWERCON)*, 2010 International Conference on, pages 1-8, Oct 2010

[43] M. Zhixin, A. Domijan, and F. Lingling, “Investigation of microgrids with both inverter interfaced and direct ac-connected distributed energy resources”, *IEEE Transactions on Power Delivery*, 26(3):1634-1642, July 2011.

[44] F. Andrade, J. Cusido, and L. Romeral, “Transient stability analysis of inverter-interface distributed generators in a microgrid system”, *EPE 2011 - 14th European Conference on Power Electronics and Applications*, pages 1-10, 2011.

[45] Z. Wang, M. Xia, and M. Lemmon, “Voltage stability of weak power distribution networks with inverter connected sources”, *American Control Conference (ACC)*, pages 6577-6582, 2013

[46] R. H. Lasseter, “Smart distribution: Coupled microgrids”, *Proceedings of the IEEE*, 99(6):1074-1082, June 2011.

[47] E. Pashajavid, F. Shahnia, and A. Ghosh, “Interconnection of two neighbouring autonomous microgrids based on small signal analysis”, *ICPE-ECCE Asia - 9th International Conference on Power Electronics and ECCE Asia*, pages 213-220, 2015

[48] M. J. Hossain, M. A. Mahmud, F. Milano, S. Bacha, and A. Hably, “Design of robust distributed control for interconnected microgrids”, *IEEE Transactions on Smart Grid*, PP(99):1-12, 2015

[49] Y. Li, N. Liu, C. Wu, and J. Zhang, “Distributed optimization for generation scheduling of interconnected microgrids”, *Power and Energy Engineering Conference (APPEEC)*, 2015 IEEE PES Asia-Pacific, pages 1-5, Nov 2015

[50] A. Teixeira, K. Paridari, H. Sandberg, and K. H. Johansson, “Voltage control for interconnected microgrids under adversarial actions”, *Emerging Technologies Factory Automation (ETFA)*, 2015 IEEE 20th Conference on, pages 1-8, Sept 2015

[51] F. Shahnia, R. Chandrasena, S. Rajakaruna, and A. Ghosh, “Primary control level of parallel distributed energy resources converters in system of multiple interconnected autonomous microgrids within self-healing networks”, *IET Generation, Transmission and Distribution*, 8(2):203-222, 2014.

[52] R. Majumder and G. Bag, “Parallel operation of converter interfaced multiple microgrids”, *Electrical Power and Energy Systems*, 55:486-496, 2014.

[53] D. Somayajula and M.L. Crow, “An integrated active power filter-ultracapacitor design to provide intermittency smoothing and reactive power support to the distribution grid”, *IEEE Trans. Sustainable Energy*, vol. 5, no. 4, pp. 1116-1125, 2014.

[54] G. Wang, M. Ciobotaru and V.G. Agelidis, “Power smoothing of large solar PV plant using hybrid energy storage”, *IEEE Trans. Sustainable Energy*, vol. 5, no. 3, pp. 834-842, 2014.

[55] S. Teleke, M.E. Baran, S. Bhattacharya and A.Q. Huang, “Rule-based control of battery energy storage for dispatching intermittent renewable sources”, *IEEE Trans. Sustainable Energy*, vol. 1, no. 3, pp. 117-124, 2010.R.

[56] M. Datta, T. Senjyu, A. Yona, and T. Funabashi, “Photovoltaic output power fluctuations smoothing by selecting optimal capacity of battery for a photovoltaic-diesel hybrid system”, *Electric Power Components & Systems*, vol. 39, no. 7, pp. 621-644, 2011.

[57] D. Wang, S. Ge, H. Jia, et al., “A demand response and battery storage coordination algorithm for providing microgrid tie-line smoothing services”, *IEEE Trans. Sustainable Energy*, vol. 5, no. 2, pp. 476-486, 2014.

[58] Khodabakhsh and S. Sirouspour, “Optimal control of energy storage in a microgrid by minimizing conditional value-at-risk”, *IEEE Trans. Sustainable Energy*, vol. 7, no. 3, pp. 1264-1273, 2016.

[59] T. Senjyu, M. Datta, A. Tona, et al., “PV output power fluctuations smoothing and optimum capacity of energy storage system for PV power generator”, *Int. Conf. on Renewable Energy and Power Quality (ICREPQ)*, pp. 35-39, 2018.

[60] J. Marcos, O. Storkel, L. Marroyo, et al., “Storage requirements for PV power ramp-rate control”, *Solar Energy*, vol. 99, pp. 28-35, 2014.

[61] J. Marcos, I. de la Parra, M. Garcia, and L. Marroyo, “Control strategies to smooth short-term power fluctuations in large photovoltaic plants using battery storage systems”, *Energies*, vol. 7, no. 10, pp. 6593-6619, 2014.

[62] K. Sandhu, and A. Mahesh, “A new approach of sizing battery energy storage system for smoothing the power fluctuations of a PV/wind hybrid system”, *International Journal of Energy Research*, vol. 40, pp. 1221-1234, 2016.

[63] A. Mahesh, K. Sandhu, and K.V. Rao, “Optimal sizing of battery energy storage system for smoothing power fluctuations of a PV/wind hybrid system”, *International Journal of Emerging Power Systems*, vol. 18, no. 1, 2017.

[64] R.P. Sasmal, S. Sen, A. Chakraborty, “Solar photovoltaic output smoothing: using battery energy storage system”, *National Power System Conference*, pp. 1-5, 2016.

[65] A. Desta, P. Courbin, V. Sciandra, “Gaussian-based smoothing of wind and solar power productions using batteries”, *International Journal Mechanical Engineering & Robotics Research*, vol. 6, no. 2, 2017.

[66] H. Nazaripouya, C.C. Chu, H.R. Pota, and R. Dagh, “Battery energy storage system control for intermittency smoothing using optimized two-stage filter”, *IEEE Trans. Sustainable Energy*, vol. 9, no. 2, pp. 664-675, 2018.

[67] X. Li, D. Hui, and X. Lai, “Battery energy storage station-based smoothing control of photovoltaic and wind power generation fluctuations”, *IEEE Trans. Sustainable Energy*, vol. 4, no. 2, pp. 464-473, 2013.

[68] M. Pang, Y. Shi, W. Wang, and X. Yuan, “A method for optimal sizing hybrid energy storage system for smoothing fluctuations of wind power”, *IEEE PES Asia-Pacific Power and Energy Conference (APPEEC)*, Xi’an, 2016.

[69] M. Song, C. Gao, M. Shahidehpour, et al., “Multi-time-scale modeling and parameter estimation of TCLs for smoothing out wind power generation variability”, *IEEE Trans. Sustainable Energy*, vol. 10, no. 1, pp. 105-118, 2019.

[70] F. Zhang, G. Wang, K. Meng, et al., “Improved cycle control and sizing scheme for wind energy storage system based on multiobjective optimization”, *IEEE Trans. Sustainable Energy*, vol. 8, no. 3, pp. 966-977, 2017.

[71] Y. Zhou, Z. Yan and N. Li, “A novel state of charge feedback strategy in wind power smoothing based on short-term forecast and scenario analysis”, *IEEE Trans. Sustainable Energy*, vol. 8, no. 2, pp. 870-879, 2017.

[72] F. Zhang, K. Meng, Z. Xu, et al., “Battery ESS planning for wind smoothing via variable-interval reference modulation and self-adaptive SOC control strategy”, *IEEE Trans. Sustainable Energy*, vol. 8, no. 2, pp. 695-707, 2017.

[73] A.V. Savkin, M. Khalid and V.G. Agelidis, “A constrained monotonic charging/discharging strategy for optimal capacity of battery energy storage supporting wind farms”, *IEEE Trans. Sustainable Energy*, vol. 7, no. 3, pp. 1224-1231, 2016.

[74] T.K.A. Brekken, A. Yokochi, A. von Jouanne, et al., “Optimal energy storage sizing and control for wind power applications”, *IEEE Trans. Sustainable Energy*, vol. 2, no. 1, pp. 69-77, 2011.

[75] G.M. Lohmann, “Irradiance variability quantification and small-scale averaging in space and time: A short review”, *Atmosphere*, vol. 9, no. 264, 2018.

[76] R. Hudson, and G. Heilscher, “PV grid integration–System management issues and utility concerns”, *Energy Procedia*, 25:82-92, 2012.

[77] A. Etxegarai, P. Eguia, E. Torres, et al, “Review of grid connection requirements for generation assets in weak power grids”, *Renewable and Sustainable Energy Reviews*, 41:1501-1514, 2015.

[78] N. Mendis, K.M. Muttaqi, S. Perera, and M.N. Uddin, “Remote area power supply system: an integrated control approach based on active power balance”, *IEEE Industry Applications Magazine*, 21(2):63-76, 2015.

[79] Y. Tan, L. Meegahapola, and K.M. Muttaqi, “A review of technical challenges in planning and operation of remote area power supply systems”, *Renewable and Sustainable Energy Reviews*, 38:876-889, 2014.

[80] Y. Zhang, S.H. Huang, J. Schmall, et al, “Evaluating system strength for large-scale wind plant integration”, *IEEE Power & Energy Society General Meeting*, 1-5, National Harbor, 2014.

[81] A. Cabrera-Tobar, E. Bullich-Massague, M. Aragues-Penalba, and O. Gomis-Bellmunt, “Review of advanced grid requirements for the integration of large

scale photovoltaic power plants in the transmission system", *Renewable and Sustainable Energy Reviews*, 62: 971-987, 2016.

[82] A. Q. Al-Shetwi, and M. Z. Sujod, "Grid-connected photovoltaic power plants: A review of the recent integration requirements in modern grid codes", *Int. Journal of Energy Research*, 42(5):1849-1865, 2018

[83] R. Shah, N. Mithulanathan, R.C. Bansal, and V.K. Ramachandaramurthy, "A review of key power system stability challenges for large-scale PV integration", *Renewable and Sustainable Energy Reviews*, 41:1423-1436, 2015.

[84] J. Wu, A. Botterud, A. Mills, et al, "Integrating solar PV (photovoltaics) in utility system operations: Analytical framework and Arizona case study", *Energy*, 85:1-9, 2015.

[85] NERC, "Integrating inverter-based resources into weak power systems: Reliability guideline", North American Reliability Corporation, Technical report, https://www.nerc.com/pa/RAPA/rg/ReliabilityGuidelines/Reliabilty_Guideline_-_Integrating_VER_into_Weak_Power_Systems.pdf, 2017.

[86] T. Sarkar, A. K. Dan, S. Ghosh, K. D. Bhattacharya and H. Saha, "Interfacing solar PV power plant with rural distribution grid: challenges and possible solutions", *International Journal of Sustainable Energy*, 2017.

[87] L. Wang, R. Yan, and T. Saha, "Voltage Management for Large Scale PV Integration into Weak Distribution Systems", *IEEE Trans. Smart Grid*, 2017.

[88] Y. Xu, and S. Yan, "The calculation of PV station penetration limit in weak grid based on approximate linear programming algorithm", *IEEE Region 10 Conference (TENCON)*, 1-4, Xi'an, 2013.

[89] P. Tierlens, and D.V. Hertem, "The relevance of inertia in power systems", *Renewable and Sustainable Energy Reviews*, 55: 999-1009, 2016.

[90] S.R. Kumar, F. Gafaro, A. Daka, and A. Raturi, "Modelling and analysis of grid integration for high shares of solar PV in small isolated systems–A case of Kiribati", *Renewable Energy*, 108:589-597, 2017.

[91] J. Gomez, F. Fernandez, F. Gafaro, and F. Perelini, "Application of grid studies for the secure and optimal utilisation of variable renewables in islands-Study

case in Samoa", *5th Int. Workshop on Integration of Solar Power into Power Systems*, Brussels, 2015.

[92] B. K. Kurniawan, H. Suyono, and H. S. Dachlan, "Injection analysis of 5 MWp photovoltaic power plant on 20kV distribution network in Kupang", *International Journal of Research in Engineering and Science (IJRES)*, 5(8):45-50, 2017.

[93] AEMO, "Contingency Frequency Response in the SWIS", Australian Energy Market Operator, Technical Report, 2019.

[94] P.M. Anderson and M. Mirheydar, "A low-order system frequency response model", *IEEE Trans. Power Syst*, vol. 5, no. 3, pp. 720-729, 1990.

[95] C. Concordia and S. Ihara, "Load representation in power system stability studies", *IEEE Trans. Power Apparatus and Systems*, vol. PAS-101, no. 4, pp. 969-977, 1982.

[96] R.P. Schulz, "Modeling of governing response in the Eastern Interconnection", *IEEE Power and Energy Society Winter Meeting*, vol.1, pp. 561-566, New York, 1999.

[97] M. Davies, F. Moran and J.I. Bird, "Power/frequency characteristics of the British grid system", *Proceedings of the IEE - Part A: Power Engineering*, vol. 106, no. 26, pp. 154-162, 1959.

[98] G.J. Berg, "System and load behaviour following loss of generation. Experimental results and evaluation", *Proceedings of the IEE, vol. 119*, no. 10, pp. 1483-1486, 1972.

[99] J.W. O'Sullivan and M.J. O'Malley, "Identification and validation of dynamic global load model parameters for use in power system frequency simulations", *IEEE Trans. Power Syst*, vol. 11, no. 2, pp. 851-857, 1996.

[100] R. Pearmine, Y.H. Song, T.G. Williams and A. Chebbo, "Identification of a load-frequency characteristic for allocation of spinning reserves on the British electricity grid", *IEE Proceedings - Generation, Transmission and Distribution*, vol. 153, no. 6, pp. 633-638, 2006.

[101] J.M. Guerrero, J.C. Vasquez, J. Matas, et al., "Hierarchical control of droop-controlled ac and dc microgrids: A general approach toward standardization", *IEEE Trans. Industrial Electronics*, 58(1), 2011.

[102] Siemens PTI, “Block Oriented Simulation Language (BOSL) Standard Controllers”, 2008.

[103] “IEEE recommended practice for excitation system models for power system stability studies”, IEEE Std. 421.5, 2005.

[104] R. Teodorescu and F. Blaabjerg, “Flexible control of small wind turbines with grid failure detection operating standalone and grid-connected mode”, *IEEE Trans. on Power Electronics*, vol. 19, no. 5, pp. 1323-1332, Sept. 2004.

[105] “Australian Government Bureau of Meteorology – One minute solar data”, accessed 1/10/2018, http://reg.bom.gov.au/climate/reg/oneminsolar

[106] J.S. Stein, C.W. Hansen, and M.J. Reno, “The variability index: A new and novel metric for quantifying irradiance and PV output variability”, *World Renewable Energy Forum*, Denver, pp. 13-17, 2012.

[107] Australian Renewable Energy Agency, “Hybrid power generation for Australian off-grid mines”, Technical Report, 2018.

[108] A. Ellis, D. Schoenwald, D. Hawkings, and S. Willard, “PV output smoothing with energy storage”, *38th IEEE Photovoltaic Specialists Conference*, pp. 1523-1528, 2012.

[109] W. Greenwood, O. Lavrova, A. Mammoli, et al., “Optimization of solar PV smoothing algorithms for reduced stress on a utility-scale battery energy storage system”, *Electrical Energy Storage Applications and Technologies Conference*, Sandia National Laboratories, 2013.

[110] W.H. Press, S.A. Tuekolsky, W.T. Vetterling, and B.P. Flannery, “Numerical recipes in C: The art of scientific computing”, Cambridge University Press, 2nd ed., pp. 397-401, 2002.

[111] “Stand-alone power systems - Part 2: System design guidelines”, AS/NZS 4509.2, 2010.

[112] J.F. Manwell, A. Rogers, G. Hayman, et al., “Hybrid2: A hybrid system simulation model, Theory manual,” National Renewable Energy Laboratory”, Technical report, 2006.

[113] J.F. Manwell, J.G. McGowan, U. Abdulwahid, and K. Wu, “Improvements to the Hybrid2 battery model”, *American Wind Energy Association Windpower 2005 Conference*, Denver, 2005.

[114] J.F. Manwell, and J. McGowan, “Extension of the kinetic battery model for wind/hybrid power systems”, *5th European Wind Energy Association Conference*, pp. 284-289, 1994.

[115] B. Sivaneasan, N. K. Kandasamy, M. L. Lim, and K. P. Goh, “A new demand response algorithm for solar PV intermittency management”, *Applied Energy*, 218:36-45, 2018.

[116] “IEEE Guide for planning dc links terminating at ac locations having low short-circuit capacities”, IEEE Std-1204, 1997.

[117] A. Gavrilovic, “AC/DC System strength as indicated by short circuit ratios”, *Int. Conference on AC and DC Power Transmission*, 27-32, London, 1991.

[118] A. Mohamed, “Analysis of grid codes and parameters identification for load frequency control”, MSc Thesis, Politecnico di Milano, 2016.

[119] L. Luo, W. Gu, X.P. Zhang, et al, “Optimal siting and sizing of distributed generation in distribution systems with PV solar farm utilized as STATCOM”, *Applied Energy*, 210:1092-1100, 2018.

[120] R.K. Varma, V. Khadkikar, and R. Seethapathy, “Nighttime application of PV solar farm as STATCOM to regulate grid voltage”, *IEEE Trans. Energy Conversion*, 24(4): 983-985, 2009.

[121] X.I. Koutiva, T.D. Vrionos, N.A. Vovos, and G.B. Giannakopoulos, “Optimal integration of an offshore wind farm to a weak ac grid”, *IEEE Trans. Power Delivery*, 21(2):987-994, 2006.

[122] C. Hackney, and B. Bates, “Delivering the dream–Nyngan solar farm connection”, *National Electric Energy Conference (EECON)*, Sydney, 2014.

[123] Y. Zhou, D.D. Nguyen, P.C. Kjaer, and S. Saylors, “Connecting wind power plant with weak grid – Challenges and solutions”, *IEEE Power & Energy Society General Meeting*, 1-5, Vancouver, 2013.

[124] P. Kundur, “Power system stability and control”, McGraw-Hill, 1994.

[125] P. Kundur, J. Paserba, V. Ajjarapu, et al, “Definition and classification of power system stability”, *IEEE Trans. Power Systems*, 19(3): 1387-1401, 2004.

[126] R.V. Haaren, M. Morjaria, and V. Fthenakis, “Empirical assessment of short-term variability from utility-scale solar PV plants”, *Progress in Photovoltaics: Research and Applications*, 22:548-559, 2014.

[127] N. Hamsic, A. Schmetter, A. Mohd, et al, "Increasing renewable energy penetration in isolated grids using a flywheel energy storage system", *Int. Conf. on Power Engineering, Energy and Electrical Drives*, 1-6, Setubal, 2007.

[128] Y. Rebours, and D. Kirschen, "A survey of definitions and specifications of reserve services", Technical Report, The University of Manchester, 2005.

[129] EirGrid and Soni, "EirGrid Operational Constraints Update", Technical Report, 2017.

[130] B. Tamimi, C. Canizares and K. Battacharya, "System stability impact of large-scale and distributed solar photovoltaic generation: The case of Ontario", *IEEE Trans. Sustainable Energy*, 4(3):680-688, 2013.

[131] IEEE Task Force on Load Representation for Dynamic Performance, "Load representation for dynamic performance analysis (of power systems)", *IEEE Trans. Power Systems*, vol. 8, no. 2, pp. 472-482, 1993.

[132] N. Masood, R. Yan and T.K. Saha, "Investigation of load frequency relief from field measurements and its impact on contingency reserve evaluation", *IEEE Trans. Power Systems*, vol. 33, no. 1, pp. 567-577, 2018.

[133] P.M. Ashton, C.S. Saunders, G.A. Taylor, et al., "Inertia estimation of the GB power system using synchrophasor measurements", *IEEE Trans. Power Systems*, vol. 30, no. 2, pp. 701-709, 2015.

[134] D.P. Chassin, Z. Huang, M.K. Donnelly, et al., "Estimation of WECC system inertia using observed frequency transients", *IEEE Trans. Power Systems*, vol. 20, no. 2, pp. 1190-1192, 2005.

[135] ENTSO-E, "Frequency measurement requirements and usage", Technical Report, 2018.

[136] Western Power, "WPN renewable penetration and system security", Technical Report, DMS# 11545078, 2014.

[137] "Olympic Batteries DC2-500 Technical Data Sheet", http://www.olympicbatteries.com.au/portals/0/product-pdfs/spec%20sheet%20for%20dc2-500%20auscell.pdf

[138] "SMA Sunny Boy Storage 3.7 / 5.0 / 6.0 Technical Data Sheet", https://files.sma.de/dl/31186/sbs37-60-den1751-v21web.pdf

[139] “Sunpower 225 Solar Panel Technical Data Sheet”, https://www.energymatters.com.au/images/sunpower/spr-225_com.pdf

[140] “SMA Tripower 5000TL – 12000TL Technical Data Sheet”, https://files.sma.de/dl/17781/stp12000tl-den1723-v10web.pdf

[141] J. Marcos, L. Marroyo, E. Lorenzo, et al., “Power output fluctuations in large scale PV plants: One year observations with one second resolution and a derived analytic model”, *Prog. Photovolt. Res. Appl.*, vol. 19, pp. 218-227, 2011.

[142] N. Jayawarna, X. Wu, Y. Zhang, N. Jenkins and M. Barnes, “Stability of a microgrid”, *3rd IET International Conference on Power Electronics, Machines and Drives (PEMD)*, 2006.

[143] Q. Zhong and G. Weiss, “Synchronverters: Inverters that mimic synchronous generators”, *IEEE Trans. Ind. Elec.*, vol. 58(4), pp. 1259-1267, 2011

[144] N. Soni, S. Doolla, and M.C. Chandorkar, “Inertia Design Methods for Islanded Microgrids Having Static and Rotating Energy Sources”, *IEEE Trans. Ind. App.*, vol. 52(6), pp. 5165-5174, 2016.

[145] Y. Xianghua and G. Feng, “Quantitative analysis of transient angle stability for grid-connected inverter considering droop coefficient”, *IEEE Conference on Energy Internet and Energy System Integration (EI2)*, Beijing, China, 2017

[146] U. Tamrakar, D. Galipeau, R. Tonkoski and I. Tamrakar, “Improving transient stability of photovoltaic-hydro microgrids using virtual synchronous machines”, *IEEE Eindhoven PowerTech*, Eindhoven, Netherlands, 2015

[147] J. Lopes, C. Moreira and A. Madureira, “Defining control strategies for microgrids islanded operation”, *IEEE Trans. Power Sys.*, vol. 21(2), 2006

[148] J.C. Vasquez, J.M. Guerrero, J. Miret and L. Garcia de Vicuna, “Hierarchical Control of Intelligent Microgrids”, *IEEE Industrial Electronics Magazine*, vol. 4(4), pp. 23-29, 2011

[149] A. Tsikalakis and N. Hatziargyriou, “Centralized control for optimizing microgrid operation”, *IEEE Power and Energy Society General Meeting*, Detroit, USA, 2011

[150] J. Schiffer, T. Seel, J. Raisch and T. Sezi, “Voltage Stability and Reactive Power Sharing in Inverter-Based Microgrids With Consensus-Based Distributed Voltage Control”, *IEEE Trans. Control Sys. Tech.*, vol. 24(1), 2016

[151] F. Guo, C. Wen, J. Mao and Y. Song, “Distributed Secondary Voltage and Frequency Restoration Control of Droop-Controlled Inverter-Based Microgrids”, *IEEE Trans. Ind. Elec.*, vol. 62(7), 2015

[152] J.W. Simpson-Porco, Q. Shaflee, F. Dorfler, J.C. Vasquez and J.M. Guerrero, “Secondary Frequency and Voltage Control of Islanded Microgrids via Distributed Averaging”, *IEEE Trans. Ind. Elec.*, vol. 62(11), 2015

[153] Australian Energy Market Operator (AEMO), National Electricity Market power system model, electronic dataset

Publications arising from this Thesis

Journal papers

1) **Julius Susanto**, F. Shahnia, D. Ludwig, "A framework to technically evaluate integration of utility-scale photovoltaic plants to weak power distribution systems", *Applied Energy*, 2018; 231:207–221
2) **Julius Susanto**, F. Shahnia, "Optimal capacity of a battery energy storage system to smooth out power fluctuations in PV-Diesel microgrids", under first revision in *IEEE Transactions on Sustainable Energy*, TSTE-00451-2019

Conference papers

3) **Julius Susanto**, F. Shahnia, A. Ghosh, S. Rajakaruna, "Interconnected microgrids via back-to-back converters for dynamic frequency support", 24th Australasian Universities Power Engineering Conference (AUPEC), Perth, Australia, 2014
4) **Julius Susanto**, F. Shahnia, A. Arefi, "Small signal model load flow initialisation for converter-dominated microgrids", POWERCON, Wollongong, Australia, 2016
5) **Julius Susanto**, F. Shahnia, A. Arefi, "Effects of network characteristics and topology on the stability of converter-dominated microgrids", 27th Australasian Universities Power Engineering Conference (AUPEC), Melbourne, Australia, 2017

6) F. Shahnia, **Julius Susanto**, M. A. Mahmud, “Evaluating the stability impact of the interconnecting tie-line between coupled neighbouring microgrids”, IEEE Power Electronics, Drives and Energy Systems (PEDES), Chennai, India, 2018

7) **Julius Susanto**, F. Shahnia, “Smoothing batteries for PV-Diesel hybrid microgrids”, International Symposium on Industrial Electronics (ISIE), Vancouver, Canada, 2019

8) **Julius Susanto**, F. Shahnia, D. Sharafi, L. Kwek, “Estimation of system load relief factor using high-resolution fault recorder data”, International Conference on Power and Energy Systems (ICPES), Perth, Australia, 2019